Preparation of Cold Mg^+ Ion Clouds for Sympathetic Cooling of Highly Charged Ions at SPECTRAP

Dissertation
zur Erlangung des Grades
"Doktor der Naturwissenschaften"
im Promotionsfach Chemie

am Fachbereich Chemie, Pharmazie und
Geowissenschaften
der Johannes Gutenberg-Universität Mainz

Radu Mircea Cazan
geboren in Iasi, Rumänien

Mainz, Februar 2012

Abstract

The bound electrons in hydrogen-like or lithium-like heavy ions experience extremely strong electric and magnetic fields in the surrounding of the nucleus. Laser spectroscopy of the ground-state hyperfine splitting in the lead region provides a sensitive tool to test strong-field quantum electro dynamics (QED), especially in the magnetic sector. Previous measurements on hydrogen-like systems performed in an electron-beam ion trap (EBIT) or at the experimental storage ring (ESR) were experimentally limited in accuracy due to statistics, the large Doppler broadening and the ion energy. The full potential of the QED test can only be exploited if measurements for hydrogen- and lithium-like ions are performed with accuracy improved by 2-3 orders of magnitude. Therefore, the new Penning trap setup SPECTRAP - dedicated for laser spectroscopy on trapped and cooled highly charged ions - is currently commissioned at GSI Darmstadt. Heavy highly charged ions will be delivered to this trap by the HITRAP facility in the future.

SPECTRAP is a cylindrical Penning trap with axial access for external ion injection and radial optical access mounted inside a cold-bore superconducting Helmholtz-type split-coil magnet. To reach the targeted accuracy in laser spectroscopy, an efficient and fast cooling process for the highly charged ions must be employed. This can be realized by sympathetic cooling with a cloud of laser-cooled light ions. Within this thesis work, a laser system and an ion source for the production of such a $^{24}Mg^{+}$ ion cloud was developed and commissioned at SPECTRAP. An all-solid-state laser system for the generation of 279.6 nm light was designed and built. It consists of a fiber laser at 1118.5 nm followed by frequency quadrupling using two successive second-harmonic generation stages with actively stabilized ring resonators and nonlinear crystals. The laser system can deliver more than 15 mW of UV laser power under optimal conditions and requires little maintenance. Additionally, a Mg^{+} ion source based on the electron-impact ionization of a Mg atomic beam was developed for pulsed injection into the trap. It was demonstrated that it delivers ion bunches with small time, momentum and energy spread, and it was used in combination with the laser system to create the first clouds of up to 2600 laser-cooled Mg^{+} ions in SPECTRAP. Fluorescence detection of the ions as well as electronic detection using the FFT-ICR technique was demonstrated. The analysis of the fluorescence lineshape indicated single-ion sensitivity and that a final temperature of about 100 mK was reached within a few seconds of cooling.

Zusammenfassung

Die Elektronen in wasserstoff- und lithium-ähnlichen schweren Ionen sind den extrem starken elektrischen und magnetischen Feldern in der Umgebung des Kerns ausgesetzt. Die Laserspektroskopie der Hyperfeinaufspaltung im Grundzustand des Ions erlaubt daher einen sensitiven Test der Quantenelektrodynamik in starken Feldern insbesondere im magnetischen Sektor. Frühere Messungen an wasserstoffähnlichen Systemen die an einer Elektronenstrahl-Ionenfalle (EBIT) und am Experimentierspeicherring (ESR) der GSI Darmstadt durchgeführt wurden, waren in ihrer Genauigkeit durch zu geringe Statistik, einer starken Dopplerverbreiterung und der großen Unsicherheit in der Ionenenergie limitiert. Das ganze Potential des QED-Tests kann nur dann ausgeschöpft werden, wenn es gelingt sowohl wasserstoff- als auch lithium-ähnliche schwere Ionen mit einer um 2-3 Größenordnung gesteigerten Genauigkeit zu spektroskopieren. Um dies zu erreichen, wird gegenwärtig das neue Penningfallensystem SPECTRAP an der GSI aufgebaut und in Betrieb genommen. Es ist speziell für die Laserspektroskopie an gespeicherten hochgeladenen Ionen optimiert und wird in Zukunft von HITRAP mit nierderenergetischen hochgeladenen Ionen versorgt werden.

SPECTRAP ist eine zylindrische Penningfalle mit axialem Zugang für die Injektion von Ionen und die Einkopplung eines Laserstrahls sowie einem radialen optischen Zugang für die Detektion der Fluoreszenz. Um letzteres zu realisieren ist der supraleitende Magnet als Helmholtz-Spulenpaar ausgelegt. Um die gewünschte Genauigkeit bei der Laserspektroskopie zu erreichen, muss ein effizienter und schneller Kühlprozess für die injizierten hochegeladenen Ionen realisiert werden. Dies kann mittels sympathetischer Kühlung in einer lasergekühlten Wolke leichter Ionen realisiert werden. Im Rahmen dieser Arbeit wurde ein Lasersystem und eine Ionenquelle für die Produktion einer solchen $^{24}Mg^{+}$ Ionenwolke aufgebaut und erfolgreich an SPECTRAP in Betrieb genommen. Dazu wurde ein Festkörperlasersystem für die Erzeugung von Licht bei 279.6 nm entworfen und aufgebaut. Es besteht aus einem Faserlaser bei 1118 nm der in zwei aufeinanderfolgenden Frequenzverdopplungsstufen frequenzvervierfacht wird. Die Verdopplerstufen sind als aktiv stabilisierte Resonantoren mit nichtlinearen Kristallen ausgelegt. Das Lasersystem liefert unter optimalen Bedingeungen bis zu 15 mW bei der ultravioletten Wellenlänge ud erwies sich während der Teststrahlzeiten an SPECTRAP als ausgesprochen zuverlässig. Desweiteren wurde eine Ionequelle für die gepulste Injektion von Mg^{+} Ionen in die SPECTRAP

Falle entwickelt. Diese basiert auf der Elektronenstoßionisation eines thermischen Mg-Atomstrahls und liefert in der gepulsten Extraktion Ionenbündel mit einer kleinen Impuls- und Energieverteilung. Unter Nutzung des Lasersystems konnten damit an SPECTRAP erstmals Ionenwolken mit bis zu 2600 lasergekühlten Mg Ionen erzeugt werden. Der Nachweis erfolgte sowohl mittels Fluoreszenz als auch mit der FFT-ICR Technik. Aus der Analyse des Fluoreszenz-Linienprofils lässt sich sowohl die Sensitivität auf einzelne gespeicherte Ionen als auch eine erreichte Endtemperatur in der Größenordnung von ≈ 100 mK nach wenigen Sekunden Kühlzeit belegen.

To my wife, my friends, my family and to all the people
who struggle for a better life

Contents

List of Figures

LIST OF FIGURES

List of Tables

1

Introduction

1.1 Motivation

One of the most successful scientific theories up to date, the quantum electrodynamic theory (QED), was subject to extensive experimental tests and confirmations over the last decades. Often, the accuracy of the predicted QED effects is limited by the uncertainty of the fine structure constant α. A way to improve the theory is to extract the value of α from measurements which are more accurate than prediction by QED. To date, the most precise determination of α was done through measurements of electron g value and it is better than 1 ppb [1]. Another example is the g-factor of the bound electron in hydrogen-like systems from which an improved electron mass was extracted. Lately, another stringent test of bound state QED was presented with a measurement of the g-factor of H-like $^{28}Si^{13+}$ [2].

Extremely important is the validity of the theory in the ultra-relativistic regime, namely in the presence of extreme static electric and magnetic fields [3]. Even though the modern technology has not found a way to produce such enormous static fields, nature provides us with a complete system for study: highly charged ions (HCI). These are heavy ions, almost completely stripped of electrons and they represent an isolated system, where the remaining electron experiences average electric fields up to 10^{16} V·cm^{-1} and magnetic fields up to 10^4 T. These ions, naturally occuring only in high temperature plasmas in the universe, can be produced nowadays in electron beam ion traps and at accelerator facilities. They are available at the experimental storage rings as hydrogen-like ions, few-electron systems or even bare nuclei up to U^{92+}. The HITRAP facility

under commissioning at GSI Darmstadt [4] will be capable of delivering these HCI as a low-energy beam to further experiments.

The experiments planned to use the HITRAP facility include the measurement of the g-factor of a bound electron in hydrogen-like ions [5] and high-accuracy mass spectrometry [6]. The g-factor experiment focuses on precise determination of the g-factor of bound electrons using forbidden transitions in HCI. This provides a stringent tests of bound-state QED. Additionally, nuclear magnetic moments can be extracted from these measurements. High-accuracy mass spectrometry will allow for a precise determination of atomic binding energies in few-electron systems.

The results presented in this thesis are made in the framework of one of the experiments associated with HITRAP, namely SPECTRAP (SPECtroscopy TRAP) [7]. SPECTRAP aims to check the vacuum polarization and self energy in the strong field regime, as predicted by the QED, by performing laser spectroscopy on cold Pb^{81+} or Bi^{82+} in a Penning trap. Under normal circumstances, i.e. in neutral or singly charged ions, the hyperfine splitting (HFS) of the ground state, as a result of interaction between the nuclear magnetic moment and the magnetic moment of the bound electron, is a very small effect. It is about three orders of magnitude smaller than the fine splitting structure, caused by the spin-orbit interaction. For a H-like ion, the HFS is given by [8]

$$\Delta E^{1s} = \frac{4}{3}\alpha(\alpha Z)^3 g_I \frac{m_e}{m_p}\frac{2I+1}{2} m_e c^2 A_s (1-\delta)(1-\epsilon) \tag{1.1}$$

where α is the fine structure constant, g_I the nuclear g-factor, I the nuclear spin, m_e and m_p are the electron and the proton mass, respectively. The last three terms, A_s, $(1-\delta)$ and $(1-\epsilon)$ are the correction factors for the relativistic energy of the s orbital electron, the charge distribution and the magnetic moment distribution [9, 10], respectively.

For HCI, this hyperfine splitting of the fundamental level increases roughly proportional to Z^3 and it amounts to 243.87 nm in H-like $^{209}Bi^{82+}$ [11]. The lifetime of the upper HFS state decreases with Z^{-9} and reduces the lifetime of the F=5 state to approximatively 350 μs. Altogether, this means that this transition is accessible to laser spectroscopy, along with HFS transitions in other HCI, as pictured in Fig. 1.1, taken from [12].

The hyperfine transition in Li-like $^{209}Bi^{80+}$ at 1555 nm can also be used to disentangle nuclear structure from QED effects [13]. Both transitions were recently measured in an experiment at the Experimental Storage Ring also at GSI by the LIBELLE collaboration

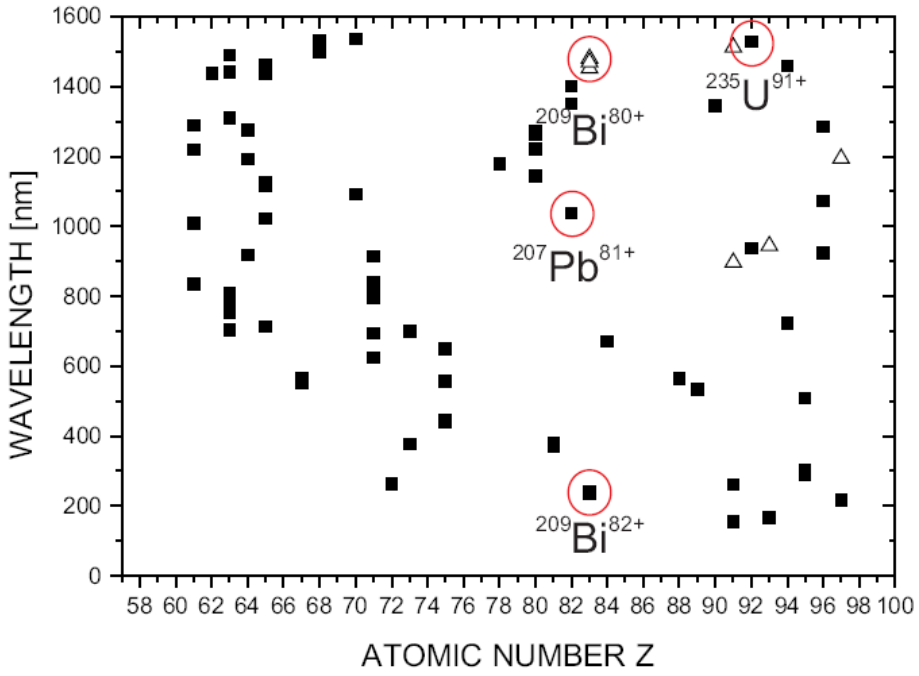

Figure 1.1: Hyperfine splitting in H-like (square) and Li-like (triangle) highly charged ions with the most interesting spectroscopy candidates emphasized. The figure is taken from [12].

[14]. The measurements in the ion trap provide the unique possibility to perform spectroscopy on a well localized cloud of highly charged ions with continuous laser excitation and relative efficient fluorescence detection. By further cooling the ions, it is expected to obtain an unprecedented accuracy [15] due to the reduction of the Doppler broadening.

1.2 Trapping and Cooling Benefits

Although, for laser spectroscopy, HCI can be studied in storage rings, accuracy is limited by the uncertainty of the ion velocity, which shifts the transition frequency, and by the large Doppler width [16]

$$\delta\nu_D = \nu_0\sqrt{\frac{8\ \ln 2\ k_B T}{mc^2}} \tag{1.2}$$

where ν_0 is the transition frequency, k_B is the Boltzmann constant, m is the ion mass, c is the speed of light and T is the temperature of the ion ensemble. For example, in the Experimental Storage Ring at GSI, the Doppler width can amount to $\approx 20-40$ GHz and, together with the uncertainty of absolute energy/velocity of the ion, limits the accuracy of the measurement on the order of 10^{-4}.

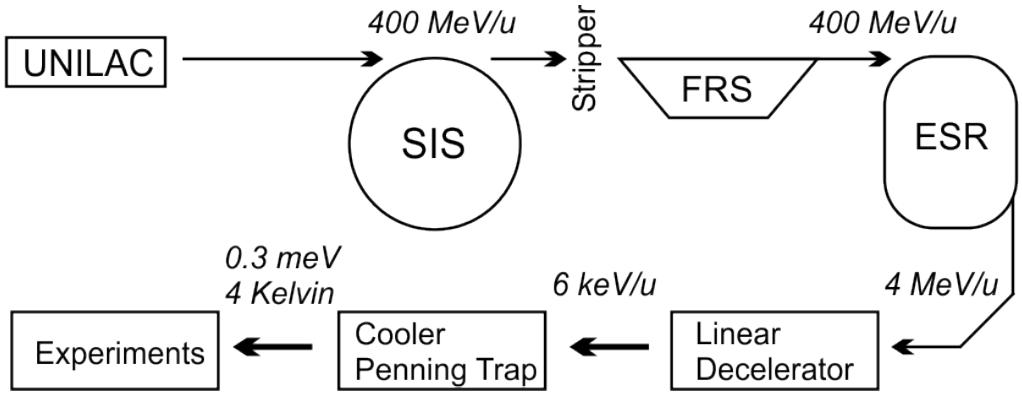

Figure 1.2: HITRAP facility at GSI Darmstadt.

Hence, by trapping them, one can therefore expect an increase in accuracy of at least an order of magnitude. The Doppler width can be greatly reduced by using a proper cooling technique. A sub-Kelvin temperature for $^{209}Bi^{82+}$ is equivalent to a Doppler width $\delta\nu_D \lesssim 61$ MHz, which is almost three orders of magnitude less than in the storage ring. Due to the special nature of HCI, only a few cooling methods are appropriate, emphasized in the next chapter.

Additionally to the high accuracy for laser spectroscopy, a cold trapped ion cloud will also give a stronger fluorescence signal. For a constant number of ions, the narrower Doppler profile corresponding to a cold cloud is also equivalent to a higher maximum fluorescence rate.

1.3 Sources of HCI

Among different ways of producing HCI, two are commonly used [17]: in an accelerator facility [4] and using an electron beam ion source, (EBIS) [18], or an electron beam ion trap, EBIT [19].

Using an accelerator facility, a high-energy ion beam is directed through a thin foil or a gas target. The resulting stripped HCI are collected in a storage ring or decelerated even more and fed into a trap. The parameters which are optimized are the speed of the ion and the thickness of the target, depending on the ionization cross section for that speed. For HITRAP, HCI coming from the UNILAC linear accelerator are accelerated in the heavy-ion synchrotron SIS, stripped in a foil to the desired charge state and injected into the storage ring ESR. In the ESR the ions can be decelerated down to an energy of

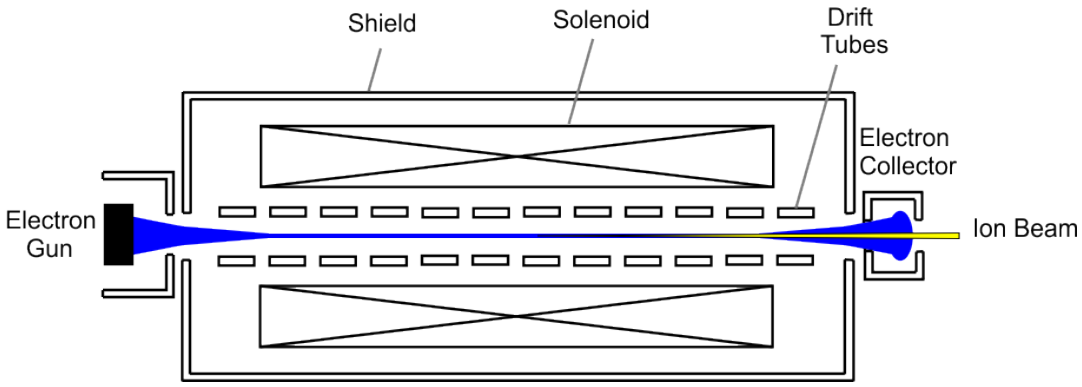

Figure 1.3: Schematic description of an electron beam ion source (EBIS).

about 4 MeV/u. They are then extracted in a fast-extraction mode as short ion bunches, decelerated in a combination of a drift tube and an RFQ decelerator. Then they are loaded into a Cooler Penning trap and cooled to liquid helium temperatures (Fig. 1.2). This corresponds to an energy reduction by 11 orders of magnitude.

The other common way of producing HCI is the EBIS. It is based on ion charge breeding inside a trap. The operating principle is depicted in Fig. 1.3. An electron gun generates an electron beam which is sent through a long stack of drift tubes inside a superconductive solenoid. The electron beam is transversely compressed by the strong magnetic field generated by the solenoid to a high density along the drift tubes. At the end of the drift tubes, the electrons are decelerated and collected by an electron collector. The ions are produced by electron-impact ionization of a neutral gas fed into the trap region. Afterwards, in order to have a higher charge state, the ions are further ionized by trapping them. They are trapped radially by the space charge of the electron beam whereas axially they are confined by positive voltages at the end electrodes.

The charge state will depend on the storage time inside the trapping region as well as on the energy of the electron beam. After achieving the desired charge state, one of the end electrodes is lowered and the HCI are extracted through the hollow electron collector. The storage time is between 0.1 and several seconds while the pulse length is between 0.1 and 100 microseconds. Typical magnetic fields used are 2-6 T and the length of the drift tubes is over one meter. The vacuum inside the trapping region should be very good, below 10^{-11} mbar, in order to avoid electron capture of HCI from the background gas. The electron beam energy should be higher than the ionization energy of the last electron corresponding to the desired charge state of a particular ion and has values above 5 keV.

Compared to the EBIS, an EBIT is typically used for both production and study of HCI. Therefore, the EBIT usually has only three short drift tubes with slits in the central one and, additionally, the magnetic field is generated by Helmholtz geometry coils. The Super-EBIT [20] in Livermore was capable to produce and trap bare U^{92+} with an 200 keV electron beam energy, thus obtaining the highest charge state ever reached with this type of source.

1.4 Outline

The current thesis is structured in five chapters:

Chapter 2 deals with the main theory principles concerning the experiments presented in this thesis:

- the trapping principles with an emphasis on the Penning traps and the non-destructive ion detection;
- the main cooling methods appropriate for cooling of HCI ions and used throughout the experiment: resistive, laser and sympathetic cooling;
- a brief introduction into the principles of second harmonic generation, including the Boyd-Kleinmann theory;
- an overview of the Mg^+ cooling and the description of the Hänsch-Couillaud locking scheme.

Chapter 3 describes the experimental setup with the steps towards building the laser system, finding an appropriate ion source and finishing with a brief overview of the SPEC-TRAP setup. The Penning trap and the electronic circuitry was designed and built in the work of another thesis [21].

Chapter 4 presents the first successful results of laser cooling of Mg^+ ions at SPEC-TRAP. An emphasis is put on the efficient trap loading as well as on the optimization of the fluorescence signal as a very sensitive detection system. The focus is also on the determination of the trap main parameters together with the testing of the cryogenic electronics associated with the trap.

Chapter 5 summarizes the results of the experiments and presents the planned improvements and future experiments.

2

Theory

2.1 Ion Traps

2.1.1 Trapping Principles

The main concept about ion trapping is to have a 3D potential well that will keep the ions localized. An ion will be trapped at some point in space if the force corresponding to the potential energy minimum is directed towards that point [17, 22]

$$\vec{F} = -k\vec{r} \tag{2.1}$$

where $\vec{r}$ is the displacement from the minimum energy point and k is a proportionality constant.

The force opposes the gradient of the potential energy

$$\vec{F} = -\nabla U = -\nabla q\Phi \tag{2.2}$$

which points to a harmonic potential and - using the Cartesian coordinates - the potential can be written as

$$\Phi = \frac{\Phi_0}{d^2}(\alpha x^2 + \beta y^2 + \gamma z^2) \tag{2.3}$$

where Φ_0 can be a time-dependent function, d is a normalization factor and α, β, γ are some coefficients. If we neglect space charge effects, the above equation must satisfy the Laplace equation

$$\Delta\Phi = 0 \tag{2.4}$$

and thus the relationship

$$\alpha + \beta + \gamma = 0 \tag{2.5}$$

between the coefficients must be fulfilled.

For practical reasons, a rotational symmetry around one axis can be considered

$$\alpha = \beta = -\frac{\gamma}{2}. \tag{2.6}$$

Using one solution to these conditions, Eq. (2.3) becomes

$$\Phi = \Phi_0(x^2 + y^2 - 2z^2) = \Phi_0(r^2 - 2z^2). \tag{2.7}$$

The difference in sign shows that the potential has a minimum along two axes but a maximum along the other axis. Hence, it is a saddle point. This is in accordance with Earnshaw's theorem [23] which states that "a charge acted on by electrostatic forces cannot rest in stable equilibrium in an electric field". This inconvenience can be surpassed by adding a magnetic field along the z axis - Penning traps [24] - or by using an electric quadrupole field alternating at high frequency which will "rotate" the saddle - RF (Paul) traps [25].

Equipotential lines of a quadrupole potential according to Eq. (2.7) are hyperbolic, thus it is geometrically optimal to design the electrodes as a ring with a hyperbolic cross section and with two hyperboloids of revolution as endcaps, as shown in Fig. 3.37.

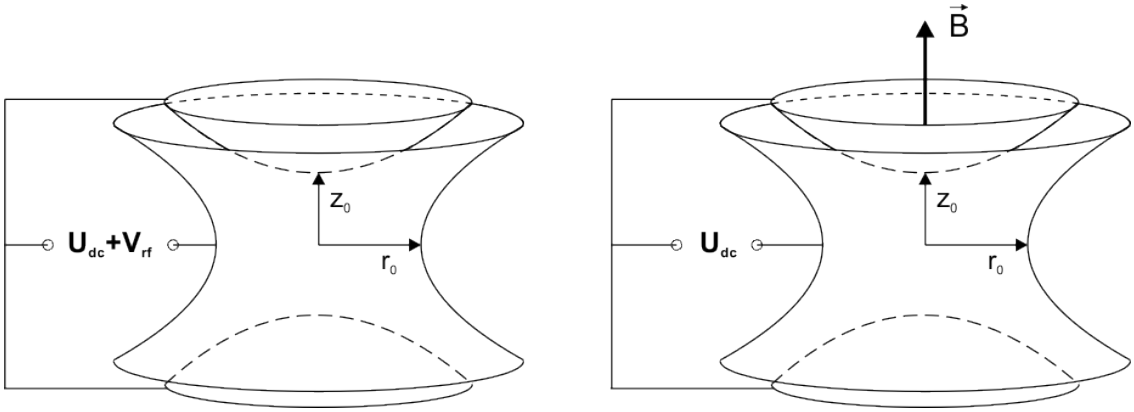

Figure 2.1: The hyperbolic trap in two variants: (a) Paul trap (b) Penning trap.

This was the way first traps were made [24, 25, 26, 27]. For a trap that is designed for laser spectroscopy, this layout has a number of disadvantages: First, the coupling of the laser beam to the trap center and the fluorescence detection are hampered by the large solid angle that is blocked by the trap elements. Often it is also important that ions are transported into the trapping region, especially if short-lived or highly charged ions are to be investigated, which cannot be produced inside the trap. For both reasons it is required

to have openings in the trap electrodes which necessarily give rise to field imperfections. Thus, many cylindrical traps are designed with additional compensation electrodes that restore the quadrupole field in a region around the center.

2.1.2 Ideal Penning Traps

In a Penning trap, the potential (2.7) and the electrical field created between the ring and the endcaps are chosen such that the motion along z is stable whereas the radial dimension is unbound. By adding a magnetic field along the z axis, the ion is radially confined as well. An ion in a Penning trap has a specific motion which can be determined by solving the equations of motion.

First, the ion is subject to the Lorentz force in the radial plane [6, 28]

$$\vec{F_L} = q\vec{v} \times \vec{B} \tag{2.8}$$

where $\vec{B}$ is the magnetic field along the z axis, q is the ion charge and v is the ion speed component perpendicular to the magnetic field direction.

Due to this force, the ion will have a circular motion around the z axis with an angular frequency

$$\omega_c = \frac{q}{m}B \tag{2.9}$$

with m being the ion mass. Besides this motion, the ion will feel the effect of the overlapped quadrupole potential

$$\Phi(z, r) = \frac{U_{dc}}{2d^2}\left(z^2 - \frac{r^2}{2}\right) \tag{2.10}$$

where U_{dc} is the potential between the endcaps and the ring while d characterizes the trap dimension

$$d^2 = \frac{1}{2}\left(z_0^2 + \frac{r_0^2}{2}\right). \tag{2.11}$$

The electric field can be written as

$$E_z = -\frac{U_{dc}}{d^2}z \tag{2.12}$$

along the z axis and

$$\vec{E_r} = \frac{U_{dc}}{2d^2}\vec{r} \tag{2.13}$$

in the radial plane. Using these values for the electrical and magnetic field, the equations of motion are

$$m\ddot{z} = qE_z \tag{2.14}$$

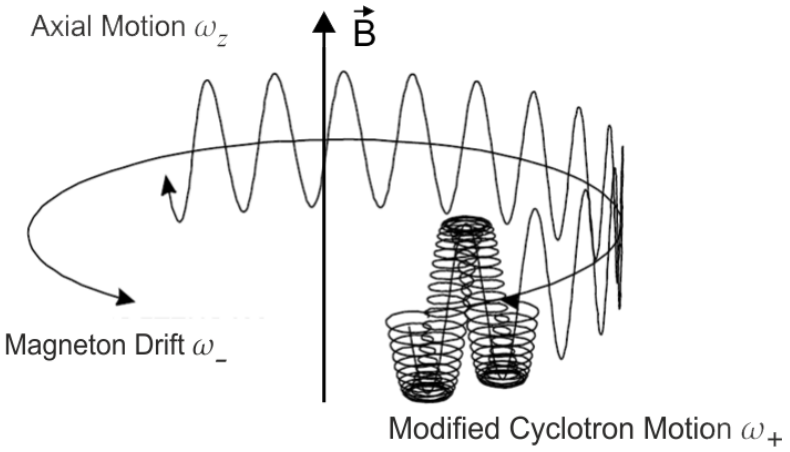

Figure 2.2: Schematic trajectory with the three independent eigenmotions of an ion in a Penning trap.

and

$$m\ddot{\vec{r}} = q(\vec{E_r} + \dot{\vec{r}} \times \vec{B}). \tag{2.15}$$

The solution of these differential equations exhibits three independent periodic motions, as shown in Fig. 2.2. The three eigenfrequencies of these motions for an ideal electric quadrupole are:

- the axial oscillation frequency associated with the harmonic trapping motion along the trap axis

$$\omega_z = \sqrt{\frac{qU_{dc}}{md^2}} \tag{2.16}$$

- the reduced cyclotron frequency associated with the circular modified cyclotron motion

$$\omega_+ = \frac{\omega_c}{2} + \sqrt{\frac{\omega_c^2}{4} - \frac{\omega_z^2}{2}} \tag{2.17}$$

- the magnetron frequency associated with the circular magnetron motion ($\vec{E} \times \vec{B}$ drift), around the trap axis

$$\omega_- = \frac{\omega_c}{2} - \sqrt{\frac{\omega_c^2}{4} - \frac{\omega_z^2}{2}}. \tag{2.18}$$

From Eqs. (2.17) and (2.18) one can easily come to an important relationship for mass spectrometry, since it relates the mass of the ion to some experimentally measurable parameters

$$\omega_c = \omega_+ + \omega_-. \tag{2.19}$$

If the roots of Eqs. (2.17) and (2.18) are real, then the motion is bound, which gives the condition for stable trapping

$$\omega_c^2 > 2\omega_z^2. \tag{2.20}$$

Using the values for ω_c and ω_z, the trapping condition can be written in terms of trap voltage

$$U_{dc} < \frac{qB^2d^2}{2m}. \tag{2.21}$$

The last equation relates the repulsive radial electrostatic potential to the minimum magnetic field required to counteract the effect and to keep the ions confined.

2.2 Non-destructive Ion Detection: FFT-ICR

There is always an experimental necessity in working with traps to detect if ions are actually trapped, what kind of ions are trapped or how the ions react to external perturbations, e.g. applied RF-fields. Besides laser resonance fluorescence detection, which is limited to a few species, there is another non-destructive method for ion detection and measurements on the trapped ions. This method is based on direct measurements of the reduced cyclotron frequency by detecting the mirror charge induced in the ring electrode. The ring electrode is therefore splitted in two, four of even eight segments.

Considering a ring configuration with four segments, an ion performing the cyclotron motion inside the trap will induce periodic image currents in the ring segments. The frequency of the image currents is given by the modified cyclotron motion. The principle of Fast Fourier Transform - Ion Cyclotron Resonance (FFT-ICR) has been applied for a long time with Penning traps for large ion clouds [29]. Unfortunately these image currents from a single ion are very small, only of the order of a few 10 fA. Recent work is going on to use it even for single-ion detection of singly charged, very rare species in cryogenic traps [30].

Using more ions doesn't solve the problem immediately, since the ions are moving incoherently and, accordingly, the induced image currents will be constant. To overcome this situation, an external RF electrical field is applied using two opossing ring segments (Fig. 2.3). If the RF frequency matches the reduced cyclotron frequency, there will be a periodic transfer of energy from the external dipolar excitation to the ions which will cause the ions to start moving coherently.

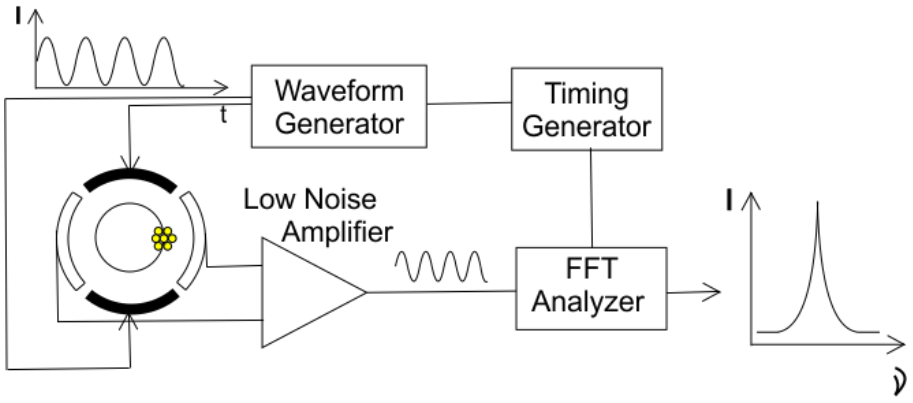

Figure 2.3: Schematic principle of an Fast-Fourier Transform - Ion Cyclotron Resonance (FFT-ICR) setup.

After a number of excitation cycles, if there are enough ions and they move coherently, a detectable periodic current will be induced on the remaining opposing plates. Still being very small, this current is usually first amplified by a low noise (sometimes cryogenic) amplifier and then fed into an FFT analyzer. From the output spectrum of the FFT analyzer, the reduced cyclotron frequency can be extracted.

Since the reduced cyclotron frequency ω_+ is much higher than the magnetron frequency ω_-, from Eq. (2.19) the real cyclotron frequency can be approximated as

$$\omega_c \approx \omega_+ \tag{2.22}$$

and thus, knowing the value of the magnetic field, the mass of the ion can be calculated and identified

$$m = \frac{qB}{\omega_c}. \tag{2.23}$$

When the trap is used as a very precise mass spectrometer, relative measurements to a known ion species with mass m_{ref} are performed

$$m_x = \frac{\omega_{c(\text{ref})}}{\omega_{c(x)}} m_{\text{ref}}. \tag{2.24}$$

Moreover, the axial frequency ω_z is calculated or measured experimentally in order to calculate the magnetron frequency ω_- and, thus, better calculate the real cyclotron frequency ω_c. An useful relationship, valid also for real Penning traps, is the Brown-Gabrielse invariance theorem [31]

$$\omega_c^2 = \omega_+^2 + \omega_-^2 + \omega_z^2. \tag{2.25}$$

Unlike real Penning traps, which are subject to correction factors, Eq. (2.19) is valid in the case of an ideal Penning trap. This means from comparing this equation with Eq. (2.25) that

$$2\omega_+\omega_- = \omega_z^2 \tag{2.26}$$

leading to the real cyclotron frequency as

$$\omega_c = \omega_+ + \frac{\omega_z^2}{2\omega_+} \tag{2.27}$$

which is independent of ω_-.

In typical trap experiments, by using an ion with a known mass, the measured cyclotron frequency can be used to calculate the magnetic field inside the trap to very high accuracy. For laser spectroscopy, this provides useful information, for example, for calculating the Zeeman shift of the atomic energy levels.

2.3 Cooling of Ions in a Trap

2.3.1 Resistive Cooling

Resistive cooling is one of the three cooling methods will be used in the final SPECTRAP experiment. Its implementation is partially similar with the FFT-ICR and it can even serve simultaneously as a non-destructive ion detection method. Resistive cooling is better suited for the Penning traps since in the Paul traps there is a flow of energy from the trapping RF field to the ions which can counteract and, at some temperature, even overwhelm the cooling effects [26].

Like in the case of FFT-ICR, an ion oscillating along the z axis with the axial frequency ω_z will induce image currents in the endcaps. Provided that they are connected to an external RLC damping circuit as shown in Fig. 2.4, there will be a transfer of energy from the oscillating ions to the external damping circuit, even though the movement of several ions is not necessarily coherent[27]. The RLC circuit ensures a strong energy exchange between those ions which have axial frequency close to

$$\omega_0 = \frac{1}{\sqrt{LC}}. \tag{2.28}$$

The temperature limit achievable in this way is the temperature of the external circuit. Usually, the circuit is kept at liquid nitrogen (77 K) or even at liquid helium (4 K)

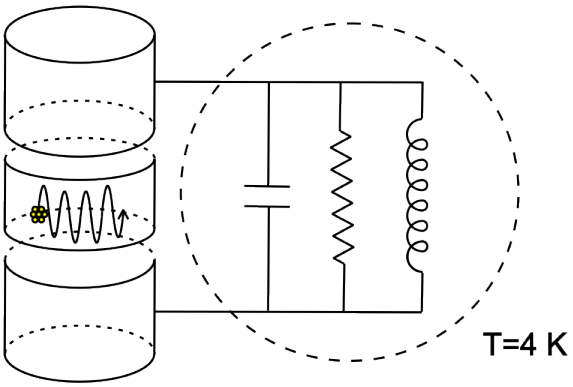

Figure 2.4: A setup for resistive cooling: the endcaps of the Penning trap are connected to an external RLC-damping circuit.

temperature. The energy loss of ions is exponential with a time constant [17]

$$\tau = \left(\frac{2z_0}{q}\right)^2 \frac{m}{\omega L Q} \tag{2.29}$$

where L is the inductance of the circuit and Q its quality factor. This time constant highly depends on the number of ions, their mass and charge state and on the quality factor of the external circuit. Moreover, resistive cooling is acting on the center-of-mass of the ion cloud and therefore, only the correlated motion of the ions is cooled in a relatively short time. The behavior of the uncorrelated motion has been observed in [32] but has not been investigated in detail so far. As a rule of the thumb, the center-of-mass motion can be cooled within several hundreds of milliseconds while cooling of the uncorrelated motion can take many seconds [17, 22, 33].

2.3.2 Laser Cooling

Laser cooling [34, 35] was proposed already a few decades ago and it was the first cooling method capable of cooling ions or atoms into the mK regime. This paved the way for scientists to obtain the lowest temperatures on Earth. Additionally, this method seems to be the fastest cooling method to this temperature range so far.

Laser cooling uses photons to cool the ions or atoms, with the aid of the Doppler effect and the photon's momentum transfer. The laser is detuned from the atomic resonance frequency in such a way that its frequency, respectively the energy of the photons, is slightly below the one required for exciting the ion to the excited level. Thus, there will be no interaction between them and the laser if the ions are at rest (Fig. 2.5a). But if

an ion is moving towards the laser, it will effectively see a higher frequency due to the Doppler effect

$$\nu = \nu_L \gamma \left(1 - \frac{v}{c} \cos \theta\right) \tag{2.30}$$

where ν is the frequency observed in the ion's rest frame, ν_L the laser frequency, γ the relativistic time dilatation factor - which can be neglected for small ion velocities $v \ll c$ - and θ is the angle between the ion's direction of motion and the propagation direction of the laser beam.

Those ions that are traveling towards the laser beam and have a velocity v that compensates the detuning of the laser, will absorb a photon and its momentum will be reduced accordingly (Fig. 2.5b).

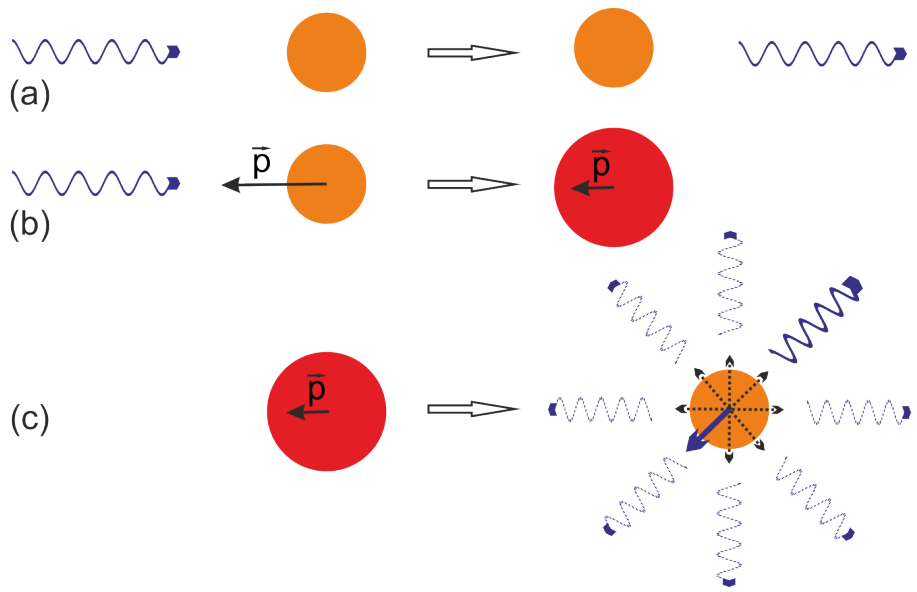

Figure 2.5: Laser interaction with the ion at rest (a). Laser interaction and with a moving ion (b), followed by spontaneous emission in random direction (c).

Shortly afterwards, depending on the transition strength, the ion will relax into the ground state by emission of a photon (Fig. 2.5c) with momentum $\vec{k}_e$. The net momentum transfer to the ion after n absorption-emission cycles can be written as

$$\Delta p = \sum_n \hbar \vec{k}_L + \sum_n \hbar \vec{k}_e = n\hbar \vec{k}_L + \hbar \underbrace{\sum_n \vec{k}_e}_{=0} . \tag{2.31}$$

While the recoil from the absorption of the laser photons is always in the same direction, the emission is distributed over all directions and effectively the recoil momentum cancels.

Energetically, the photons emitted by the ions have a higher energy in the laboratory frame than the absorbed photons. Hence, the kinetic energy of the ions is effectively transferred into the radiation field and, after a number of absorption-emission cycles, the motion of the ion along the laser beam direction is cooled.

The scattering of the photons leads to a frictional force which slows the ion down [36]

$$F_{\text{scatt}} = (\text{photon momentum}) \times (\text{scattering rate}). \tag{2.32}$$

The photon momentum is $\hbar k_L$ and the scattering rate is

$$R_{\text{scatt}} = \Gamma \rho_{22}, \tag{2.33}$$

where Γ is the transition linewidth and ρ_{22} is the fraction of the population in the upper level, given by the optical Bloch equations ([37, 38]) which leads to

$$R_{\text{scatt}} = \frac{\Gamma}{2} \frac{\Omega^2/2}{\delta^2 + \Omega^2/2 + \Gamma^2}. \tag{2.34}$$

Assuming the ion movement along one axis and small ion velocities $v \ll c$, there is an "effective", Doppler-shifted ion resonance frequency in the laboratory rest frame

$$\nu_0' = \nu_0 \left(1 - \frac{v}{c}\right). \tag{2.35}$$

Even when the frequency of the incoming photon is not matching the new resonance frequency, there is still a chance of interaction which is taken into account by the frequency detuning

$$\delta = 2\pi(\nu_L - \nu_0'). \tag{2.36}$$

Considering the relationship between the Rabi frequency Ω and the saturation intensity [36, 38]

$$\frac{I}{I_{\text{sat}}} = 2\frac{\Omega^2}{\Gamma^2} \tag{2.37}$$

with

$$I_{\text{sat}} = \frac{\pi}{3} \frac{hc}{\lambda_0^3} \Gamma \tag{2.38}$$

where λ_0 is the transition wavelength, the force can be then written as

$$F_{\text{scatt}} = \hbar k_L \frac{\Gamma}{2} \frac{I/I_{\text{sat}}}{1 + I/I_{\text{sat}} + 4\delta^2/\Gamma^2} \tag{2.39}$$

and it is, as expected, proportional to the laser intensity as long as the intensity is below the saturation value whereas it approaches its maximum value

$$F_{\max} = \hbar k_L \frac{\Gamma}{2} \tag{2.40}$$

for intensities $I \gg I_{\text{sat}}$. In the most typical case, the laser intensity is about the saturation intensity while the detuning is small and the transition is strong

$$F_{\text{scatt}} = \hbar k_L \frac{\Gamma}{4} \quad \text{when} \quad \begin{cases} I = I_{\text{sat}} \\ \delta \ll \Gamma. \end{cases} \tag{2.41}$$

At saturation intensity, the radiation force will accelerate an ion of mass m according to

$$a_{\max} = \frac{F_{\max}}{m} = \frac{\hbar k_L}{m} \frac{\Gamma}{4} = \frac{1}{4} \frac{v_r}{\tau} \tag{2.42}$$

where τ is the lifetime of the excited state and

$$v_r = \frac{\hbar k_L}{m} = \frac{h}{\lambda m} \tag{2.43}$$

is the recoil speed and represents the change of the ion speed after the absorption or the emission of a photon of wavelength λ.

With the aid of Eq. (2.42), the cooling distance, respectively the cooling time, for a hot ion can be roughly estimated. In an ideal case, the acceleration is constant and close to the maximum value. The cooling limit is given by the Doppler cooling limit[36]

$$k_B T_D = \frac{\hbar \Gamma}{2}. \tag{2.44}$$

While for an atom in a magneto-optical trap it is necessary to have six laser beams to address all possible directions of motion, for a bound ion in an ion trap only a single laser beam is sufficient. The laser should be tilted relative to the z-axis in order to address all motions simultaneously though, in a real trap, the motions are coupled and cooling of a single motion can work almost as well.

However, one has to keep in mind that after a few absorption-emission cycles, the ion is not in resonance with the laser anymore. Thus, the description above might be valid for the least energetic ions, since in that case, the laser frequency can be swept rapidly in order to maintain the resonance. A potential technical difficulty arises for ions in the 100 eV range. For these ions, the laser frequency would have to be either

- red-shifted with a few 10 GHz and then tuned very fast to small detunings (chirp cooling) which is equivalent to $\delta = 0$ in (2.39)

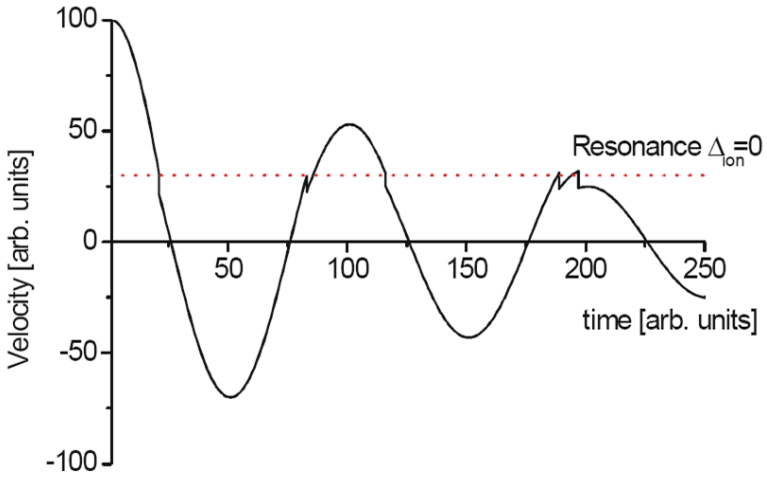

Figure 2.6: Reduction of the axial ion speed in a Penning trap as a result of absorption near the turning points. The figure is taken from [39].

- or kept fixed, but red-shifted for a cold ion. This results in small interaction rates and thus very long cooling times (tens of minutes), equivalent to a large value for δ in (2.39) and a corresponding weak cooling force.

At SPECTRAP, a special case has to be considered: Here, energetic ions are stored inside a Penning trap. A large part of the energy is contained in the motion. During the axial oscillation, the ion passes through all speed values between 0 at the turning point and the maximum kinetic energy at the center of the trap. A red-shifted laser with a fixed small detuning and sufficiently high intensity, aligned along the trap axis, can interact with the ion each time it is approaching the one or leaving the other turning point. A condition for this to happen efficiently is that the Rabi frequency is much higher than the axial frequency from (2.16)

$$\omega_z \ll \Omega. \tag{2.45}$$

When this condition is fulfilled, the ion will practically oscillate along the axis much slower than the time required for the transition to the excited state to occur. Using a laser with sufficient intensity, i.e. close to or above saturation, the ion will most probably absorb a photon near each turning point as illustrated in Fig. 2.6, taken from [39]. The scattering rate in (2.33) will be $2\omega_z/2\pi$ and the scattering force in Eq. (2.32) can be written as

$$F_{\text{scatt}} = \hbar k_L \frac{\omega_z}{\pi} \tag{2.46}$$

and will typically lead to a faster cooling for the fast ions with a fixed laser detuning.

2.3.3 Sympathetic Cooling

Though it is a highly efficient cooling method for ions in a trap, laser cooling is restricted to ions with a favorable energy level structure. Nevertheless, it is still possible to cool any type of ion by Coulomb interaction with laser cooled ions, provided that their charge states are of the same sign [33, 40]. Moreover, this indirect way allows continuous cooling without the necessity of turning the laser off while performing spectroscopy. This allows longer measurements times at lower temperatures.

If the ions to be cooled are placed in a trap together with a laser-cooled ion cloud, the mutual Coulomb interactions between the two species will give rise to a continuous transfer of energy from the hot ions to the cold ions. If this energy flow is not too large for the heat capacity of the laser-cooled ion cloud and for the energy dissipation by the laser interactions, the hole assembly can become a cold plasma.

Unfortunately, for sympathetic cooling of HCI there is no successful experiment mentioned in the scientific literature. Thus, it is rather difficult to precisely evaluate the requirements for this type of experiments. Nevertheless, based on previous experiments involving the symphatetic cooling of simple ions [33, 40] and on the simulations describing the cooling of HCI by a laser-laser cooled Mg^+ ions [41, 42, 43], several boundary conditions can be noted. The hole assembly can become a cold plasma when the laser cooling force is greater than the Coulomb heating interactions, which means that:

- the laser-cooled ions are always in resonance with the cooling laser and/or
- the laser power, detuning and spatial overlapping is optimal and/or
- the laser-cooled ion cloud is much larger in number than the hot ions and/or
- the difference in temperature between the hot and cold ions is fairly small.

In a cold plasma, the coupling between the ions can be very strong when the plasma parameter [44]

$$\Gamma_p = \frac{E_{\text{Coulomb}}}{E_{\text{Thermal}}} = \frac{1}{4\pi\epsilon_0}\frac{Q^2e^2}{a_{\text{WS}}k_BT} \tag{2.47}$$

exceeds unity [41, 45]. Here, Q is the charge state of the laser-cooled ion and

$$a_{\text{WS}} = \left(\frac{3}{4\pi n}\right)^{1/3} \tag{2.48}$$

is the Wigner-Seitz radius [42] which characterizes the inter-ion spacing in a Coulomb crystal, once the plasma of volume density n undergoes a phase transition [46].

In this case, the time scale of the plasma reaction to an incoming ion is given by the plasma period, τ_p, defined by the plasma frequency for ions with mass m [41, 43, 47]

$$\omega_p = \frac{2\pi}{\tau_p} = \sqrt{\frac{Q^2 e^2 n}{\epsilon_0 m}}. \tag{2.49}$$

Considering the Coulomb force, the heat transfer process from the incoming ion to the laser cooled plasma is more efficient when the charge state of the incoming ion is higher[1]. This also means that this cooling method is particularly suitable for highly charged ions.

2.4 Laser Cooling of Mg^+ Ions - Overview

Laser cooling has proved to be a versatile tool for very fast cooling of ions or atoms down to mK temperatures. Yet, as already stated, this method is restricted to ions with favorable structure of the energy levels. It is recommendable that the ion has a closed transition between the ground state and the excited state - without dark states. Also, the transition frequency should be in the laser-accessible region.

The aim of this thesis is the setup of a system to cool ions in a trap to a very low temperature regardless of their charge state, energy level structure or other parameters. This will be achieved using sympathetic cooling. Therefore, one needs a trap filled with laser cooled ions which implies the necessity of an ion species suitable for laser cooling and a laser system capable of delivering a tunable, narrow linewidth laser beam at the wavelength of interest. For our experiment we have chosen $^{24}Mg^+$ ions and to build a laser system at 279.6 nm consisting of a fiber laser emitting at 1118.5 nm and two successive second-harmonic generation (SHG) ring cavities for frequency quadrupling [48].

The choice of using $^{24}Mg^+$ ions is obvious through the fact that ^{24}Mg is a natural occurring, abundant and non-toxic element with a convenient structure of energy levels, without any dark states between the levels implied in the transition used for cooling as shown in Fig. 2.7 [49]. For comparison, the energy levels of Ca^+ are provided. The Ca^+ ion can easily decay in the $3d$ dark state after the initial excitation. Thus, in order to successfully laser-cool Ca^+ ions, an additional laser has to be used to repump the ions in the $4p$ state.

[1] the charge state of the laser-cooled ion is restricted to low values (1+ or 2+) since the transition wavelength should be in the laser-accessible region

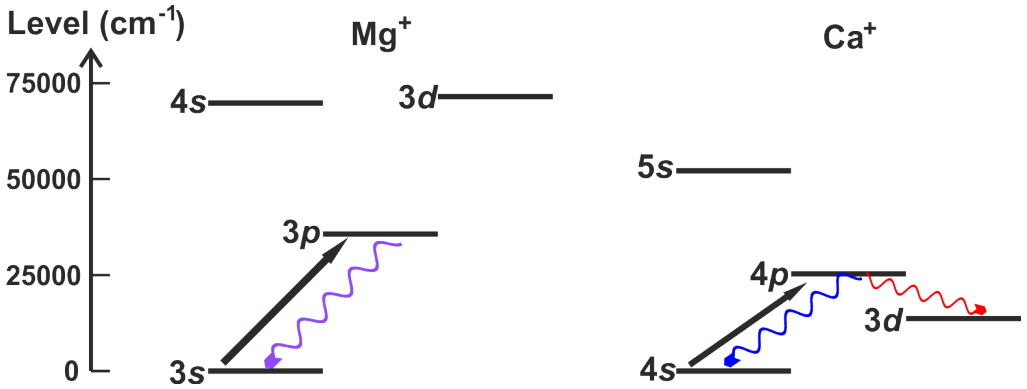

Figure 2.7: Energy levels of Mg^+ compared to Ca^+.

The apparently more complicated solution of building two SHG stages and using a fiber laser instead of using a dye laser and only one SHG stage is motivated by considering that, over the last years, the fiber laser proved to be a high power, reliable and stable laser source [50], whereas dye lasers still require an expensive pump laser and require much more care for stable operation. Alternatively, there is also the possibility to use two lasers for sum frequency generation and two ring cavities [51] but this would even increase the maintenance effort. The simplicity of operation is of key importance for online applications like at HITRAP. Moreover, the nonlinear crystals became widely available and SHG cavities are in principle commercially available. However, for this experiment the frequency quadrupling was realized without commercial doublers. Furthermore, the laser beam emitted by the fiber laser has a very narrow linewidth ($\delta\lambda$<200 kHz) and an excellent quality factor (M^2<1.05) [52].

2.5 Nonlinear Optics

2.5.1 Principles of Second Harmonic Generation

Nonlinear optical effects were first observed in the 19th century in form of the Pockels and Kerr effects. However, it was not until the development of the laser in the 1960s that the study of the behavior of light in optical materials at higher intensities became possible. This led to the discovery of second harmonic generation or frequency doubling in 1961 [53] as a special case of a frequency mixing process.

When a laser wave passes through a linear and isotropic optical medium, the polarization density vector of the material is collinear with and proportional to the electric field

[54, 55]

$$\vec{P}(t) = \epsilon_0 \chi^{(1)} \vec{E}(t) \tag{2.50}$$

where ϵ_0 is the electric vacuum permittivity and $\chi^{(1)}$ the linear electric susceptibility of the medium. In a nonlinear optical medium, the polarization can be written as a power series of the electric field

$$\vec{P}(t) = \epsilon_0(\chi^{(1)}\vec{E}(t) + \chi^{(2)}\vec{E}^2(t) + \chi^{(3)}\vec{E}^3(t) + ...) \tag{2.51}$$

where $\chi^{(2)}$ and $\chi^{(3)}$ are the second and the third-order nonlinear susceptibility, describing the strength of the second and third-order nonlinear effects respectively. In order for the power series to converge, the following relationship must be satisfied

$$\chi^{(1)}\vec{E}(t) \gg \chi^{(2)}\vec{E}^2(t) \gg \chi^{(3)}\vec{E}^3(t). \tag{2.52}$$

The higher terms are thus too small and can be ignored. The dependence between the polarization density and the electric field is linear for small values of the field but becomes nonlinear for high values of the field as illustrated in Fig. 2.8 [55].

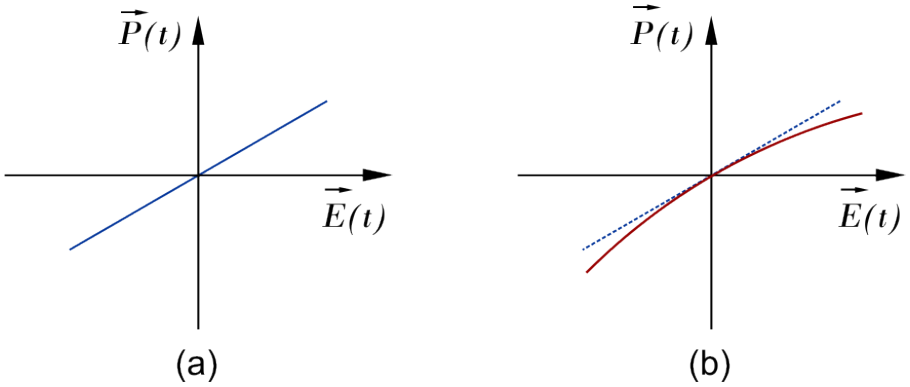

Figure 2.8: The dependence between the polarization density and the electric field for a linear optical medium (a) and for a nonlinear medium (b) [55].

If we consider a medium which exhibits second order susceptibility $\chi^{(2)}$ and we write the electric field of a laser beam passing through the medium as [54]

$$\vec{\mathcal{E}}(r,t) = \vec{E}(r)e^{-i\omega t} + \vec{E}^*(r)e^{i\omega t} \tag{2.53}$$

the polarization density corresponding to the second order term from Eq. (4.6) becomes

$$\vec{P}^{(2)}(t) = \chi^{(2)}(|E|^2 e^{-2i\omega t} + |E|^2 e^{2i\omega t}) + 2\chi^{(2)}EE^*. \tag{2.54}$$

The resulting second-order polarization density contains a term with frequency 2ω corresponding to the second-harmonic generation and a term at zero frequency (DC) corresponding to the optical rectification [56], a process discovered in 1962 in which a static electric field is created in the medium. The process can be graphically illustrated as shown in Fig. 2.9 [55].

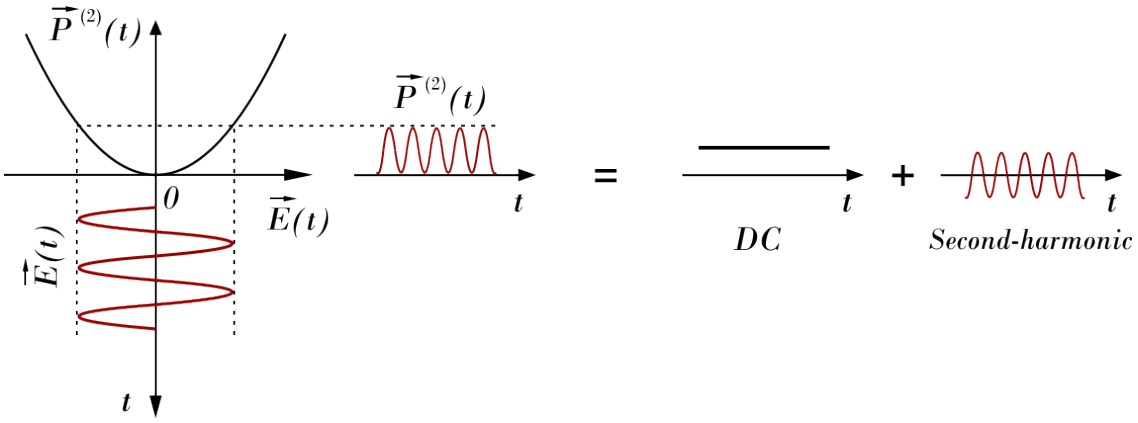

Figure 2.9: A harmonic electric field passing through a second-order nonlinear medium generates a polarization with a component at double frequency (second harmonic) and one at zero frequency (optical rectification) [55].

By passing a laser beam through a nonlinear medium, it is thus possible to generate the second harmonic of the incident beam. Typical nonlinear media are birefringent crystals, though SHG was also demonstrated in media like glass fibers or even air [57].

2.5.2 Phase Matching

Second harmonic generation can be regarded as a process in which two waves of frequency ω are combined for creating a wave of frequency 2ω. In order for this process to be efficient, the interacting waves should be in phase along the propagation direction. This condition is called phase matching and leads to the constructive addition of amplitude contributions from different locations.

The condition of phase-matching can be easily explained in terms of photon mixing process where two photons of frequency ω are destroyed and a photon of frequency 2ω is created within the crystal, as in Fig. 2.10. The conservation of energy and momentum requires that the following relationships are satisfied [55]

$$\hbar\omega + \hbar\omega = \hbar(2\omega) \tag{2.55}$$

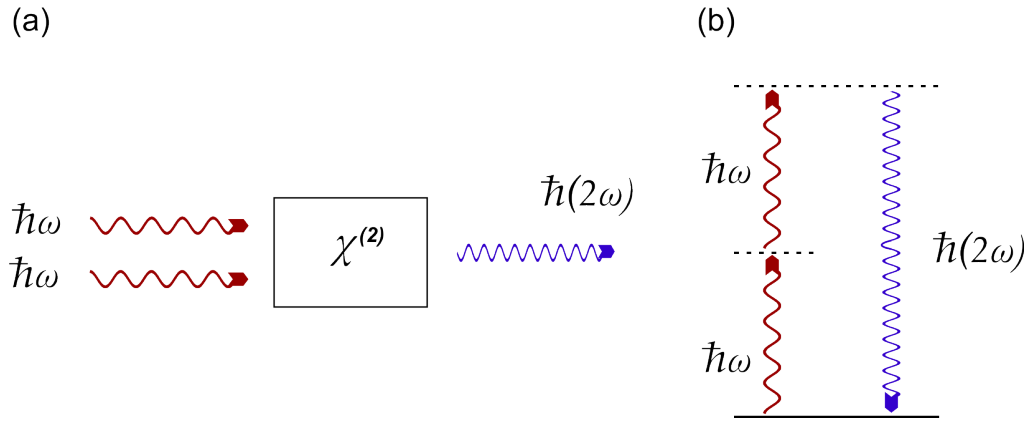

Figure 2.10: Second harmonic generation as a process in which two photons are destroyed and a photon of double frequency is created. The dashed lines represent virtual energy levels.

$$\hbar\vec{k}_{\omega}^{(1)} + \hbar\vec{k}_{\omega}^{(2)} = \hbar\vec{k}_{2\omega} \tag{2.56}$$

where $\vec{k}$ represents the wavevector of a photon. These relationships can be written as

$$\omega + \omega = 2\omega \tag{2.57}$$

representing the self-evident frequency-matching condition and

$$\vec{k}_{\omega}^{(1)} + \vec{k}_{\omega}^{(2)} = \vec{k}_{2\omega} \tag{2.58}$$

representing the phase-matching condition.

For the simple experimental case when the interacting photons or waves are collinear, Eq. (2.58) is equivalent to

$$n_{\omega}^{(1)} + n_{\omega}^{(2)} = 2n_{2\omega} \tag{2.59}$$

where n represents the refractive index of the medium. Because of the chromatic dispersion, this condition is usually not fulfilled. However, in birefringent crystals, the refractive index depends on the polarization of the waves and their directions relative to the principal axes. Hence, condition 2.59 can be compensated for the dispersion by proper selection of polarization, temperature and orientation of the crystal.

There are two types of phase-matching depending on the polarization of the waves [58]:

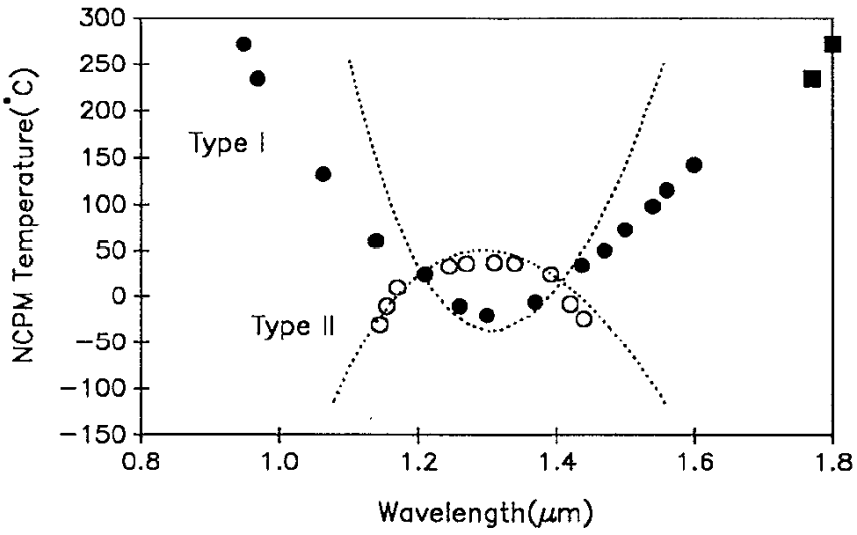

Figure 2.11: The temperature for non-critical phase-matching versus the wavelength of the incident wave in lithium triborate (LBO) [59]. The circles are measured data while the dashed lines are calculations according to the theory.

1. Type I phase-matching: The incident waves have the same polarization while the second harmonic has a polarization perpendicular to the incident waves. This means that a single incident beam can be used and Eq. (2.59) becomes

$$n_\omega = n_{2\omega}. \tag{2.60}$$

2. Type II phase-matching: The two incident waves have different polarization and it requires the splitting of the incident beam. This generally yields a significantly smaller conversion efficiency and is used when the birefringence is relatively strong or for other types of frequency mixing processes.

The refractive index along the two or three axis of the crystal at a particular frequency can be calculated using the empirical Sellmeier equations for a particular crystal, which are typically provided by the manufacturer or can be found in scientific articles. Considering the collinear waves in type I geometry - with only one incident beam, called fundamental - the phase-matching condition (2.59) can be obtained in two ways:

1. Non-critical phase-matching (NCPM) uses the variation of the refractive index of the crystal with the temperature. The temperature of the crystal is adjusted until the refractive index at frequency ω with the corresponding polarization becomes equal

with the refractive index at frequency 2ω with the corresponding perpendicular polarization. The variation of the refractive index with the temperature or the phase-matching temperature can be found in articles or in the product datasheet. An example of phase-matching temperature curve of lithium triborate (LBO) from [59] is provided in Fig. 2.11.

2. Critical phase-matching (CPM) uses the orientation of the crystal. Typically, depending on the sign of the birefringence, one of two beams has the ordinary polarization, perpendicular on the optic axis, while the other is polarized at some variable angle in the plane described by the optic axis and the beams direction. Thus, the second beam has an extraordinary polarization and the refractive index is given by [55]

$$\frac{1}{n^2(\theta,\omega)} = \frac{\sin^2(\theta)}{n_e^2(\omega)} + \frac{\cos^2(\theta)}{n_o^2(\omega)} \tag{2.61}$$

where θ is called the cut angle of the crystal and measures the angle between the optic axis and the beams direction of propagation. Since the ordinary polarization has a constant refractive index, Eq. (2.59) can be fulfilled by choosing the cut angle θ correctly. An example of a critical phase-matching curve of beta-barium borate (BBO) as provided by Fujian Castech Crystals, Inc. [60] is illustrated in Fig. 2.12.

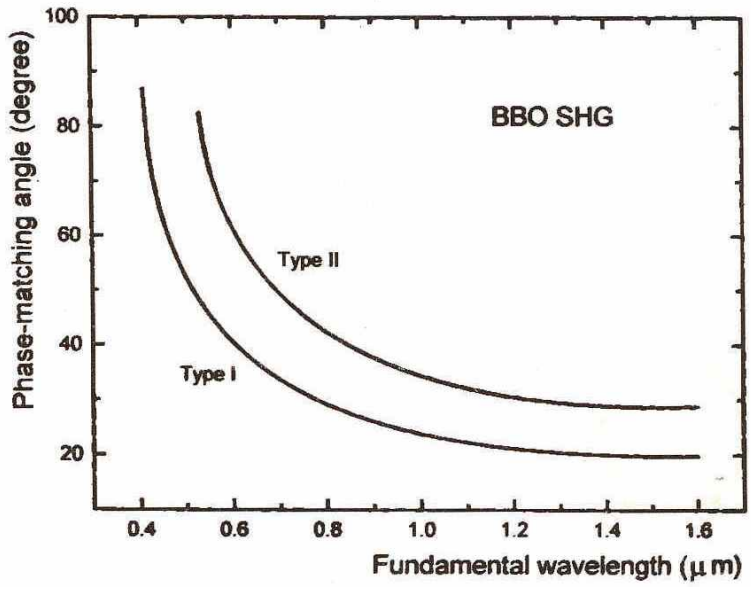

Figure 2.12: Critical phase matching tuning curves of beta-barium borate (BBO) for second harmonic generation [60].

For an uniaxial crystal, CPM can be either o-o-e or e-e-o. The first two letters describe the polarization of the fundamental wave(s) (identical for Type I) while the last letter describes the polarization of the second harmonic wave. Taking the chromatic dispersion and Eq. (2.61) into account, Type I CPM is physically possible in e-e-o configuration for positive birefringence and in o-o-e configuration for negative birefringence. The plane containing the optical axis and the laser beam is called tangential while the plane containing the laser beam but perpendicular on the optic axis is called sagittal.

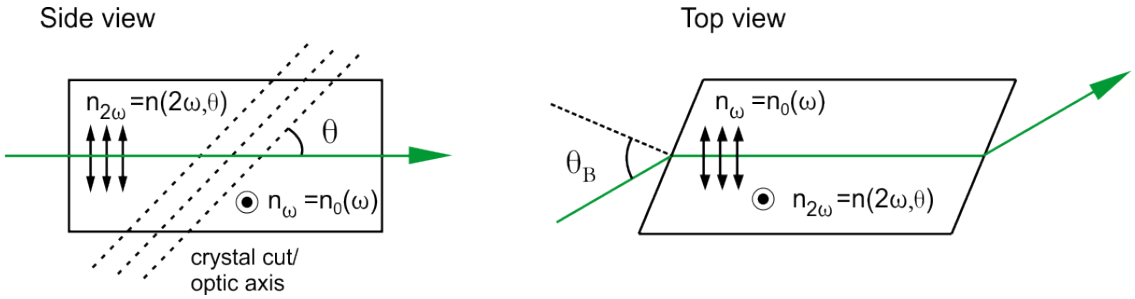

Figure 2.13: A beta-barium borate (BBO) crystal used for second harmonic generation in critical phase-matching Type I o-o-e configuration: the crystal cut angle is θ; in the top view, the faces are at Brewster angle (θ_B) relative to the incident beam.

An example of Type I o-o-e for a Brewster-cut negative uniaxial birefringent BBO as typically used in experiments for SHG is depicted in Fig. 2.13. In the case of a biaxial birefringent crystal like LBO, the CPM can be obtained also for a ϕ cut, which is the angle between the laser beam and the other optic axis. In order to distinguish between the two cutting types, the value of the other angle or the crystal plane in which the laser beam propagates is given. Thus, for example, CPM Type II e-o-o in YZ plane($\phi = 90^o$) with a $\theta = 30^o$ crystal cut means that

- the critical phase-matching solution is used;
- there are two incident waves which have ordinary and extraordinary polarization while the harmonic has ordinary polarization;
- the beams propagate in the YZ plane which is equivalent to an angle between the beam direction and the X axis $\phi = 90^o$;
- the crystal is orientated or cut so that the angle between the Z axis and the beam direction is $\theta = 30^o$.

2.5.3 Boyd-Kleinmann Theory

For designing the SHG stages, the Boyd-Kleinmann theory [61] was used. Choosing the crystal type and length can be a real challenge given the multitude of nonlinear crystal types present on the market. As a general rule, it is preferable to use NCPM instead of CPM for the same or comparable crystals. NCPM has many advantages, which are: non-astigmatic Gaussian beam output, higher efficiency, simple optimization, larger acceptance angle and wavelength bandwidth and no walk-off angle.

The walk-off angle is the angle between the direction of beam propagation and the propagation direction of the energy, which imposes a limit on the interaction length. It occurs in CPM because one of the beams has extraordinary polarization so that its refractive index and the phase velocity depends on the θ crystal-cut angle. In case of NCPM, both beams have ordinary polarization and the walk-off angle is 0.

According to the Boyd-Kleinmann theory, the harmonic power depends on several factors [61, 62]

$$P_{2\omega} = \left\{ \frac{16\pi^2 d_{\text{eff}}^2}{\lambda^3 \epsilon_o n^2 c} \right\} \cdot L \cdot e^{-(\alpha_1 + 0.5\alpha_2)L} \cdot h(\sigma, \beta, \kappa, \xi, \mu) \cdot P_\omega^2 \tag{2.62}$$

d_{eff} is the effective nonlinear coefficient, ϵ_o is the vacuum permittivity, n is the refractive index of the crystal at phase-matching, L is the length of the crystal, α_1, α_2 are the absorption coefficients of the crystal for the fundamental and the second harmonic, respectively, and P_ω is the power of the fundamental beam.

The first term is constant under normal circumstances. The function h is the so-called function of optimizable parameters and depends on

- σ - a phase mismatch factor depending on the confocal parameter of the laser beam b and the fluctuations in the wavenumber of the laser inside the crystal

$$\sigma = \frac{1}{2} b \Delta k \tag{2.63}$$

- ξ - the focusing parameter which gives the optimum confocal parameter of the laser beam as a function of crystal length for a given walk-off angle (ρ) of the laser inside the crystal

$$\xi = \frac{L}{b} \tag{2.64}$$

- β - a walk-off factor depending on the optimum focusing parameter ξ, the crystal length, the wavenumber k of the fundamental laser beam inside the crystal and the walk-off angle ρ

$$\beta = \frac{1}{2}\rho\sqrt{\frac{Lk}{\xi}} \tag{2.65}$$

- κ - an absorption factor depending on the the confocal parameter and the absorption coefficients for the harmonic and fundamental laser beams

$$\kappa = \frac{b(\alpha_1 - \frac{1}{2}\alpha_2)}{2} \tag{2.66}$$

- μ - a factor which measures the displacement of the laser focus from the center of the crystal. It depends on the relative position of the laser focus f from the entrance of the crystal

$$\mu = \frac{L - 2f}{L}. \tag{2.67}$$

The general form of the function h is

$$h(\sigma, \beta, \kappa, \xi, \mu) = \frac{e^{\mu\alpha L}}{4\xi} \int \int_{\xi(1-\mu)}^{\xi(1+\mu)} \frac{\exp[-\kappa(\tau + \tau') + \mathrm{i}\sigma(\tau - \tau') - \beta^2(\tau - \tau')^2]}{(1 + i\tau)(1 - i\tau)} d\tau d\tau' \tag{2.68}$$

and can be numerically calculated for a given specific SHG case.

2.6 Hänsch-Couillaud Locking Scheme

Nonlinear crystals have a very low doubling efficiency. But according to Eq. (2.62), the harmonic output power depends on the square of the input power. It is therefore helpful to use input power levels as high as possible. While for pulsed lasers, which provide high peak powers arising from high pulse energies and/or short pulse length, high efficiencies can be reached, it is usually required to increase the power artificially using an optical resonator to obtain high doubling efficiencies for continuous wave lasers.

The length of the optical resonator has to be maintained within a small fraction of the wavelength of the light in order to keep the resonance condition. Since the optical resonator is subject to various external perturbations, its length has to be dynamically stabilized with fast electronics. This process is called locking of the resonator. A typical finesse for an SHG cavity is about 100 and the output fringes corresponding to the resonances are very sharp.

The two locking schemes used for the stabilization of SHG cavities are Pound-Drever-Hall [63, 64] and Hänsch-Couillaud (HC) [65]. The Pound-Drever-Hall scheme, though experimentally more stable, uses frequency modulation of the incoming laser and thus requires a fairly expensive electro-optical modulator. The HC scheme offers an inexpensive alternative: It requires a polarization-selective cavity and a polarization analyzing assembly.

The polarization-selective element in an SHG cavity is the birefringent nonlinear crystal itself. The cavity is then optimized for one polarization of the incoming laser beam - typically the horizontal linear polarization. The polarization of the incoming laser beam is adjusted via a half-wave ($\lambda/2$) plate to be almost horizontal [66]. Typically, the angle between this polarization and the horizontal plane is around 5°. To change the cavity length, one of the mirrors is mounted on a piezo-electric transducer (PZT). For scanning the cavity, a triangle signal is applied to the PZT with an amplitude sufficiently high to scan through several longitudinal modes of the cavity.

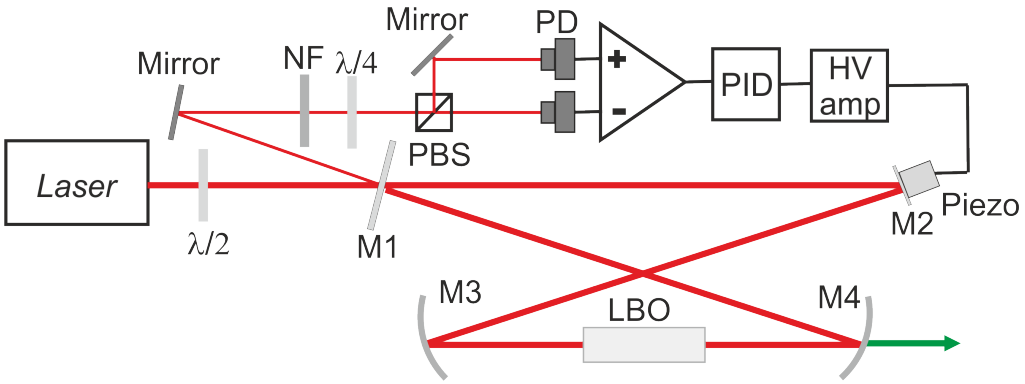

Figure 2.14: Schematic layout of the Hänsch-Couillaud locking scheme (M1-M4: cavity mirrors, $\lambda/4$ and $\lambda/2$: quarter- and half-wave plate respectively, NF: neutral density filter, PBS: polarizing beam splitter, PD: photodiode, PID: proportional-integral-derivative controller, HV amp: high voltage amplifier).

When the cavity is at resonance, the horizontal part of the laser polarization sees a low loss cavity and will consequently experience a low reflection, while the vertical part is reflected and is used as a phase reference. The horizontal polarization acquires a resonance-dependent phase shift relative to the vertical one inside the cavity. Exactly at resonance, the two polarization components are still in phase since the phase acquired in one round trip inside the cavity is an integer multiple of 2π and the overall reflected beam is therefore linearly polarized. Near the resonance, the phase acquired in the round

trip is different from 2π and, thus, the horizontal component returning from the cavity is phase-shifted relative to the vertically polarized beam. Hence, the overall reflected beam is elliptically polarized, with the ellipticity proportional to the detuning from the resonance. Moreover, the handedness depends on the sign of the detuning.

The polarization of the reflected beam is analyzed in the polarization analyzing assembly shown in the upper part of Fig. 2.14. The assembly consists of a quarter-wave ($\lambda/4$) plate, a polarization beam splitter and two photodetectors connected to a differential amplifier. The $\lambda/4$ plate is adjusted for having the axis at 45° relative to the polarization axis of the beam splitter. When the incoming beam is linearly polarized - at resonance or far away from it - the $\lambda/4$ plate converts it to circular polarization and two beams with equal intensities emerge from the beam splitter and are detected on photodiodes connected to the differential amplifier. Hence, the output of the amplifier will be zero.

Off-resonance, the beam acquires an elliptical polarization, which can be considered as a superposition of two counter rotating circularly polarized components with different amplitudes. The $\lambda/4$ plate converts these two components in linearly polarized components and the beam splitter with the differential photoamplifier allows the measurement of the difference in their amplitude. This difference is proportional to the phase shift acquired in the resonator round trip, which in turn is proportional to the detuning from the resonance.

The signal from the differential photoamplifier is given by the function [65, 67]

$$I_a - I_b = 2\ I^{(i)} \cos\,\theta\ \sin\,\theta \frac{\mathrm{T_1 R}\ \sin\,\delta}{4\mathrm{R}(1-\mathrm{R})^2\ \sin^2\frac{\delta}{2}} \tag{2.69}$$

where $I^{(i)}$ is the intensity of the incident laser beam, θ is the angle between this polarization of the incident laser beam and the horizontal plane, T_1 is the transmissivity of the cavity entrance mirror, R is the cavity roundtrip reflectivity and δ is the phase shift acquired by the horizontal part inside the cavity. Increasing the tilt of the polarization of the incoming laser beam relative to the horizontal will result in a better signal to noise ratio through $\cos\,\theta\ \sin\,\theta$, but at the expense of the laser power inside the cavity. This function is plotted in Fig. 2.15 and it has a slowly decreasing slope between the resonances. The sign of this slope is opposite to the sign of the locking slope, offering the possibility of automatic relocking by the electronics. Thus, it is an optimal error signal for the cavity locking servo loop.

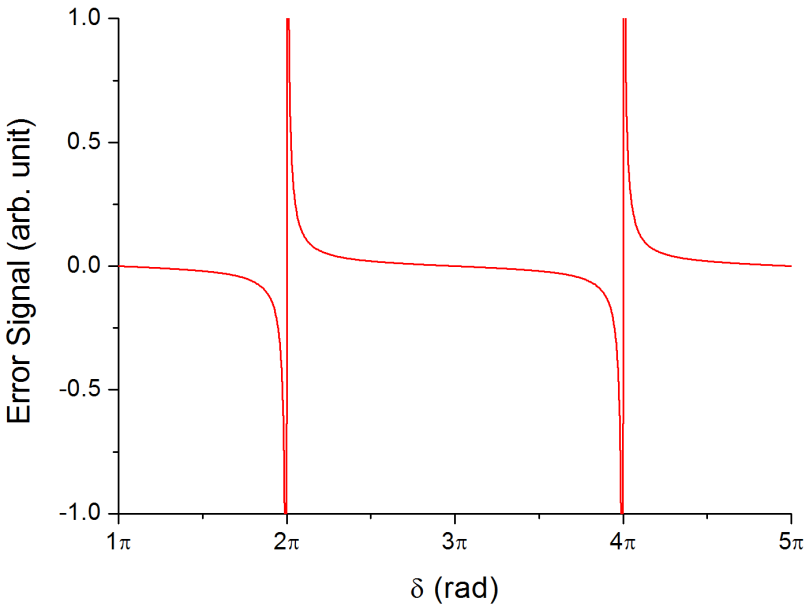

Figure 2.15: Calculated Hänsch-Couillaud error signal according to (2.69) for servo locking.

3

Experimental Setup

3.1 The Fiber Laser

As already stated in the previous chapter, the laser system at 279 nm consists of a single-mode fiber laser at 1118 nm and two cavities for second harmonic generation to obtain frequency quadrupling. The laser is a Koheras Boostik fiber laser [52], specified to deliver 1.66 W maximum output power, but a maximum of 1.2 W including the amplified spontaneous emission (ASE) was observed.

A fiber laser usually consists of a master oscillator and one or two amplifying stages [50, 58]. The master oscillator for this laser is a distributed feedback (DFB) [68] ytterbium-doped fiber pumped by a diode laser. A periodic perturbation in the refractive index of the fiber middle forms the Bragg grating [69] which allows for wavelength selection and for the narrowing of the linewidth (Fig. 3.1).

There is a trade-off between the doping concentration of the fiber and the possibility to write the Bragg grating, which limits the output to only a few ten milliwatts [70]. The output of the master oscillator is therefore used to seed a fiber amplifier [71] which again uses a doped fiber as a gain medium, as depicted in Fig. 3.2. The pump power of the ytterbium doped fiber is provided by two high power diode lasers around 976 nm,

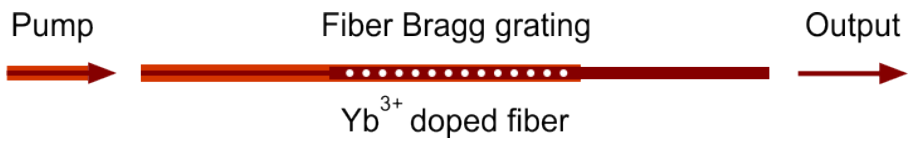

Figure 3.1: The gain medium of a distributed feedback (DFB) fiber laser with the Bragg grating in the middle.

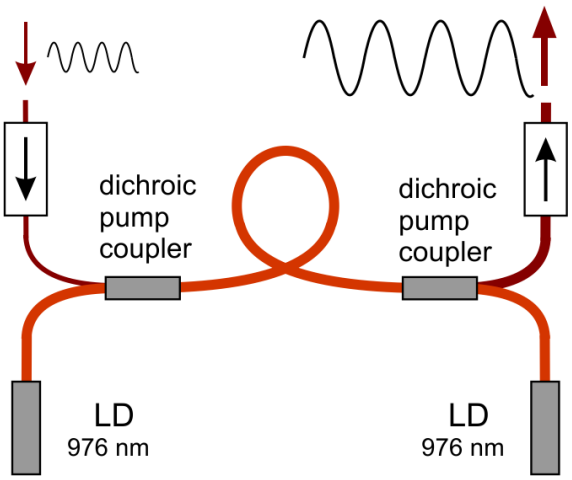

Figure 3.2: A typical ytterbium-doped fiber amplifier (LD: Laser diode for optical pumping).

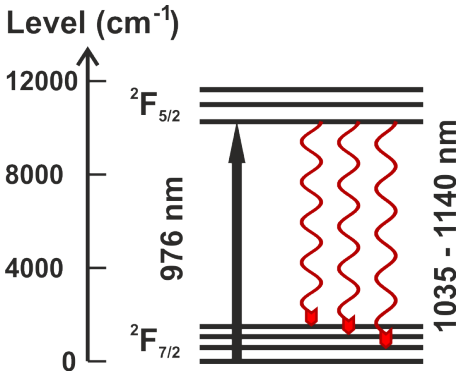

Figure 3.3: Energy levels of Yb^{3+} consisting of two groups with four, respectively three Stark levels.

amplifying the 1118 nm radiation coming from the first stage. Two optical isolators are used in order to prevent the back reflections. For reference, the energy level structure of Yb^{3+}, with the levels involved in the amplification, is provided in Fig. 3.3 [72, 73]. The main levels are splitted in four, respectively three sublevels by the Stark effect, caused by the "glass field" [74].

The gain is typically limited by the increasing level of ASE and not by the available pump power. To overcome this limit, a second amplifier or amplifier chains can be used. The master laser used here provides a seed power of 40-60 mW, the first amplifier delivers up to 500 mW while the last "booster" amplifier delivers up to about 2 W theoretically.

The fiber laser has some very nice specifications as seen in Table 3.1. Unfortunately, an output power of 1.66 W was never obtained and, after several complications and

Table 3.1: Technical specifications of the Koheras Boostik fiber laser.

Parameter	Value	Unit
Output power	1.66	W
Wavelength (at approx. 33 ^{o}C)	1118.5408	nm
Linewidth	<70	kHz
Beam quality, $\mathbf{M}^2$	<1.05	
Optical SNR (50 pm res.)	>61	dB
A_{sign}/A_{noise}	>1000	
10 hours power variation at max. power	<12	%
Thermal tuning range (25-45 ^{o}C)	450	pm
Piezo tuning range (0-200 V)	19	pm

repairs, described in detail in Appendix A.1, operation was only possible with <1 W total power. Moreover, it turned out that the master oscillator is running on two modes, with perpendicular polarization and a mode distance of ≈1.5 GHz. Thus, less than 500 mW laser power was available for quadrupling in the final setup.

Apart from these unpleasant reliability problems, the fiber laser proved to be an optimum source in terms of beam quality, linewidth and stability for SHG. The output wavelength can be tuned via a piezo which stretches the seeding fiber for fine and fast adjustments or via the temperature of the fiber for rough and slow adjustments.

3.2 Design of the First Resonator

For SHG at 1118 nm, several crystals are capable of NCPM, which is the first option for phase matching: lithium triborate (LBO) [66], lithium niobate (LNO) [75] and potassium niobate (KNO). Optical homogeneity, linear absorption and the amount of inclusions in the crystal are very important for the doubling efficiency once the crystal is placed inside an enhancement cavity. LNO and KNO have a typical optical inhomogeneity of $\delta n \approx 5{\cdot}10^{-5}\mathrm{cm}^{-1}$ compared to only $\delta n \approx 10^{-6}\mathrm{cm}^{-1}$ for LBO which also has less inclusions and lower linear absorption. Moreover, the theoretical temperature for NCPM at 1118 nm is around 90°C for LBO compared to above 200°C for the other two crystals. Thus, for the first SHG cavity, LBO was chosen despite its more than five times smaller nonlinear coefficient compared to the other two crystals (LBO: $d_{\mathrm{eff}} = 1.2$ pm/V, LNO: $d_{\mathrm{eff}} = 6.1$ pm/V and KNO: $d_{\mathrm{eff}} = 21$ pm/V [59]).

3.2.1 Crystal Length and Doubling Efficiency

For our case with NCPM and therefore zero walk-off angle $\rho = 0$, the value of the optimum focusing parameter according to the Boyd-Kleinmann theory is $\xi = 2.84$ [61]. Assuming the focus of the cavity mode in the center of the crystal, $\beta = \mu = 0$, and ξ fixed to the optimum value, the confocal parameter can be expressed as $b = L/\xi$ and we can obtain from (2.63) and (2.66)

$$\sigma = \frac{L}{\xi} k \Delta n \tag{3.1}$$

$$\kappa = \frac{L(\alpha_1 - \frac{1}{2}\alpha_2)}{2\xi}. \tag{3.2}$$

Here we assumed that the fluctuations of the wavenumbers are due to variations of the refractive index Δn inside the crystal. These variations are caused by the optical inhomogeneity of the crystal and the temperature fluctuations of the oven. Thus, $h(\sigma, \beta, \kappa, \xi, \mu)$ depends on the quality of the crystal and the performance of the temperature stabilization as given parameters and only on the crystal length as variable.

The typical fluctuation in the refractive index of LBO is $\delta n_L \approx 10^{-6}$ cm^{-1} due to inhomogeneities and $\delta n_T \approx (7.3 \cdot 10^{-6} - 2.1 \cdot \lambda)$ K^{-1} (λ in meters) due to temperature fluctuations, which is $\Delta T \leq 0.1$ K for our case. The typical absorption coefficients are $\alpha_1 \approx 0.1\%$ cm^{-1} and $\alpha_2 \approx 0.3\%$ cm^{-1}. Taking these parameters into account, the double integral in (2.68) can be solved with Matlab numerically. The function of optimizable parameters $h(L)$ is plotted in Fig. 3.4a for a crystal length from 0 to 200 mm. The optimum crystal length would be 85 mm. However, such a long crystal would result in a strongly reduced angle, temperature and spectral acceptance for SHG.

Introducing the conversion coefficient η, Eq. (2.62) can be written as

$$P_{2\omega} = \eta P_{\omega}^2, \tag{3.3}$$

where η for our case is

$$\eta = \left\{ \frac{16\pi^2 d_{\text{eff}}^2}{\lambda^3 \epsilon_o n^2 c} \right\} L \, e^{-(\alpha_1 + 0.5\alpha_2)L} \, h(L). \tag{3.4}$$

The simulated conversion coefficient η is plotted in Fig. 3.4b for the same virtual crystal length domain. Compared to h, η depends even stronger on the crystal length and also has a maximum at 85 mm. Even with such a hypothetically long crystal, the harmonic output for single pass doubling would be ≈ 1.3 mW for a fundamental input of 1 W.

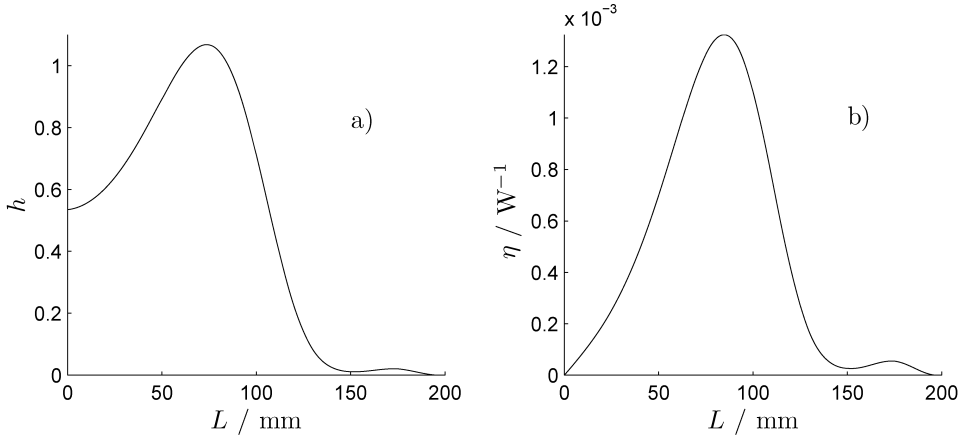

Figure 3.4: The function of optimizable parameters $h(L)$ (a) and the conversion coefficient η (b) for single-pass SHG in LBO at 1118 nm as a function of the crystal length L.

3.2.2 Cavity Enhancement

Equations (2.62) and (3.3) explicitly show that the power level of the fundamental laser is very important for efficient SHG. For a 33 fold increase in fundamental power, the harmonic increases ≈ 1000 times. A 33 fold increase can be easily achieved after placing the crystal inside a ring cavity. The power of the fundamental laser in the cavity is

$$P_{\omega}^{\mathrm{cav}} = A(c_{\mathrm{eff}} P_{\omega}^{\mathrm{inp}}). \tag{3.5}$$

c_{eff} is a coupling efficiency coefficient and it represents the ratio between the power of the fundamental laser in front of the input mirror and the power entering the cavity at resonance. It depends on the laser waist size and position (mode matching) and on the reflectivity of the input mirror.

The enhancement factor A is given by [76]

$$A = \frac{1-r}{(1-\sqrt{rv})^2} \tag{3.6}$$

where r is the reflectivity of the input mirror and v represents the ratio between the laser power after one round trip inside the cavity and the initial power. For a given v, the maximum value of A is for $r = v$. This condition is called impedance matching and actually means that at resonance, the losses inside the cavity are the same as the transmission through the input mirror. A positive side effect of choosing a mirror with a reflectivity in order to meet the conditions for impedance matching is that the coupling efficiency c_{eff} has a maximum for a given laser waist size and position.

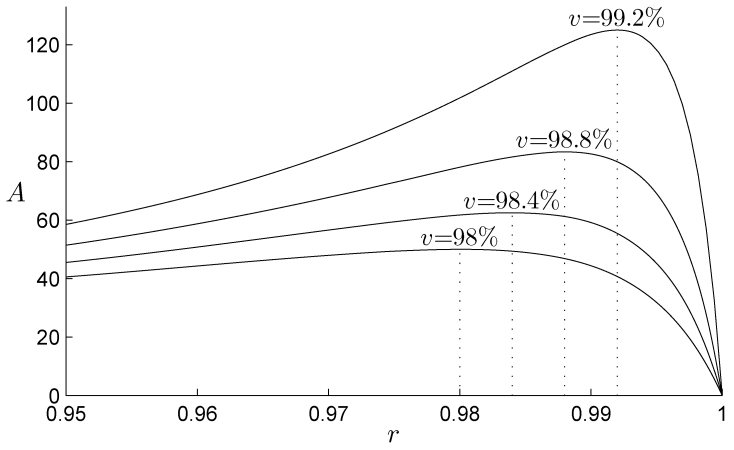

Figure 3.5: The enhancement factor A of a ring cavity as function of input mirror reflectivity and round-trip ratio level v of the fundamental laser.

Compared to a passive cavity, one has to consider that the doubled light power also counts as loss in a cavity for SHG. Hence, the losses v can be written as [77]

$$v = (1 - \alpha_1 L)(1 - \eta P_\omega^{\mathrm{cav}})(1 - t) \tag{3.7}$$

where the first term represents the losses due to linear absorption inside the crystal, the second term represents the losses due to SHG and the last term represents the total losses due to transmission or reflections of the laser on the surfaces inside the cavity.

Under normal circumstances, it is quite difficult to exactly meet the condition for impedance matching, but as it can be seen in (3.6) it is always advisable to have minimum losses by using high reflectivity mirrors, good anti-reflection (AR) coatings on the crystal, short good-quality crystals and by maintaining clean surfaces. In Fig. 3.5, the enhancement factor is plotted versus the reflectivity of the input mirror for four round-trip ratio-levels between 98 and 99.2%. Even with a small change of only 1.2% in the round-trip level, the enhancement factor in the cavity varies by a factor of ≈ 3. Hence, from (3.3) and (3.5), only 1.2% additional losses inside the cavity would lead to an ≈ 9 fold decrease of the harmonic output.

3.2.3 Choice of an Input Mirror and Crystal Length

When choosing the reflectivity for the input mirror, one has to consider the manufacturing tolerance besides the uncertainty in the level of losses inside the cavity. In practice, either

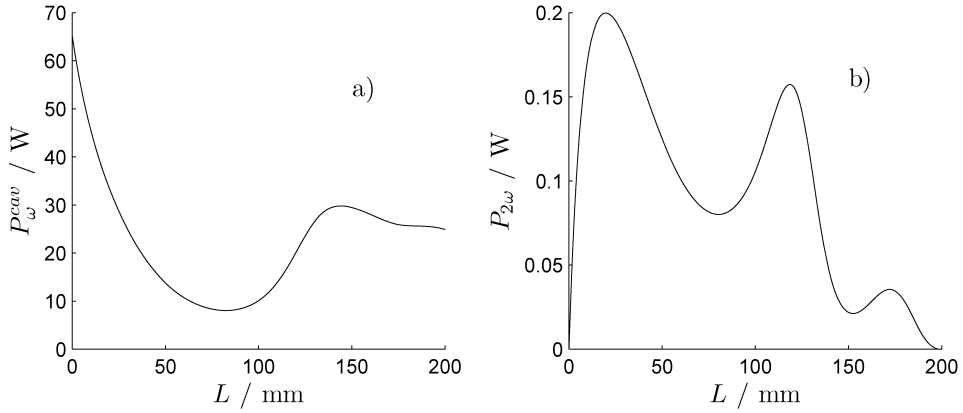

Figure 3.6: The power level of the 1118 nm laser inside the cavity (a) and the expected power level outside the cavity of the laser radiation at 559 nm (b) as a function of the crystal length L. Optimization parameters are summarized in Table 3.4 on page 58.

several mirrors with different reflectivities are tested or a mirror with a lower reflectivity is used. The second option becomes clear from Fig. 3.5 where, in order to have a higher enhancement factor, the reflectivity should rather be chosen a little bit too low than too high. This is due to the milder slope and hence larger tolerance on the lower reflectivity side, especially in the case of low cavity losses.

From (3.5), (3.6) and (3.7), it can be clearly seen that P_ω^{cav} depends on A which in turn depends on P_ω^{cav}, thus forming a nonlinear set of equations. This set of equations was solved numerically using Matlab. After the initial estimation of all losses, an input mirror with $r = 0.975$ was ordered and a mirror with $r = 0.978$ was received.

Consequently, in the experiment, an input mirror with $r = 0.978$ was used and the tangential linearly polarized laser power in front of the mirror was measured to be 0.95 W. Besides this, for the simulations, $t \approx 1\%$, $c_{\mathrm{eff}} \approx 80\%$ was assumed and η to be the one plotted in Fig. 3.4b. Thus, the fundamental power inside the cavity is plotted in Fig. 3.6a for the same crystal length domain and it has a minimum corresponding roughly to the maximum of the conversion coefficient η (see Fig. 3.4b and Eq. (3.7)).

Finally, there is a trade-off between the conversion efficiency and the power built inside the cavity regarding the crystal length. By combining the plot from Fig. 3.4b with the one from Fig. 3.6a according to (3.3) we obtain the expected $P_{2\omega}$ shown in Fig. 3.6b. The first maximum is obtained at 20 mm and the expected power level is around 200 mW.

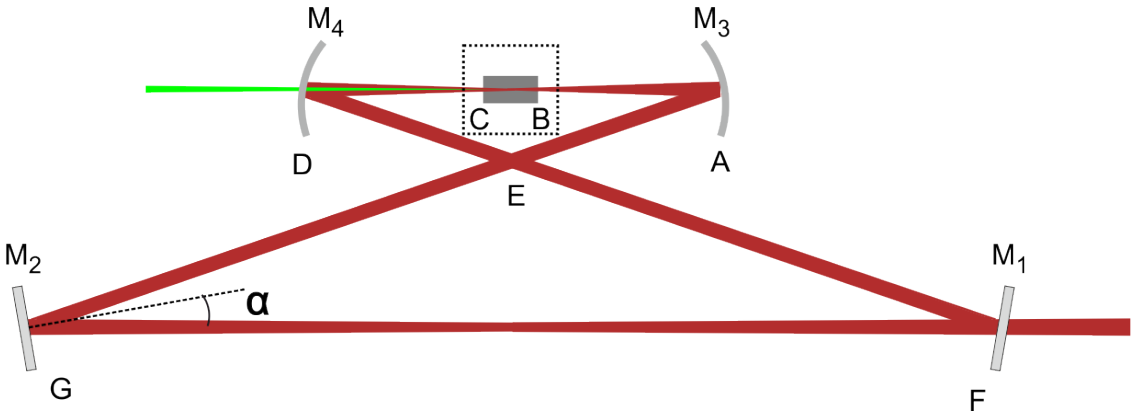

Figure 3.7: The bow-tie resonator for SHG at 1118 nm in a LBO crystal.

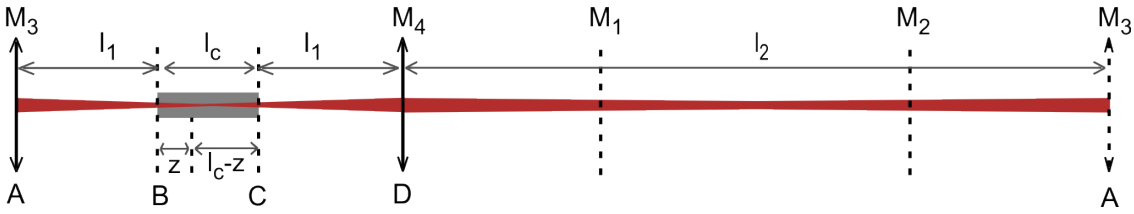

Figure 3.8: The unfolded bow-tie resonator for SHG at 1118 nm.

3.2.4 Ray Transfer Matrix Analysis of the First Resonator

The 20 mm long LBO nonlinear crystal was cut for non-critical phase-matching (NCPM), type I XY/XZ, $\theta = 90°$, $\phi = 0°$. Eq. (2.64) for the optimum $\xi = 2.84$ [61] is equivalent with obtaining a beam waist of 28 μm in the middle of the crystal. Using the ray transfer matrix analysis [78], a bow-tie resonator was designed that allows the oven with the crystal to be fitted in the middle of the short arm and to obtain the required beam waist in the center of the crystal, as depicted in Fig. 3.7. Because of the oven size, a rather large folding angle α has to be used.

In order to write the explicit form of the matrices and to calculate the waist along the beam inside the resonator, it is easier to unfold the bow-tie resonator as in Fig. 3.8 where M1 and M2 are the plane mirrors, M3 and M4 are the plano-concave mirrors, l_c is the crystal length, l_1 is the distance between the crystal face and the nearest focusing mirror and l_2 is the outer distance between the focusing mirrors. Since the plane mirrors have no effect on the beam shaping, they will not be considered in the calculation.

Because of the tilt of the spherical mirrors in one plane, the respective beam shaping is different for the two planes: the tangential(horizontal, parallel to the laser table in the

Table 3.2: Transfer matrices used for calculating the beam shape and size inside the first resonator according to Fig. 3.8.

Matrix label	Tangential(H)	Sagittal(V)
M_{AA}	$\begin{pmatrix} 1 & 0 \\ -\frac{1}{f\cos\alpha} & 1 \end{pmatrix}$	$\begin{pmatrix} 1 & 0 \\ -\frac{\cos\alpha}{f} & 1 \end{pmatrix}$
M_{AB}	$\begin{pmatrix} 1 & l_1 \\ 0 & 1 \end{pmatrix}$	$\begin{pmatrix} 1 & l_1 \\ 0 & 1 \end{pmatrix}$
M_{BC}	$\begin{pmatrix} 1 & \frac{l_c}{n_c} \\ 0 & 1 \end{pmatrix}$	$\begin{pmatrix} 1 & \frac{l_c}{n_c} \\ 0 & 1 \end{pmatrix}$
M_{CD}	$\begin{pmatrix} 1 & l_1 \\ 0 & 1 \end{pmatrix}$	$\begin{pmatrix} 1 & l_1 \\ 0 & 1 \end{pmatrix}$
M_{DD}	$\begin{pmatrix} 1 & 0 \\ -\frac{1}{f\cos\alpha} & 1 \end{pmatrix}$	$\begin{pmatrix} 1 & 0 \\ -\frac{\cos\alpha}{f} & 1 \end{pmatrix}$
M_{DA}	$\begin{pmatrix} 1 & l_2 \\ 0 & 1 \end{pmatrix}$	$\begin{pmatrix} 1 & l_2 \\ 0 & 1 \end{pmatrix}$

current setup) and the sagittal(vertical) one. The matrices for the two planes are given in Table 3.2, where α and f are the tilt angle and the focal length of the focusing mirror, respectively, while n_c is the refractive index of the crystal.

For numerical calculation of the beam waist inside the crystal for example, the corresponding matrix M_{BC} is splitted in two by introducing an intermediate point Z

$$M_{BZ} = \begin{pmatrix} 1 & \frac{z}{n_c} \\ 0 & 1 \end{pmatrix} \tag{3.8}$$

$$M_{ZC} = \begin{pmatrix} 1 & \frac{l_c - z}{n_c} \\ 0 & 1 \end{pmatrix} \tag{3.9}$$

where $l_c = l_z + (l_c - l_z)$.

The matrix of the overall system for the point Z is

$$M = \begin{pmatrix} A & B \\ C & D \end{pmatrix} = M_{BZ}M_{AB}M_{AA}M_{DA}M_{DD}M_{CD}M_{ZC}. \tag{3.10}$$

In the resulting matrix, B is depending on the intermediate-point position z and allows the calculation of the beam waist along the optical axis [79]

$$w^2(z) = -\frac{\lambda_0 B}{\pi\sqrt{1-\left(\frac{A+D}{2}\right)^2}}. \tag{3.11}$$

The well-known stability condition for a resonator is

$$\left|\frac{A+D}{2}\right| < 1. \tag{3.12}$$

As it can be easily seen in Table 3.2, for a given crystal length, there are three independent parameters which can be tuned in order to obtain the required beam waist in the middle of the crystal: the length of the long arm l_2, the tilt angle α and the focal length f of the focusing mirrors. For each set of values of these parameters, there is only a single value of the distance l_1 between the crystal face and the nearest mirror for which a round waist in the middle of the crystal is obtained. A beam waist of only 28 μm would require short focal length mirrors, typically less than 50 mm. Moreover, in order to prevent the appearance of astigmatism, the angle α should be less than 5°. Together, these two conditions would greatly obstruct the fitting of the oven. Nevertheless, it is possible to increase both parameters by accepting two compromises: a rather long cavity length and partial astigmatism.

The optimum result is presented in Fig. 3.9. The total length of the cavity is 1709 mm and has a full folding angle of 30°. For the focusing arm, two plano-concave mirrors with $f = 70$ mm in a distance of $d = 154$ mm were chosen. With these specifications, the optimal round waist of 28 μm is obtained in the middle of the crystal. As expected, the focus in the middle of the long arm is astigmatic because of the large folding angle required to fit the oven into the cavity.

3.2.5 Setup of the First Resonator

The design of the first resonator is shown in Fig. 3.10. The observed elliptical output polarization of the fiber laser was optimized and controlled with a combination of a $\lambda/4$ and a $\lambda/2$ waveplate in front of the Faraday rotator. The rotator is used as an optical

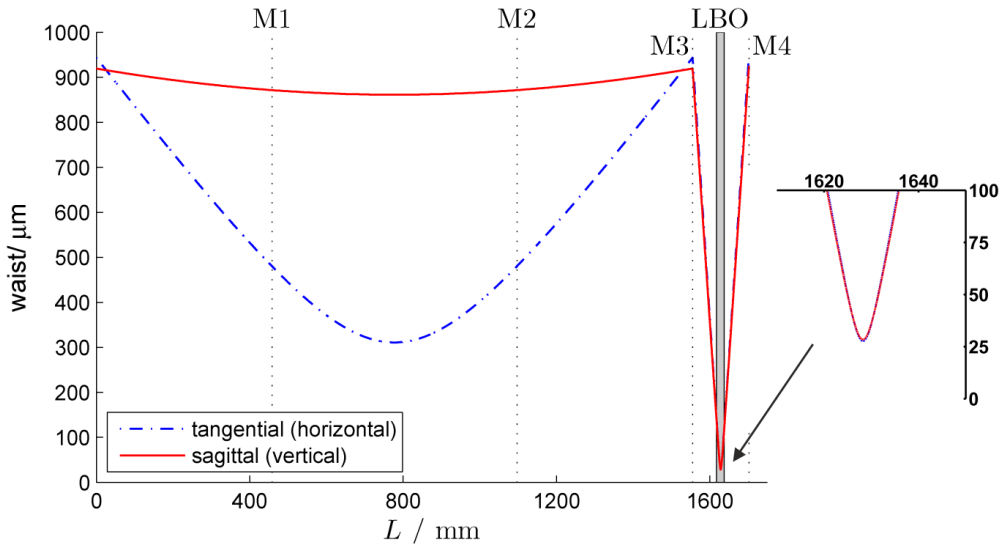

Figure 3.9: Beam waist size inside the cavity for the sagittal and tangential plane. The position of the folding mirrors M1-M4 and of the 20 mm long LBO crystal are indicated. An enlarged view of the focal region is shown on the right.

isolator to avoid back reflections into the laser. Mode matching to the astigmatic weak focus in the long arm is performed with two convex lenses ($f_1 = f_2 = 20$ cm, distance between the output of the laser and the first lens $d_1 \approx 35$ cm, distance between the lenses $d_{12} \approx 51$ cm and distance between the second lens and the middle of the long arm $d_2 \approx 35$ cm) and an anamorphic prism pair with 3:1 ratio (APP).

A neutral density filter (NF), an extra $\lambda/4$ waveplate and a Glan-Laser polarization beam-splitter were used for the polarization analysis required by the locking scheme. An additional long pass filter (LPF) with cut-on at 1100 nm was used to filter out the unpolarized ASE from the fiber laser centered at 1064 nm which was reflected by the cavity. The reflected ASE was falling on both photodiodes and was affecting the quality of the error signal and thus the stability of the cavity locking.

The input mirror M1 is AR coated for 1118 nm on the outer surface and has a reflectivity of 97.8% at 1118 nm on the surface inside the cavity. M2 is highly reflective (>99.9%) for the fundamental and is mounted on a piezo mirror shifter for fine adjustments of the cavity length. M3 is highly reflective (>99.9%) for 1118 nm while the output coupler M4 is highly reflective (>99.8%) for 1118 and has a high transmission (T >94%) for the second harmonic radiation at 559 nm.

With the aid of the anamorphic prism pair (APP) and by tilting one of the the

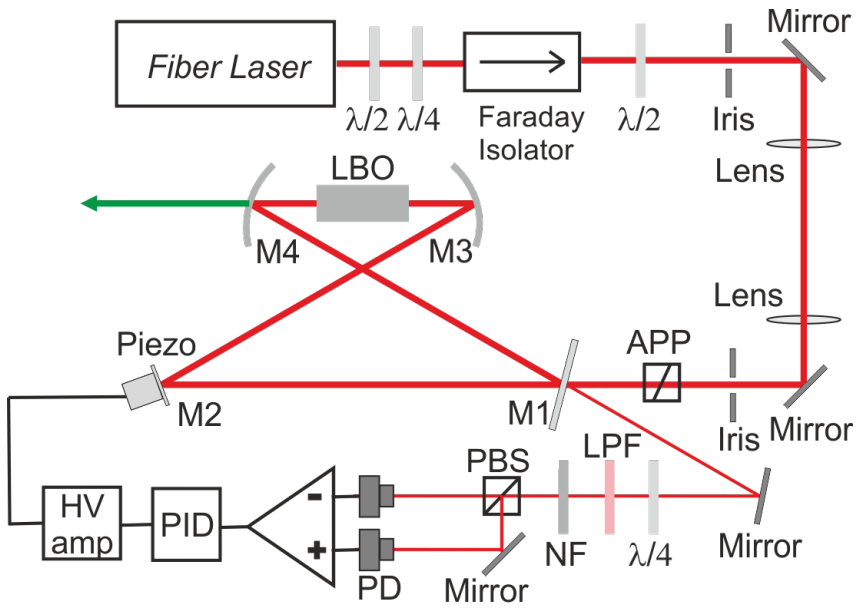

Figure 3.10: Setup of the laser and the first SHG cavity including the Hänsch-Couillaud locking setup ($\lambda/4$ and $\lambda/2$: quarter- and half-wave plate respectively, APP: anamorphic prism pair, M1-M4: cavity mirrors, LPF: low pass filter, NF: neutral density filter, PBS: polarizing beam splitter, PD: photodiode, PID: proportional-integral-derivative controller, HV amp: high voltage amplifier).

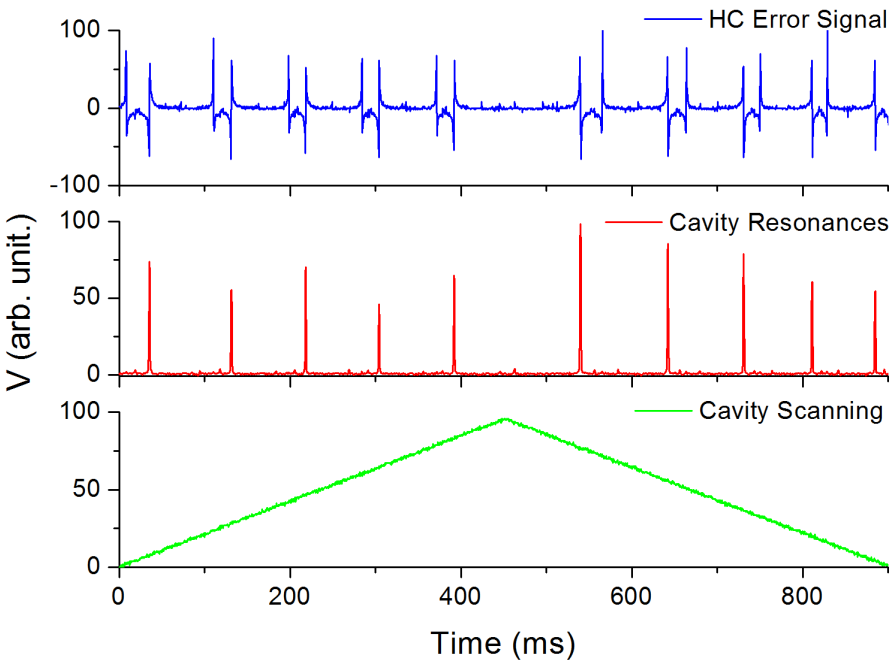

Figure 3.11: The typical resonances as seen at the output of the cavity and the Hänsch-Couillaud error signal during the scanning of the piezo mirror shifter.

two convex lenses, it was possible to properly mode-match the laser to the cavity and thus to dramatically increase c_{eff} from below 50%. Up to 80% coupling efficiency of the fundamental beam into the cavity was obtained for intermediate input power levels($\approx$ 0.3 W). At the maximum 0.95 W of infrared power in front of the cavity, due to higher conversion losses, the coupling efficiency dropped to 75%, a sign that the reflectivity of the input mirror $r = 0.978$ is slightly higher than optimum for this power level.

The cavity is locked to the laser frequency using the standard Hänsch-Couillaud polarization analysis locking scheme [65] as described in Section 2.6. The typical resonances as seen at the output of the cavity and the Hänsch-Couillaud error signal during the scanning of the piezo mirror shifter are shown in Fig. 3.11. The double error signal with opposite phase over each free spectral range appears because LBO is a biaxial birefringent crystal [80].

The enhancement factor was between 40 and 60, depending on the pump power. Two LBO crystals from Castech were tested in this cavity. Although they had identical specifications, they were from different production charges because the second crystal was bought one year later. At maximum power, the maximum green output was approximately 230 mW for the first crystal and 320 mW for the second crystal with 950 mW infrared power in front of the resonator, which is for both crystals even better than expected from the simulations. Probably, this is an effect of the crystal quality, which plays a very important role in the SHG efficiency. The specifications used for the simulations were that of a standard LBO crystal while the ordered crystals were actually of higher quality - specified as "low impurities" - but without any quantitative specifications.

Besides the good output values for both crystals, there is a large difference between the outputs of the two crystals. This can be caused by a difference in the quality of each sample but it rather seems that after a few months the crystal surfaces may have become dirty and thus it affected the SHG efficiency. A precise answer is not possible because the optimization for the first crystal took a few months while for the second crystal it took only a few days. A possible way to protect the crystal surfaces is to seal the doubling cavity and to use a continuous flow of dry nitrogen to purge the contaminants.

The achieved overall SHG efficiency was $\approx$33% relative to the 0.95 W fundamental laser power in front of the cavity and $\approx$42% relative to the power coupled in. The green power was measured after an additional dichroic mirror in order to remove the leaking fundamental, which can be comparable with the second harmonic in terms of power. The

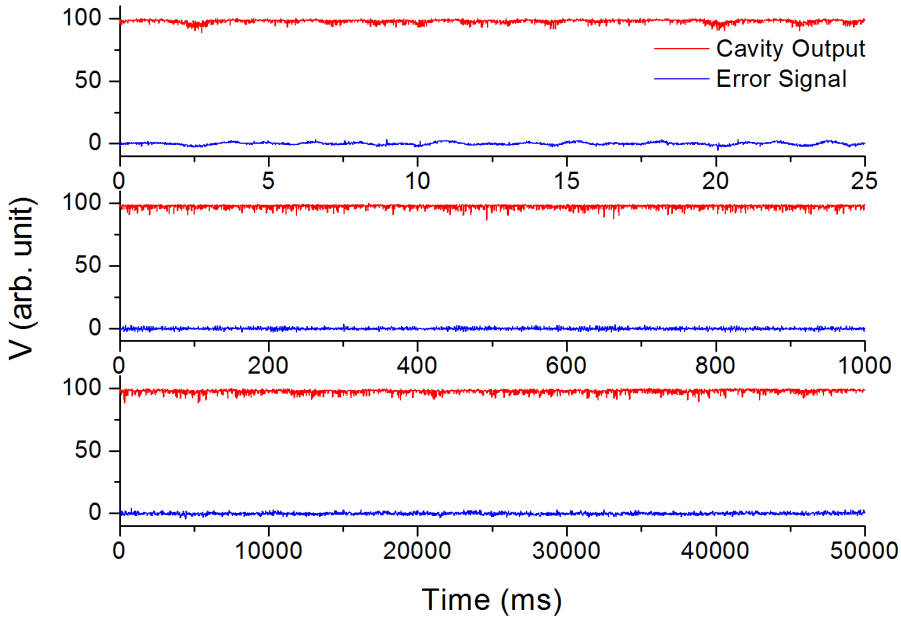

Figure 3.12: The output of the cavity and the error signal with the Hänsch-Couillaud stabilization active for three time scales.

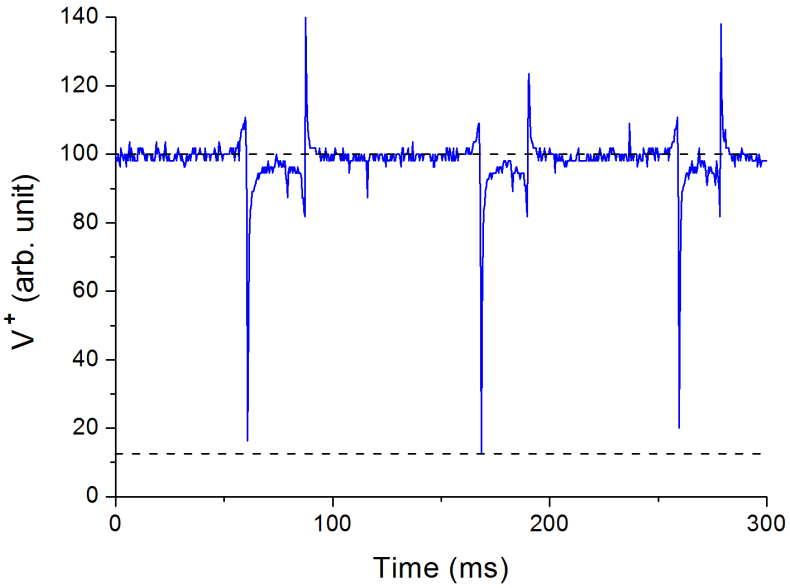

Figure 3.13: The coupling efficiency of the IR laser beam to the cavity measured through the signal from the non-inverting input of the differential photoamplifier.

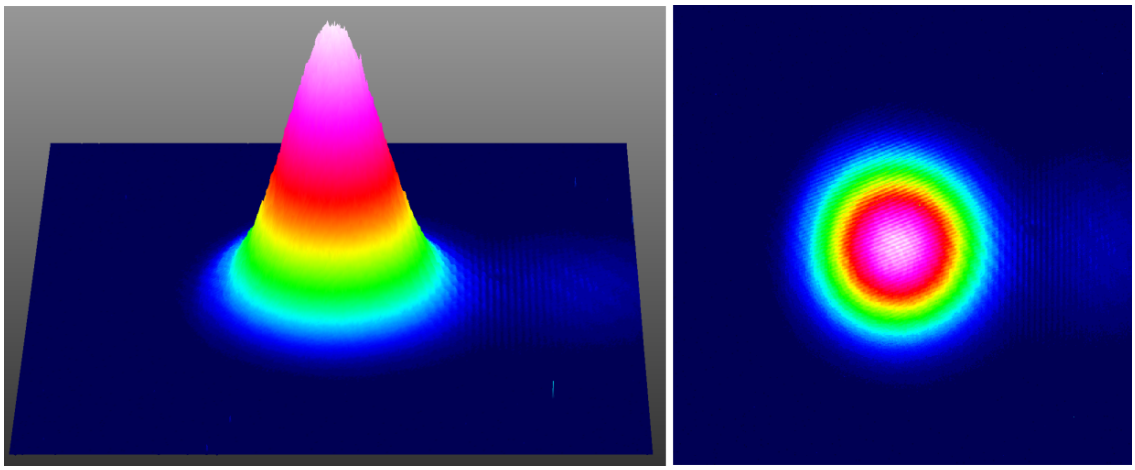

Figure 3.14: The 559 nm beam profile as acquired with a CCD Camera.

cavity was placed in a PVC case with an insulation of Thorlabs sorbothane sheets for better stability.

The stability was further improved with the expense of a small decrease in doubling efficiency by resizing the cavity to a smaller roundtrip, corresponding to a non-optimal round waist of 35 μm in the middle of the crystal. The output of the cavity and the error signal with the Hänsch-Couillaud stabilization active for three time scales are illustrated in Fig. 3.12.

The total length of the cavity was reduced to 1158 mm, the distance between the focusing mirrors was adjusted to 157.5 mm, while the full folding angle was increased to 38°. Consequently, the astigmatism in the long arm was exacerbated to a beam waist of approximatively 240 μm in the tangential (horizontal, parallel to the laser table) plane and 720 μm in the sagittal plane. However, this was closer to the 3:1 ratio of the APP and the mode-matching was performed only with one additional convex lens ($f_1 = 30$ cm, distance between the output of the laser and the lens $d_1 \approx 65$ cm, distance between the lens and the middle of the long arm $d_2 \approx 40$ cm), improving the coupling efficiency to more than 85%. The coupling efficiency was measured by blocking the photodiode corresponding to the inverting input of the differential amplifier for the error signal. At resonance, in an ideal case with 100% coupling efficiency, the intensity of the light falling on the non-inverting photodiode should drop to zero. The measured signal from the non-inverting input is shown in Fig. 3.13.

The resonator was stable for a full working day during the measurements. The beam profile was acquired with a CCD Camera at a low power level and is illustrated in Fig. 3.14.

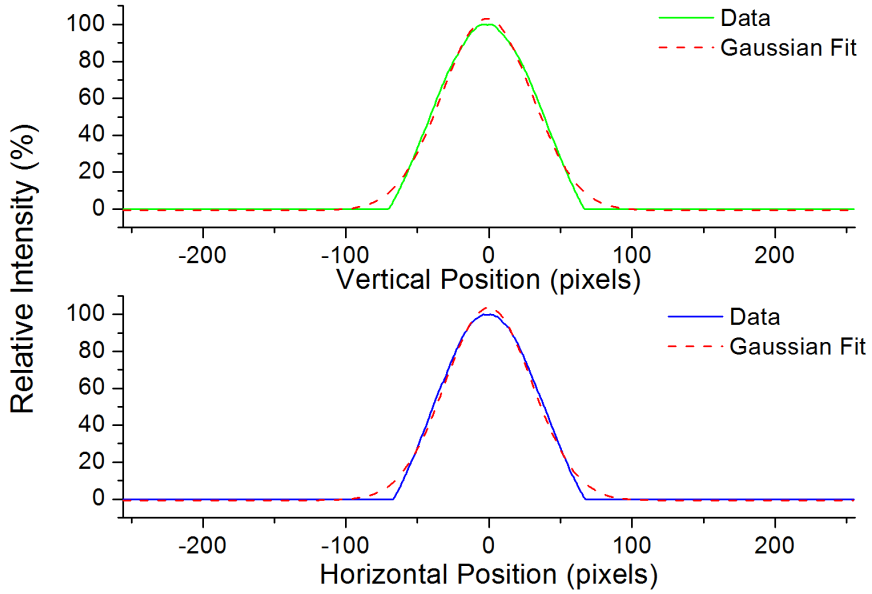

Figure 3.15: The transversal intensity profile of the 559 nm beam along the horizontal and the vertical axis, together with a Gaussian fit.

The intensity profile along the horizontal (parallel to the laser table) and the vertical axis, together with a Gaussian fit, is shown in Fig. 3.15. The output beam is a nice Gaussian TEM_{00} mode, which is crucial for the next frequency doubling step.

3.3 Design of the Second Resonator

For doubling at 559 nm there is no common commercial nonlinear crystal capable of NCPM. Therefore, crystals for critical phase-matching (CPM) at this wavelength and with a transparency range down to at least 279 nm were checked. The potential candidates were LBO, potassium dihydrogen phosphate (KDP) and β-barium borate (BBO). KDP has a very good optical quality and was previously used for doubling at 559 nm [77] but an efficient SHG requires very long crystals due to its relatively small nonlinear coefficient. While LBO and BBO have comparable optical quality, BBO has an approximately twice as large nonlinear coefficient compared to LBO and was frequently used for very efficient SHG around 559 nm [66, 75, 81, 82]. Moreover, the bigger nonlinear coefficient allows the usage of shorter crystals and the improvement of the enhancement factor of a ring cavity by reducing the linear losses inside the crystal, thus making BBO the optimal choice.

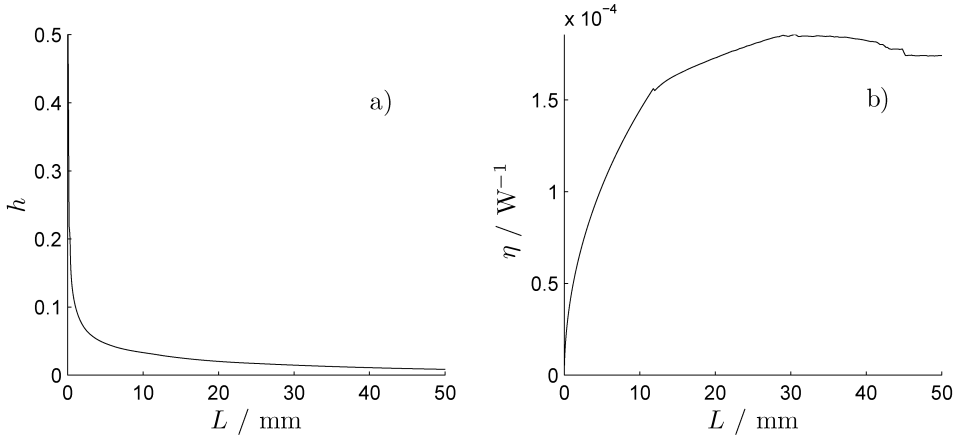

Figure 3.16: The function of optimizable parameters $h(L)$ (a) from Eq. (2.68) and the conversion coefficient η (b) for SHG in BBO at 559 nm as a function of the crystal length L.

3.3.1 Crystal Length and the Cavity Enhancement

Compared to NCPM, for CPM the walk-off angle is non-zero. Specifically for our case, $\rho \approx 4.8°$, $\beta \neq 0$ and the corresponding value of the optimum focusing parameter is $\xi = 1.39$ [61]. As for the refractive index of BBO, the typical fluctuation is $\delta n_L \approx 10^{-6}$ cm^{-1} due to inhomogeneities and $\delta n_T \approx 7.3 \cdot 10^{-6}$ K^{-1} due to temperature fluctuation which is, like in the case of first SHG cavity, 0.1 K at maximum for our case. The typical absorption coefficients are $\alpha_1 \approx 0.3\%$ cm^{-1} and $\alpha_2 \approx 4\%$ cm^{-1}.

Again, using these parameters and Matlab for numerically solving the double integral in (2.68), $h(L)$ is plotted in Fig. 3.16a over a crystal length region ranging from 0 to 50 mm. The resulting conversion coefficient is plotted in Fig. 3.16b and it reaches 80% of its maximum already for a crystal length of 10 mm. Compared to LBO, the conversion coefficient of BBO doesn't have a prominent maximum, but rather a plateau. This makes any intention to use longer crystals in order to increase the efficiency useless, even in the case of single-pass SHG.

For simulating the behavior of the BBO crystal inside the cavity, an input mirror with $r = 0.99$ and a power level of 200 mW for the horizontal linearly polarized green laser in front of the cavity were considered. After the initial simulations, it appeared that it is more favorable to use a crystal with Brewster-cut surfaces than with AR coated surfaces because of the much smaller reflectivity of the first type. It was assumed that the surface losses $t \approx 0.75\%$ for Eq. (3.7) and $c_{\text{eff}} \approx 80\%$.

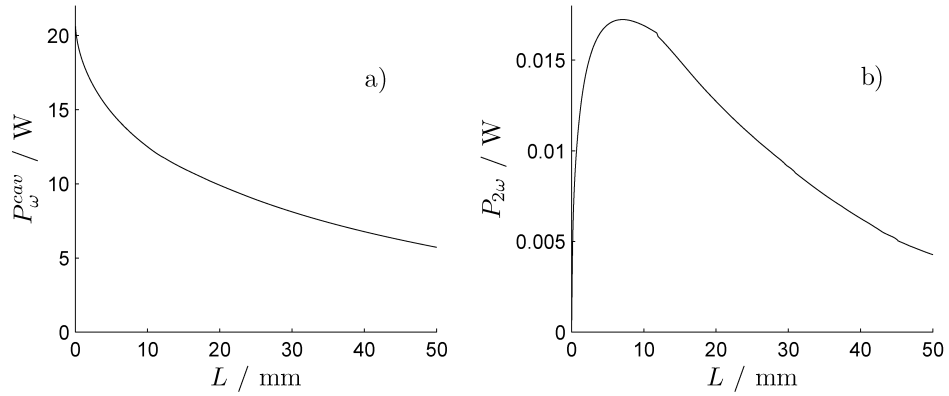

Figure 3.17: The power level of the 559 nm fundamental inside the cavity (a) and the expected power level of the second harmonic 279 nm (b) outside the cavity as a function of the crystal length L. Optimization parameters are summarized in Table 3.4 on page 58.

The power level of the fundamental light inside the cavity is plotted in Fig. 3.17a. Using (3.3) and the simulated data, the expected power level of the generated second harmonic at 279 nm outside the cavity is shown in Fig. 3.17b. It was estimated that from the UV radiation generated inside the crystal, only 75% can be used outside the cavity. The losses are mainly at the output surface of the Brewster-cut crystal for 559 nm - about 22% according to the Fresnel equations since the harmonic is a tangential/p-polarised wave - but also at the inner surface of the output dichroic mirror. The first maximum is obtained at 7 mm and has an expected power level of about 17 mW.

3.3.2 Ray Transfer Matrix Analysis of the Second Resonator

A 7.4 mm long[1] Brewster-cut BBO-crystal was used for type I CPM at 559 nm with $\theta = 44.45°$, $\phi = 0°$ crystal cut. From Eq. (2.64), the corresponding beam waist in the middle of the crystal for the optimum $\xi = 1.39$ [61] is approximately 16 μm. Again, using the ray transfer matrix analysis, a bow-tie resonator was designed, which allows us to obtain the required beam in the middle of the crystal, as shown in Fig. 3.18.

By using a Brewster-cut for the BBO-crystal, two new matrices for the horizontal(sagittal) plane are introduced, characterizing the refraction at the crystal surface. In the unfolded resonator (Fig. 3.19), M5 and M6 are the plane mirrors, M7 and M8 are

[1] a 7 mm long crystal was ordered but a 7.4 mm crystal was received, in compliance with the specified tolerance.

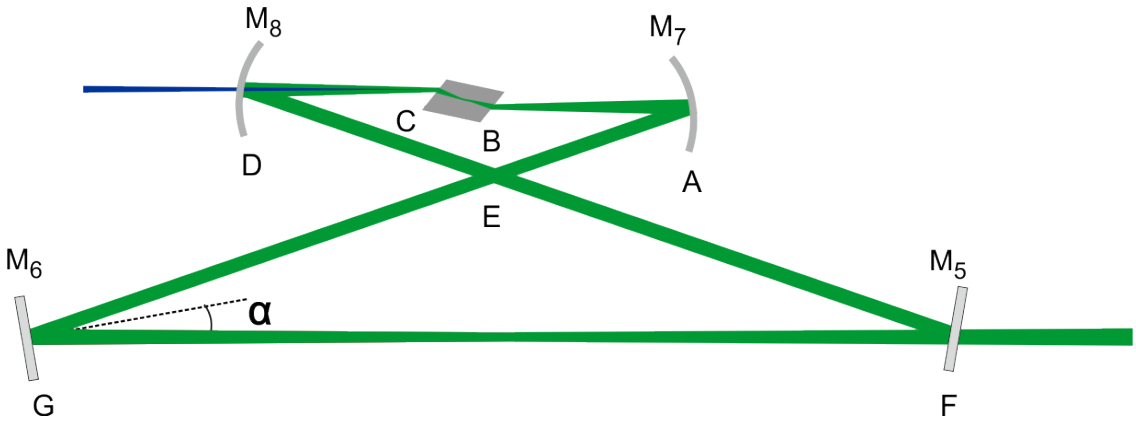

Figure 3.18: The bow-tie resonator for SHG at 559 nm in a BBO crystal.

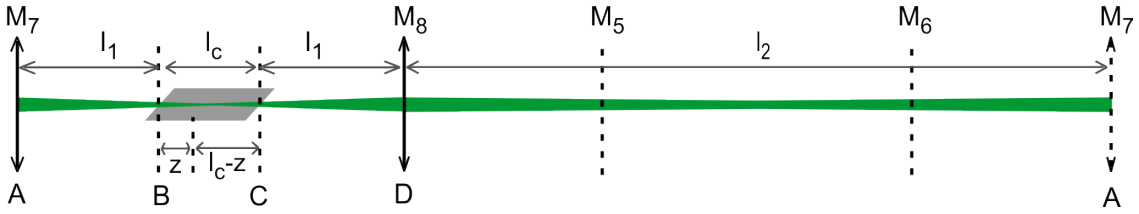

Figure 3.19: The unfolded bow-tie resonator for SHG at 559 nm.

the plano-concave mirrors, l_c the crystal length, l_1 is the distance between the crystal face and the nearest spherical mirror and l_2 is the outer distance between the focusing mirrors. The complete set of matrices is given in Table 3.3 where α and f are the tilt and the focal length of the focusing mirrors while n_c is the refractive index of the crystal.

Using the same procedure as for the first resonator, the beam waist inside the resonator is plotted in Fig. 3.20. Because of the astigmatism introduced by the concave spherical mirrors, crystal faces and crystal axis, it is impossible to design a simple cavity which facilitates the focusing of the laser to a round waist inside the crystal. Therefore, a bow-tie resonator capable of achieving a focus in the middle of the crystal with a waist of 16 μm in the tangential (vertical) plane and 26 μm in the sagittal (horizontal, parallel to the laser table) plane, was designed.

3.3.3 Setup of the Second Resonator

The full setup is presented in Fig. 3.21. The round Gaussian beam from the first resonator is mode-matched into the second resonator with two spherical lenses ($f_1 = 15$ cm, $f_2 = 10$ cm, distance between the output of the first resonator and the first lens $d_1 \approx 17$ cm,

Table 3.3: Transfer matrices used for calculating the beam shape and size inside the second resonator according to Fig. 3.19.

Matrix label	**Sagittal(H)**	**Tangential(V)**
M_{AA}	$\begin{pmatrix} 1 & 0 \\ -\frac{1}{f\cos\alpha} & 1 \end{pmatrix}$	$\begin{pmatrix} 1 & 0 \\ -\frac{\cos\alpha}{f} & 1 \end{pmatrix}$
M_{AB}	$\begin{pmatrix} 1 & l_1 \\ 0 & 1 \end{pmatrix}$	$\begin{pmatrix} 1 & l_1 \\ 0 & 1 \end{pmatrix}$
M_{BB}	$\begin{pmatrix} n_c & 0 \\ 1 & \frac{1}{n_c} \end{pmatrix}$	
M_{BC}	$\begin{pmatrix} 1 & \frac{l_c}{n_c} \\ 0 & 1 \end{pmatrix}$	$\begin{pmatrix} 1 & \frac{l_c}{n_c} \\ 0 & 1 \end{pmatrix}$
M_{CC}	$\begin{pmatrix} \frac{1}{n_c} & 0 \\ 1 & n_c \end{pmatrix}$	
M_{CD}	$\begin{pmatrix} 1 & l_1 \\ 0 & 1 \end{pmatrix}$	$\begin{pmatrix} 1 & l_1 \\ 0 & 1 \end{pmatrix}$
M_{DD}	$\begin{pmatrix} 1 & 0 \\ -\frac{1}{f\cos\alpha} & 1 \end{pmatrix}$	$\begin{pmatrix} 1 & 0 \\ -\frac{\cos\alpha}{f} & 1 \end{pmatrix}$
M_{DA}	$\begin{pmatrix} 1 & l_2 \\ 0 & 1 \end{pmatrix}$	$\begin{pmatrix} 1 & l_2 \\ 0 & 1 \end{pmatrix}$

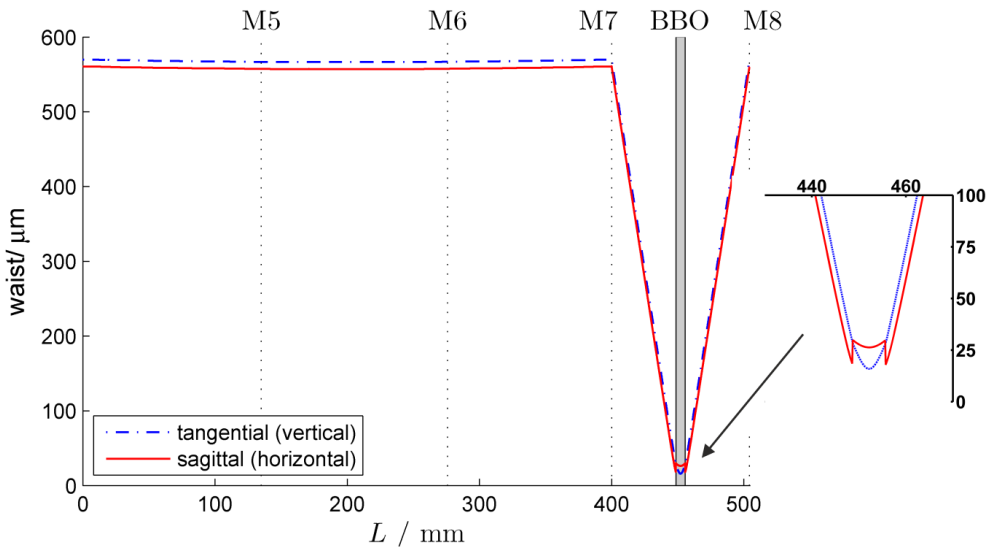

Figure 3.20: Beam waist size inside the second cavity. An enlarged view of the focal region is shown to the right.

distance between the lenses $d_{12} \approx 55$ cm and distance between the second lens and the middle of the long arm $d_2 \approx 33$ cm). Instead of an LPF, a dichroic mirror is used here to remove the leaking infrared beam in order to optimize the error signal for the Hänsch-Couillaid [65] locking. The initial M5 was AR coated for 559 nm on the outside relative to the cavity and it had a reflectivity of 99.3% on the inside, which was slightly higher than the optimum and resulted in locking problems during first tests, as observed in [83]. The mirror was consequently replaced by one with a 98.2% reflectivity.

The other cavity mirrors have a high reflectivity (>99.9%) for 559 nm and a high transmission (>90%) for 279 nm on the surfaces that form the resonator. On the outer surface they are AR coated for 279 nm, even though that is necessary only for M8. M6 is mounted on a piezo tube for fast correction to the cavity length, as required by the locking scheme. M7 is a plano-concave mirror while M8 is a concave-convex zero-lens shaped mirror, both with a focal length of 50 mm. The distance between the focusing mirrors and the nearest crystal face is 48.7 mm, the full folding angle is 18.8° and the total length of the cavity is 504 mm. The crystal is kept at 50°C to avoid condensation of water vapor on its surface. The typical resonances as seen at the output of the cavity and the Hänsch-Couillaud error signal during the scanning of the piezo mirror are shown in Fig. 3.22.

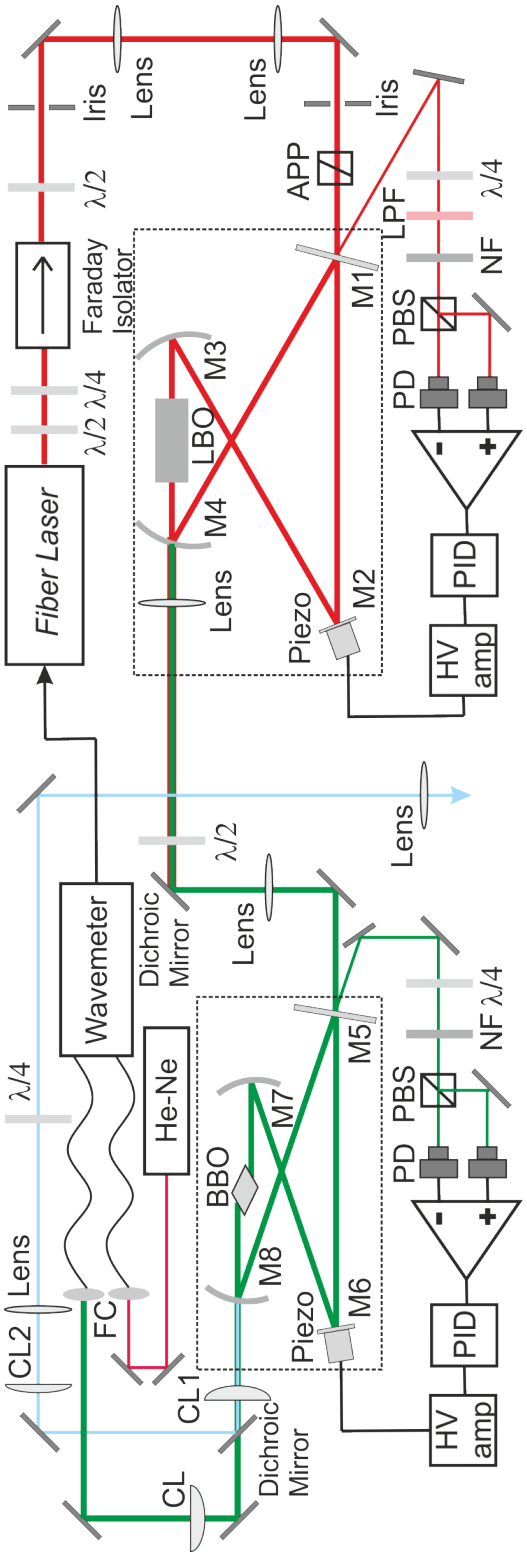

Figure 3.21: The UV laser system at 279 nm. Some abbreviations are the same as in Fig. 3.10 (M5-M8: cavity mirrors, CL: cylindrical lens, FC: fiber coupler).

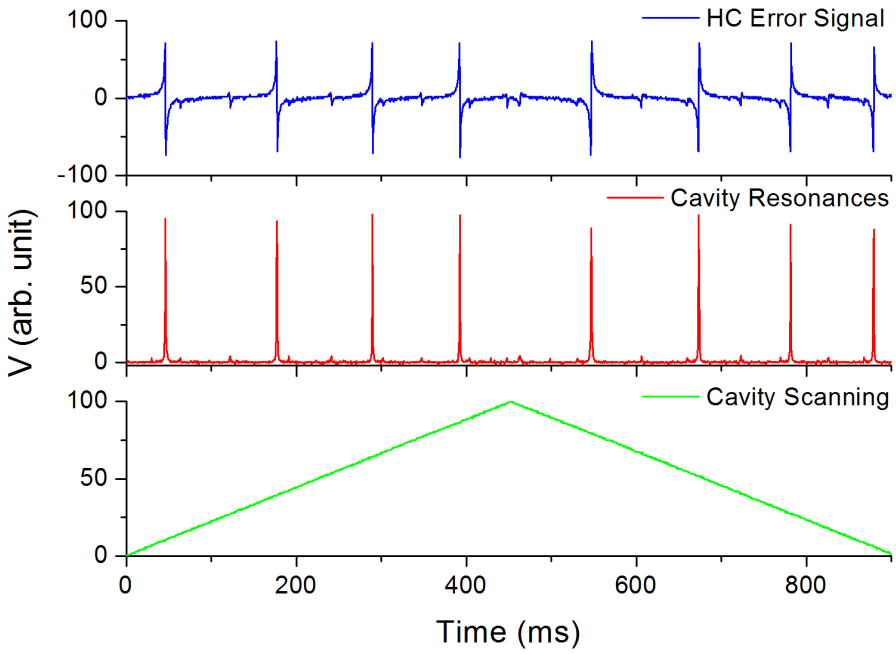

Figure 3.22: The typical resonances as seen at the output of the second cavity and the Hänsch-Couillaud error signal during the scanning of the piezo mirror.

As described in Subsection 3.2.5, the coupling efficiency was measured from the non-inverting input and is shown in Fig. 3.23. The measured coupling efficiency was $> 85\%$ and the enhancement factor was between 60 and 70 depending on the pump power. The maximum UV output power was 16.7 mW for 210 mW of green power in front of the resonator, which is in very good agreement with the simulations. Unlike for the first resonator, the BBO crystal used in the second resonator was a standard one. The maximum overall SHG efficiency was $\approx 8\%$ relative to the power in front of the cavity and $\approx 9\%$ relative to the power coupled in. The power was measured after an additional dichroic mirror which separates the UV beam from the leaking green beam.

Considering the actual scaling of the SHG efficiency with the pump power (3.3), this resonator seems to be of similar efficiency compared to the first resonator, despite the slightly lower optical quality of BBO and the less efficient solution for the phase matching - CPM over NCPM. This is partially due to the better quality of the cavity mirrors and higher nonlinear coefficient of the BBO compared to LBO. Moreover, the scaling of the SHG efficiency with the pump power for a resonator is not really linear since the enhancement factor of the cavity decreases when the single pass SHG conversion losses are higher, i.e. when the pump power is higher.

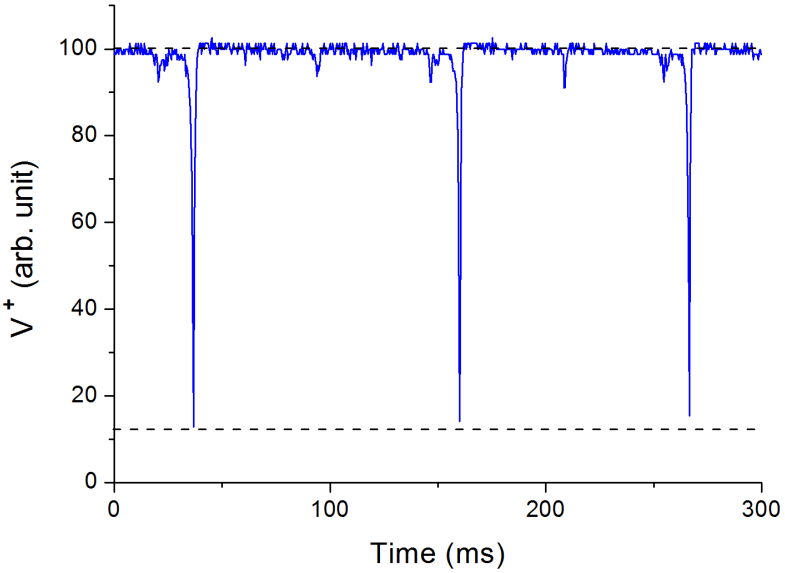

Figure 3.23: The coupling efficiency of the 559 laser beam to the second cavity measured through the signal from the non-inverting input of the differential photoamplifier.

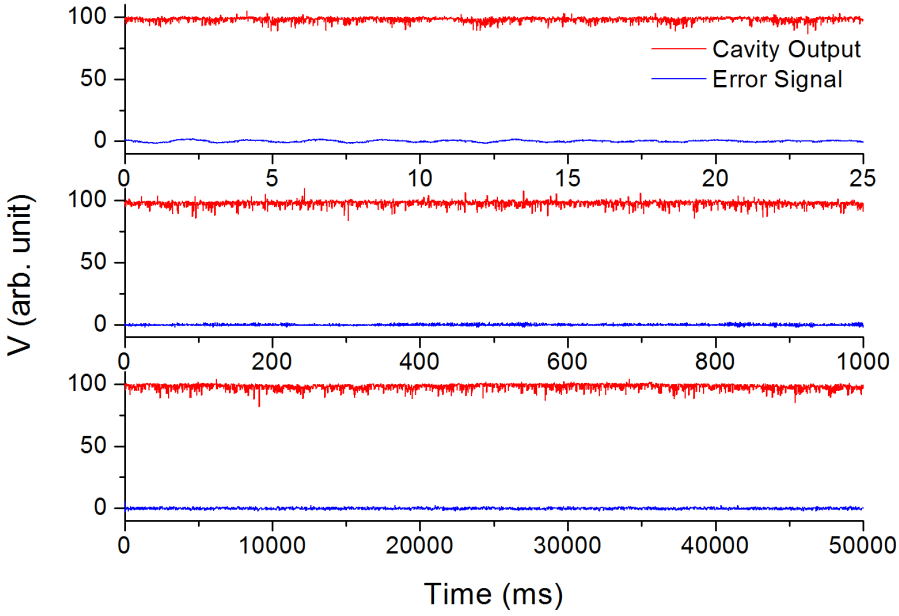

Figure 3.24: The output of the second cavity and the error signal with the Hänsch-Couillaud stabilization active for three time scales.

The resonator was placed in a PVC case for thermal and acoustic insulation and was stable for a full working day during the measurements. The output of the second cavity and the error signal with the Hänsch-Couillaud stabilization active for three time scales are illustrated in Fig. 3.24. A photo of the laser system with the second resonator enhanced is provided in Fig. 3.25.

The strongly elliptical output beam was reshaped to a roughly circular shape of 1 mm diameter with two cylindrical lenses (CL1 and CL2, $f_1 = 15$ cm, $f_2 = 20$ cm, distance between the output of the first resonator and the first cylindrical lens $d_1 \approx 14$ cm and distance between the cylindrical lenses $d_{12} \approx 65$ cm) and with two spherical lenses ($f_1 = 30$ cm, $f_2 = 75$ cm, distance between the second cylindrical lens CL2 and the first spherical lens $d_{23} \approx$11 cm and distance between the spherical lenses $d_{34} \approx 112$ cm). Because of the problems with the fiber laser, the available pump power in front of the first resonator was restricted to a maximum of 0.5 W. Even with such a relatively low input power, 3 mW of UV light are available for the experiment, which is sufficient for laser cooling. The most important details of the two resonators are summarized in Table 3.4.

Table 3.4: Summary of the most relevant parameters of the two resonators.

Parameter	1^{st} **Resonator Value**	2^{nd} **Resonator Value**
Crystal type	LBO	BBO
Phase matching	NCPM Type I	CPM Type I
Crystal length l_c	20 mm	7.4 mm
Input wavelength λ_0	1118.54 nm	559.27 nm
Crystal cut θ	90°	44.4°
Crystal cut ϕ	0°	0°
Optimum beam waist w_0	28 μm	16 μm
Experimental beam waist (T/S)[1]	35/35 μm	16/26 μm
Crystal input/output surfaces	Dual AR coating	Brewster-cut (59.1°)
Crystal temperature	96°C	50°C
Reflectivity of the input mirror	97.8%	98.2%
Total cavity length	1158 mm	504 mm
Full folding angle 2α	38°	18.8°
Focusing mirrors f	70 mm	50 mm
Focusing arm length[2] d	157.5 mm	104.8
Mode-matching beam waist (T/S)	240/720 μm	560/560 μm
Enhancement factor $A^{(\max)}$	≈60	≈70
Coupling efficiency $c_{\text{eff}}^{(\max)}$	>85%	>85%
Input fundamental power $P_{\omega}^{(\max)}$	950 mW	210 mW
Output harmonic power $P_{2\omega}^{(\max)}$	320 mW	16.7 mW
Doubling efficiency $P_{2\omega}^{(\max)}/P_{\omega}^{(\max)}$	≈33%	≈8%

[1]tangential/sagittal: The horizontal plane, parallel to the laser table, is tangential for the first resonator and sagittal for the second resonator;

[2]geometric length along the beam path.

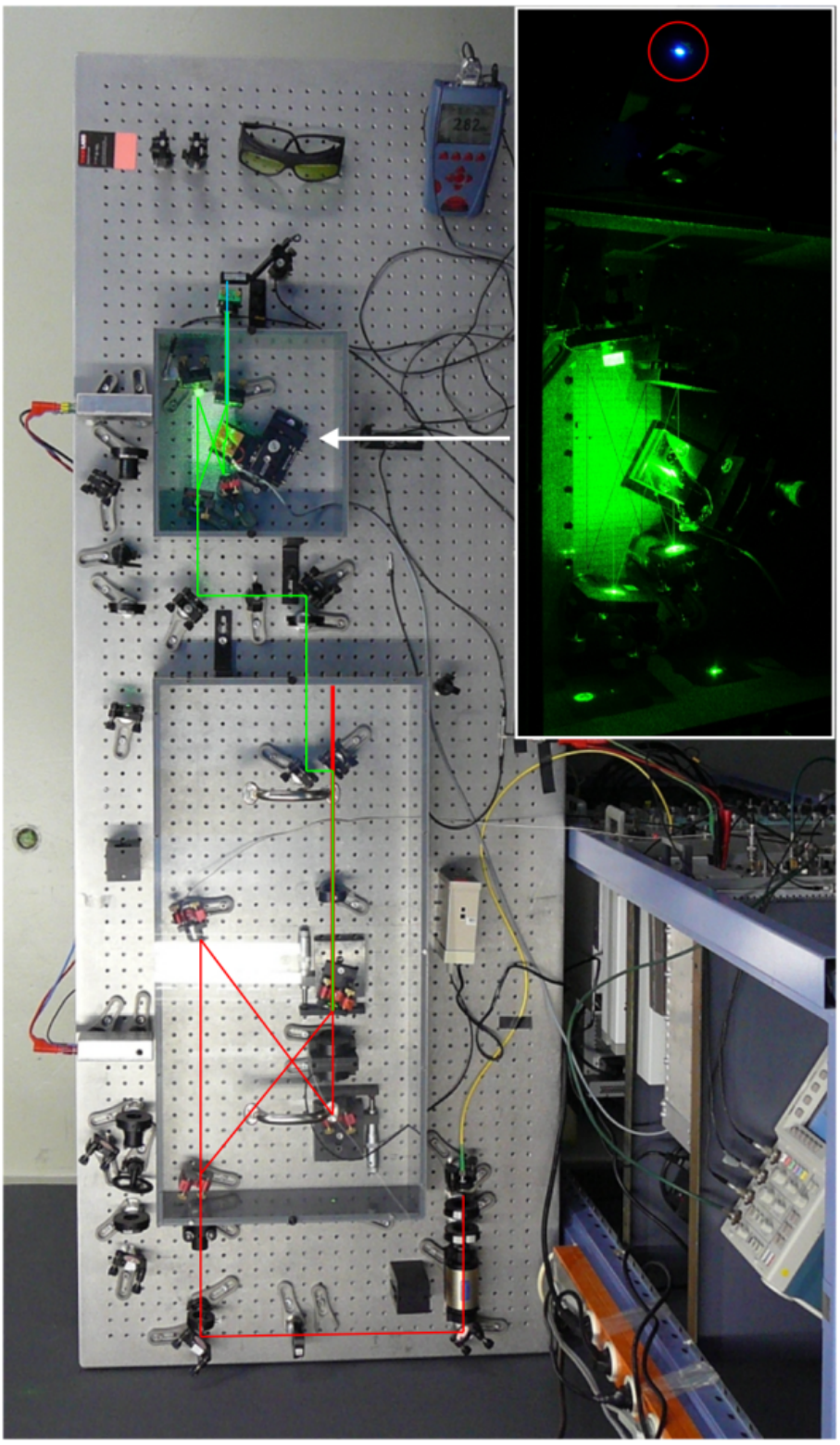

Figure 3.25: A photo of the UV laser system at 279 nm with the second resonator enhanced.

3.4 Frequency Stabilization and Control

The frequency of the fiber laser system can be controlled using a 0-200 V input that is applied to the piezo that stretches the fiber of the seed laser. The tuning range of this oscillator is 19 pm at the fundamental wavelength corresponding to approximatively 45 GHz for the fundamental or 190 GHz for the quadrupled laser beam. This is equivalent to 1 MHz/mV in UV and therefore requires a low-noise signal for the stabilization.

When considering a reference for locking, one should take into account the precision required for the experiment. Fortunately, for laser cooling of $^{24}Mg^{+}$, the requirements are moderate: The natural linewidth is $\delta\nu_{\text{nat}} = 42$ MHz [84] and the final temperature is below 1 K, which is equivalent to a Doppler width $\delta\nu_D = 157$ MHz.

For stabilization and control of this laser system, a High Finesse WS7 Super-Precision Wavelength Meter was used. The wavemeter has a calibration period of 14 days and was recalibrated regularly with a Sios SL02/1 Stabilized He-Ne laser. It has a PC-based graphical user interface, which allows to control the wavemeter through an USB 2.0 connection. The USB connection also acts as a power supply.

The software can be used to display the wavelength and offers also the possibility of custom function generation for frequency tuning. The software offers a very comfortable locking solution based on a digital PID regulator, which is part of the control software, and a -4..+4 Volts output correction signal with down to less than 2 MHz experimental locking stability in optimal conditions, despite the specified measurement resolution[1]. The main specifications for the wavemeter and for the stabilized He-Ne laser are listed in Table 3.5 and 3.6.

The laser system was locked using the leaking green beam from the second cavity, as presented in Fig. 3.21. Before connecting to the fiber laser, an offset was added to the correction signal - since the piezo can only be operated with positive voltage - and then amplified with a low-noise HV amplifier, thus being bounded in the 40 to 80 Volts range. Considering the piezo tuning range for the fiber laser, the effective slope available for the stabilization was ≈2.5 GHz/V for the green beam at 559 nm.

A typical wavelength course of the locked laser is presented in Fig. 3.26a. Even though locking to the wavemeter has been shown to be in principle capable to stabilize a laser within ±0.5 MHz of the set point [85], the frequency of the fiber laser's second harmonic was oscillating within ±15 MHz. For short periods, the laser was indeed locked within

[1] the stability was even measured with a frequency comb to be on the 0.5 MHz range for a few minutes.

Table 3.5: Technical specifications of the High Finesse WS7 Wavelength Meter.

Wavemeter Parameter	Value	Unit
Absolute accuracy 370 - 1100 nm	60	MHz
Measurement resolution	10	MHz
Data acquisition speed	400	Hz
Wavelength calculation speed	150	Hz
Pattern display speed	50	Hz
Required input power	0.01-10	μW
Fizeau interferometers FSR - fine mode	4	GHz
Fizeau interferometers FSR - wide mode	20-30	GHz

Table 3.6: Technical specifications of the Sios SL02/1 Stabilized He-Ne laser.

He-Ne Laser Parameter	Value	Unit
Nominal wavelength	632.9914 $\pm$ 0.0003	nm
Output power	$\geq$ 1	mW
Warm-up time to achieve stable operation	<10	min
Max. thermal frequency drift	$\pm$4	MHz/K
Max. total frequency drift	$\pm$25	MHz
Frequency stability over 1 hour	$\pm 1 \cdot 10^{-8}$	

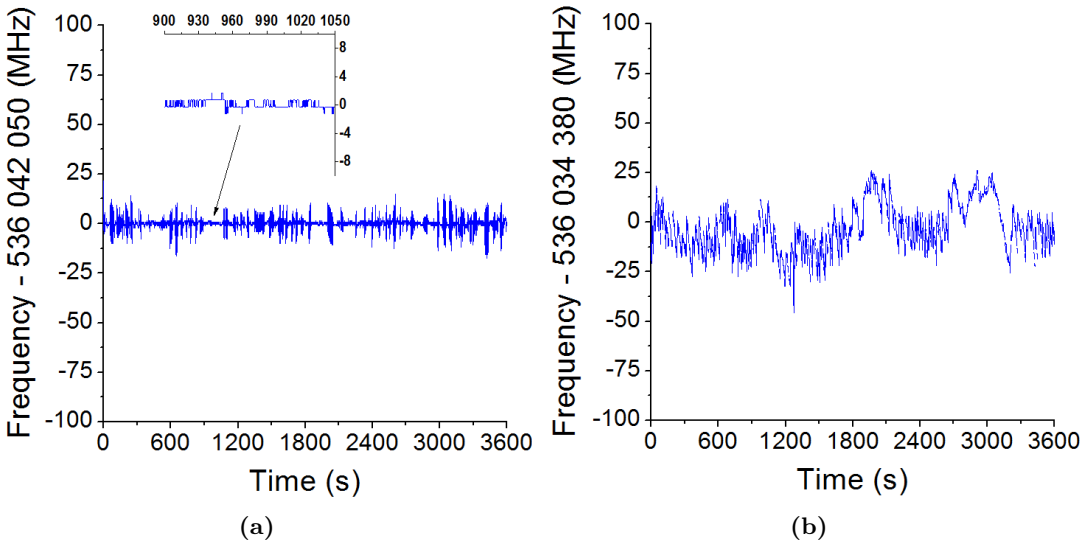

Figure 3.26: A locking example of the laser system to the wavemeter (a) and a free-running example (b).

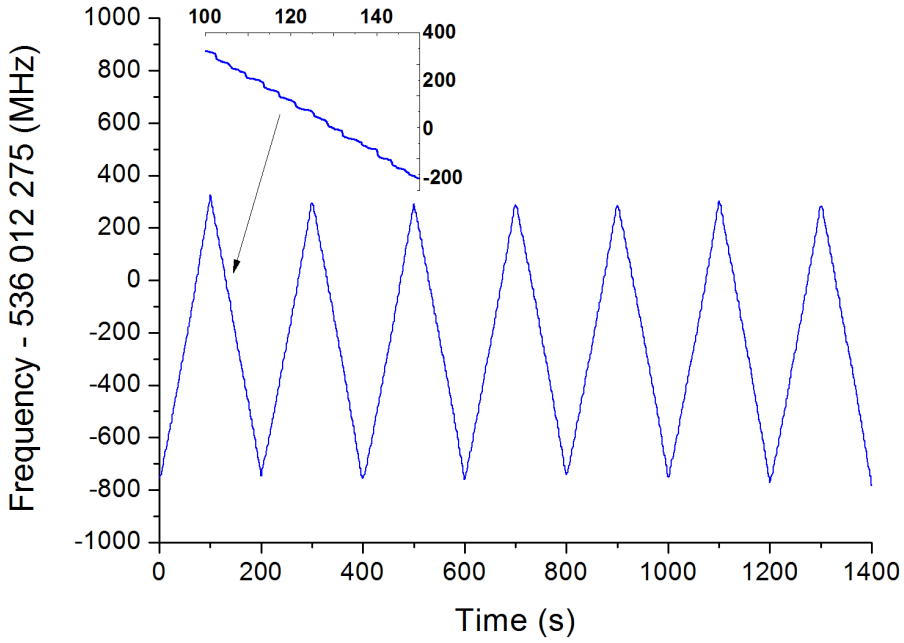

Figure 3.27: Frequency of the 559 nm green beam: a free running tuning example of the laser system.

±1.5 MHz of the set-point, as indicated in the inset. However, the oscillating behavior was present for virtually any setting of the wavemeter's PID regulator and could be caused by the steep thermal tuning slope of this laser type, which is about 11 MHz/mK at 559 nm.

Figure 3.26b shows the wavelength of the free-running laser for comparison. Surprisingly, the fluctuations are comparable to those in the locked mode: During one hour of measurement, after an initial warm-up time for both the wavemeter and the laser system, the frequency oscillated over a total range of about ±35 MHz, including a slow drift. For the experiment, the frequency was planned to be tuned over about 1 GHz range at 559 nm or 2 GHz range in the UV, in order to quickly cool the hot ions and, moreover, to record a line profile of the cooling transition. This range was found to be the longest one, consistently stable, limited by the tuning capabilities of the resonators piezo crystals. Changing the frequency of the fiber laser requires a corresponding change of the length of the doubling cavities. This has to be accommodated by the piezo holding the mirrors. Taking into account that the free running fluctuations and drifting range is much smaller than the tuning range, the laser was not locked but rather be tuned using a triangle-shaped signal, while the wavemeter was supervising the absolute frequency.

The frequency recorded with the wavemeter during such a scan is plotted in Fig. 3.27.

Relative to the tuning range, the frequency looks stable and smooth while the long-term frequency drift is at maximum about 40 MHz (at 559 nm) during the ≈25 min recording time. However, by zooming into the straight sections, it is observed that the actual tuning is not entirely smooth but more stairs like. The height of the "stairs" at 559 nm is between 10 and 25 MHz, which is similar to the jitter noticed when the laser is locked. This seems to happen because of the tuning hysteresis of the fiber laser piezo, as also declared in the manual. For the future, as mentioned in Appendix A.1, the main seeding fiber will be replaced with an external cavity diode laser. This modification will solve both, the locking problems and the polarization issue causing the power limitations of the amplified laser radiation. Nevertheless, the quality of tuning without stabilization is sufficient for the purpose of the experiment.

3.5 Mg^+ Ion Sources

Magnesium ions have to be created outside the trap and then to be injected, similar as it is foreseen for the highly charged ions. Hence, several Mg^+ sources were tested in order to check whether they meet the following conditions:

- the source can be pulsed and triggered/synchronized with the opening of the trap;
- the source has a high yield so that a sufficient number of ions for symphatetic cooling will be trapped and/or
- the ion bunch from the source has a small momentum and energy spread so that it can be collimated and transported to the trap and/or
- the ion bunch has a time extent comparable with the opening of the trap so that - if necessary - several ion bunches can be stacked in the trap.

3.5.1 Laser Ablation

Laser ablation was long studied as a method for generating pulsed plasmas with applications in deposition of thin solid films or for generating supersonic beams of particles [86]. Laser ablation occurs if a focused and pulsed laser beam hits the surface of a target. At low laser fluences, the target absorbs the energy of the laser pulse and some material from the target can be either desorbed, evaporated or sublimated. At higher laser fluences, material can be violently ejected from the target and converted into a plasma.

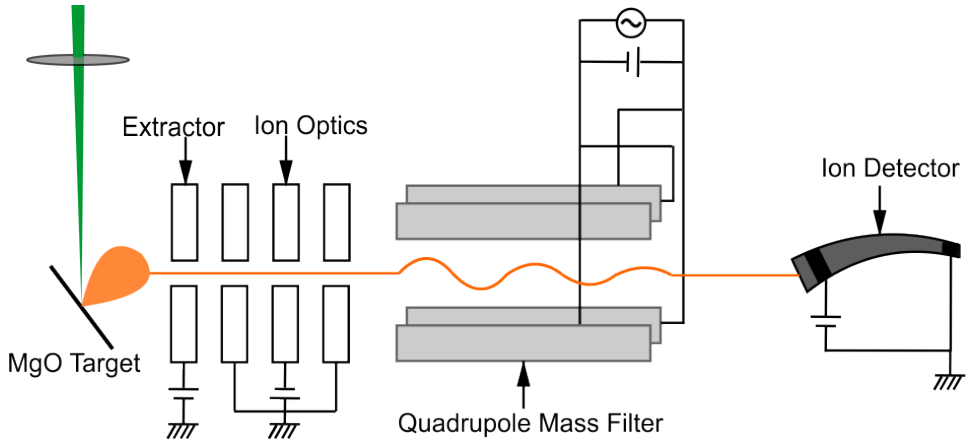

Figure 3.28: The laser ablation setup with the quadrupole mass spectrometer for tests of an ablation ion source.

Laser ablation of a Calcium target with a Nd:YAG 532 nm laser was recently also used as an ion source for linear Paul traps [87, 88]. This allows the generation of ions directly from the solid target located near the "ring" electrodes of the trap. The number of the generated particles can be controlled by the laser fluence.

The very simple experimental setup for a pulsed ion source is the greatest advantage of laser ablation. However, for our experiment it was not clear whether the very high spread in momentum and energy would be prohibitive for the transport into the trap. Nevertheless, if the yield is sufficiently large, it can compensate for the momentum/energy spread and therefore, the chance of realization was further investigated. A 532 nm (2ω) Brilliant Q-switched Nd:YAG laser was used for this purpose. The laser pulse was about 6 ns long and had a energy in the mJ range. With the aid of a 300 mm biconvex lens, the laser pulse of 9 mm in diameter was focused on the target as in Fig. 3.28. The ions were extracted from the plasma plume and guided towards an Extrel mass spectrometer consisting of ion optics, a quadrupole mass filter (QMF) and an ion detector.

Initially, a head-on geometry was tested with a metallic magnesium target perpendicular to the quadrupole axis and with the laser traveling along the axis of the mass separator, before impinging on the target surface. In this geometry, the mass spectrometer was unable to resolve the mass of the ions, since in a QMF the ions must travel sufficiently long inside to be mass separated by the applied RF field. The fast ions created here were flying through the mass filter obviously unaffected, independent of their mass.

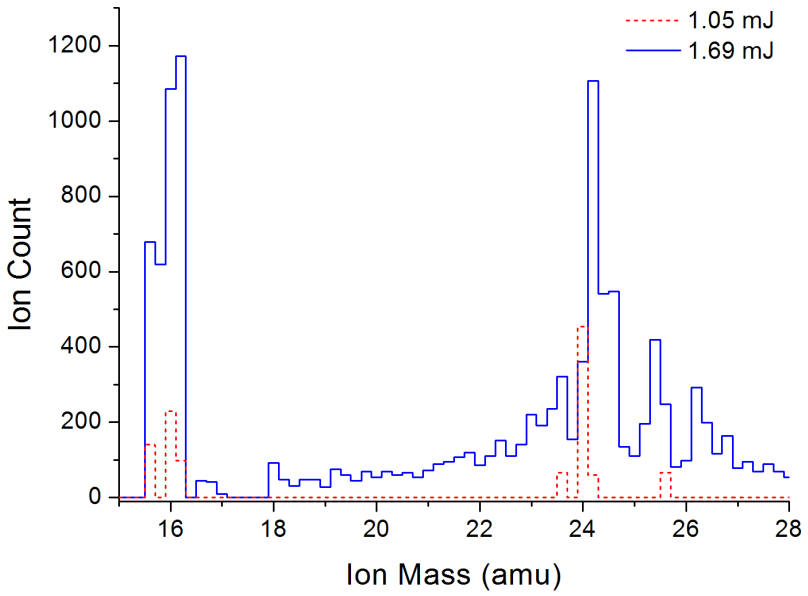

Figure 3.29: The mass spectrum from the quadrupole mass spectrometer as obtained with a laser-ablated MgO target for 1.05 mJ and 1.67 mJ pulse energy.

Consequently, the target was placed at an angle of 30° relative to the axis of the quadrupole so that the fast ions can be avoided while the slow ions can be bent into the quadrupole. Moreover, the metallic target was replaced by MgO in order to increase the chances to obtain slow, singly charged Mg ions. An example of mass spectrum is presented in Fig. 3.29. The spectrum was recorded in about 10 seconds for a pulse repetition rate of 10 Hz. It can be immediately noticed that the spread in energy is quite large, affecting the resolution of the mass spectrometer. The yield is also very small and there is no repeatability because of the target depletion and, thus, the laser position has to be constantly modified. This, together with the difficulties of installing the pulsed laser in an open hall near the experiment have led to the conclusion that laser ablation of a Mg/MgO target is not an appropriate ion source for our purpose.

3.5.2 HeatWave Ion Emitter

The second ion source tested was based on the thermionic emission of positive ions [89, 90]. Thermionic emission occurs due to the surface ionization, which involves the ionization of an element with low I_P (ionization potential) on a high work function W surface [91]. The surface should be hot enough to desorb the ions thermally and the electrons are lost to surface upon desorption. Typically, this is done by placing a sample of the material

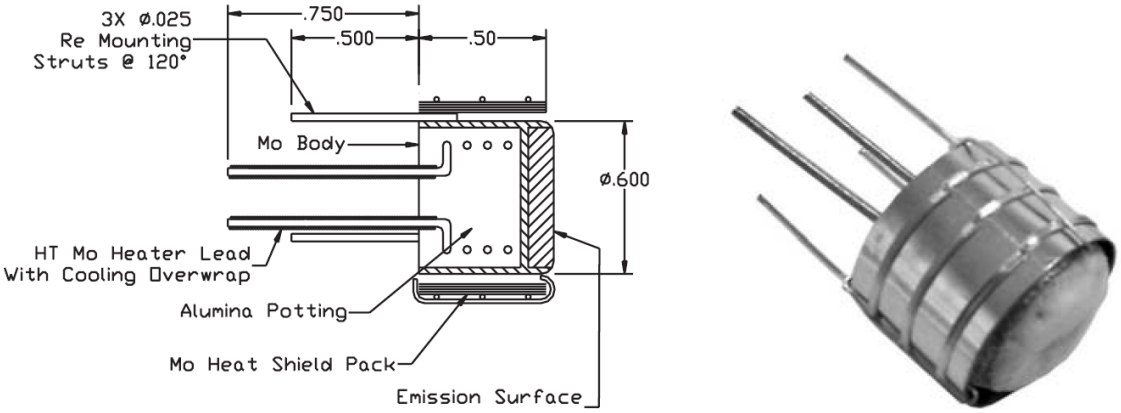

Figure 3.30: A HeatWave Labs ion emitter based on thermionic emission of positive ions [96].

of interest on a filament made from a refractory metal. When the filament is heated, a fraction of the atoms/molecules from the material evaporate as ions [92]. The current density is given by the Richardson-Dushman equation [90]

$$J = AT^2 e^{-W/kT} \tag{3.13}$$

where A is a material-dependent constant, known as Richardson's constant, T is the temperature and k is the Boltzmann constant. At thermal and charge equilibrium, the ratio of positive ions to neutral species n_+/n_0 can be calculated using the Saha-Langmuir equation [93, 94]

$$\frac{n_+}{n_0} = \frac{g_+}{g_0} \exp\left(\frac{W - I_P}{kT}\right) \tag{3.14}$$

where g_+ and g_0 are the statistical weights of the ions and neutrals, respectively. Since the evaporation rate and the temperature cannot be varied independently, the ionization efficiency [91, 94]

$$\beta(T) = \frac{n_+}{n_+ + n_0} = \frac{1}{1 + \frac{g_0}{g_+} \exp\left(\frac{I_P - W}{kT}\right)} \tag{3.15}$$

is low for atoms with $I_P > W$ and which evaporate at low temperatures [92]. Thus, this method is very efficient for alkaline metals but it was also long demonstrated to work for alkaline earths [95].

The tested ion emitters were commercial alkali ion sources from HeatWave Labs [96] similar to the one illustrated in Fig. 3.30. It consists of a molybdenum body holding the heater cavity and, separately, a cap made out of an extremely porous tungsten disc ($W = 4.55$ eV [97]), into which the emitter material was melted. The heater cavity consists

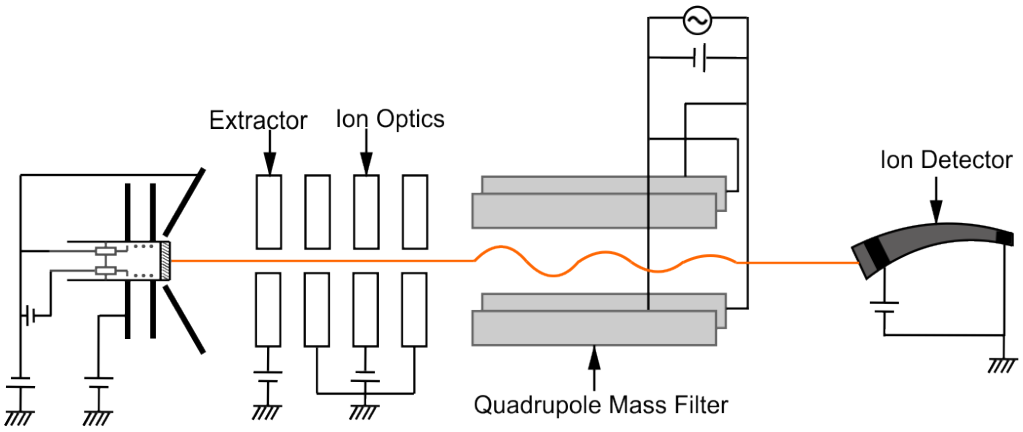

Figure 3.31: The HeatWave ion source with the quadrupole mass spectrometer for testing the ion emitter.

of a non-inductively wound coil of molybdenum wire stuck into high purity Al_2O_3. The heater leads are overwrapped with some thiner molybdenum wire for cooling and greater reliability. The ion emitter can be mounted on a support using the three equally-spaced rhenium mounting struts. Some ion emitters have an additional heat shield pack made out of three layers of 0.05 mm thick Molybdenum foil.

The manufacturer claims that these emitters have a small energy spread and are particularly suited for low-energy experiments, below 100 eV. Moreover, current densities of up to 10 mA/cm^2 are possible under optimal conditions. After several hours of heating, the ion beam should be of very high purity. Several materials can be combined into any mix ratio, yielding mixed ion beams. The emission of ions is dominant compared to the emission of neutrals, though an exact ratio is not known by the manufacturer.

A potassium ion emitter was first tested because it was available in the lab. The emitter was mounted in the middle of three electrodes as illustrated in the left side of Fig. 3.31. Two of the electrodes are in electric and thermal contact with the emitter body and are water cooled. The third electrode is in electric contact with the heater coil and is used for focusing the ion beam, though this is not absolutely necessary if appropriate ion optics are placed close to the emitter surface.

This source was initially tested using a simple Faraday cup and proved to be stable, emitting an ion current of up to 200 pA ($\cong 1.25 \cdot 10^9$ ions/s) with only 4 W of electric power. Consequently, a magnesium ion emitter was ordered and tested. After the first tests, it was noticed that the measurement and the corresponding settings are fluctuating

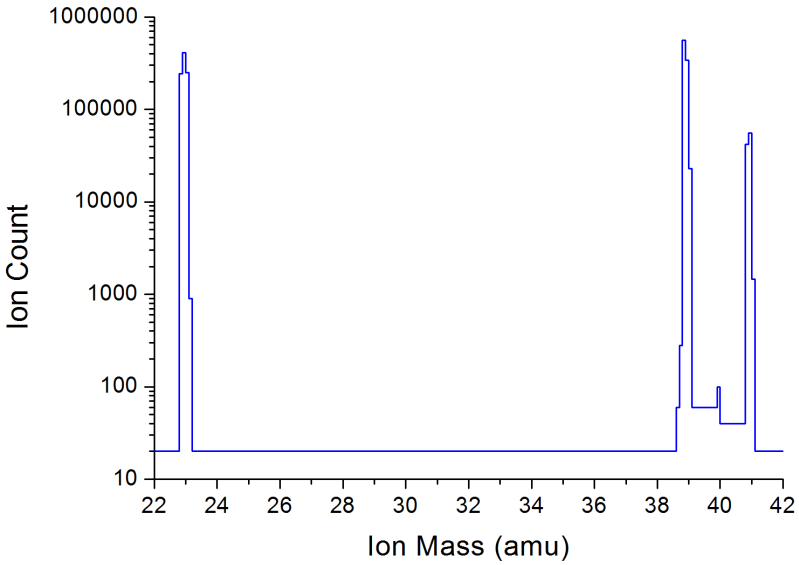

Figure 3.32: A mass spectrum example from the quadrupole mass spectrometer as obtained with a HeatWave Mg^+ ion source. While large amounts of $^{23}Na^+$ and $^{39,41}K^+$ are visible, there is no sign of $^{24}Mg^+$

and, thus, the source was placed for ion discrimination in front of the mass spectrometer presented in the previous subsection.

Unfortunately, there was no measurable amount of Mg ions at the maximum electric power recommended by the manufacturer for this emitter (12 W). The observed threshold for emission of Mg ions was at 18 W, a heating power at which there is already a significant emission of sodium and potassium ions, as shown in Fig. 3.32. A consistent amount of about 4000 cps of Mg ions was measured only at a power of 25 W. This was far beyond the manufacturer's recommendation for operation and resulted in current leaking from the heater coil to the emitter body. At this power, about $3{\cdot}10^5$ cps of ^6Li and $3{\cdot}10^6$ cps of ^7Li were also measured. This is in accordance with Eq. (3.15), considering the work function of tungsten $W = 4.55$ eV and the first ionization potential of the observed elements, given in Table 3.7 [97].

Admittedly, the alkali-earth sources are advertised as experimental by the manufacturer and stated to be "quoted on a best efforts basis only". Nevertheless, the magnesium ion emitter proved to be completely useless.

Table 3.7: First ionization potential of the observed elements.

Element	First I_P (eV)
Lithium (Li)	5.39
Sodium (Na)	5.14
Magnesium (Mg)	7.65
Potassium (K)	4.34

3.5.3 Electron-impact Ion Source

The last tested ion source was based on electron-impact ionization and was designed especially for this experiment, based on a high-temperature atomic beam source that was available. The efficiency of an electron-impact ion source depends on the amount of electrons and atoms as well as on the energy of the electrons and density. The ionization probability for an atom crossing an electron beam with a flux Φ_e is given by

$$P = \sigma_I(E)\Phi_e \tag{3.16}$$

with the ionization cross section $\sigma_I(E)$.

The energy dependence of the cross section for the single ionization of neutral atoms rises at the threshold, given by the ionization potential I_P of the atom, proportional to $E^{1.127}$ (Wannier's law [98]), reaches a maximum at about $3-5\times I_P$ and decreases at high energies $\sim \frac{\ln E}{E}$ due to decreasing interaction times.

For the ionization cross section of Mg, the latest values with the corresponding references can be found in [99] and are presented in Fig. 3.33. The peak cross section of about $5{\cdot}10^{-16}$ cm^2 appears at an electron energy of 17 - 21 eV, while the threshold for the ionization is at 7.64 eV.

The complete electron-impact ion source is illustrated in Fig. 3.34. The oven is formed from a rolled tungsten foil welded between two steel plates. The plates are sitting on two water-cooled steel rods through which a current of about 25 A is flowing, required to heat the oven filled with Mg fragments ($\approx 1-2$ mm in diameter). It was observed that the usage of Mg metallic powder or with very small fragments, delayed the emission of atomic magnesium and led to a less reliable operation of the source. In this case it was required to apply a significantly higher heating current, which also poses a risk of coating the ionizer. The reason for this is not fully understood, but is most probably caused by the oxide layer at the surface of Mg fragments/grains. The Mg fragments/grains must be

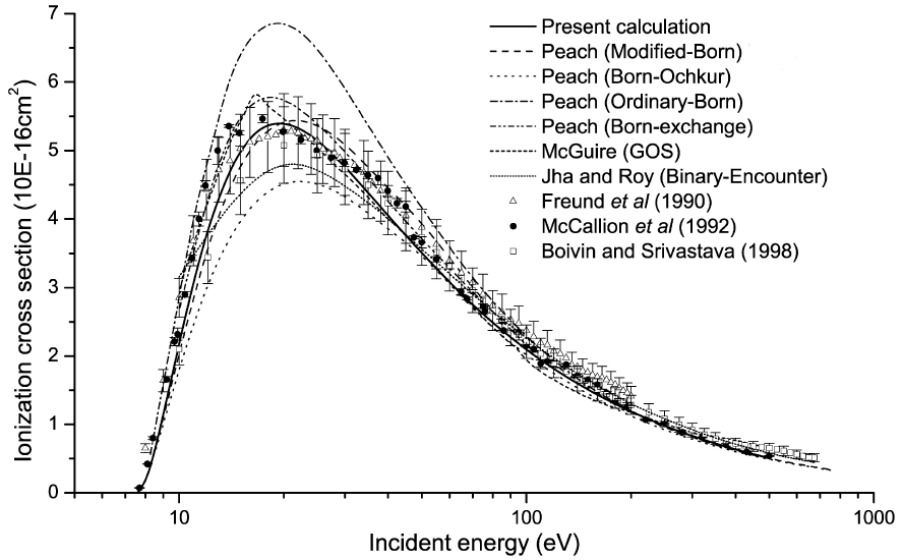

Figure 3.33: One of the latest calculation of the single ionization cross section for Mg compared with other theoretical calculations (lines) and recent experimental results data points. The figure is taken from [99].

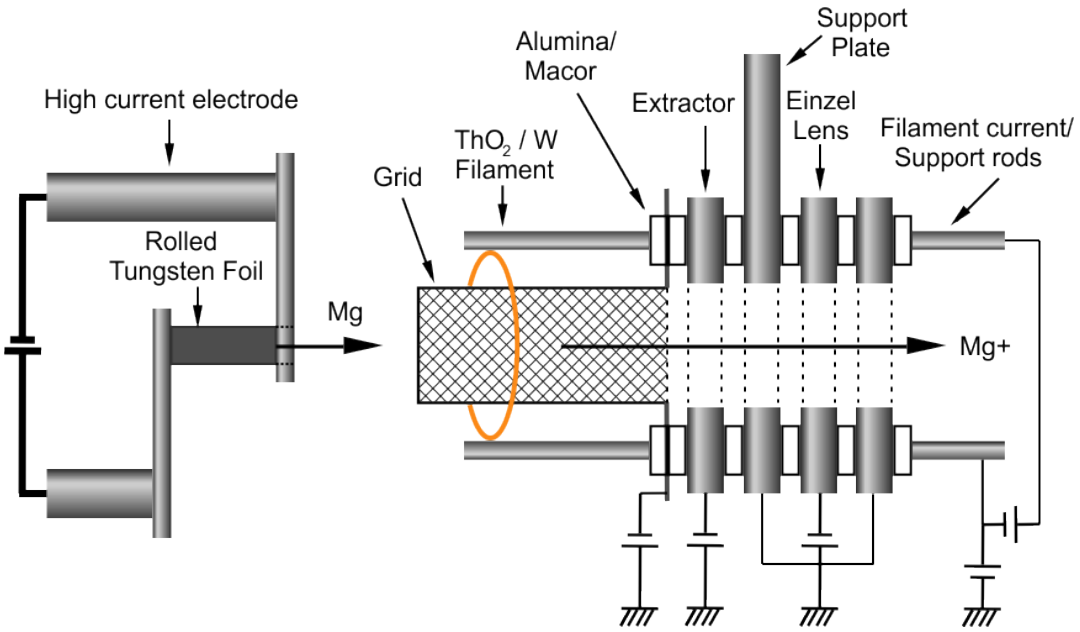

Figure 3.34: The complete Mg^+ electron-impact ion source with the oven and initial shaping ion optics.

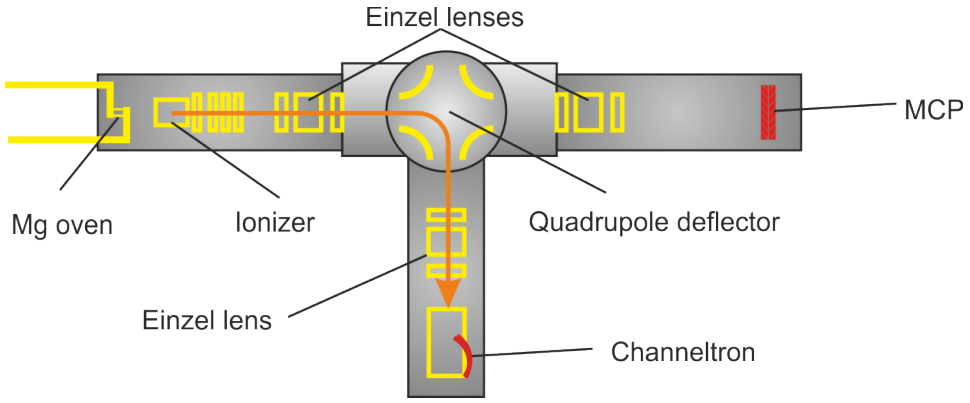

Figure 3.35: The time-of-flight (TOF) mass spectrometry setup for analyzing the output of the electron-impact ion source.

initially fissured and the amount of Mg atoms which can be emitted is larger for bigger chunks.

The atoms leaving the oven enter the metallic grid, which represents the ionization region. The grid was manufactured by Stanford Research Systems, Inc. and is part of a replacement kit for a residual gas analyzer. The electrons for the impact ionization are produced with a filament made out of a 0.2 mm thick thoriated-tungsten (99% W, 0.9% Th_2O) wire from Advent Research Materials. Heating currents of about 4 A are typically used to obtain efficient electron emission. They are accelerated towards the grid by a negative bias voltage on the filament of about -20 V, which is in the region of maximum cross section. The electrons are largely transmitted through the grid and cross the atomic beam on the axis. The highest ionization efficiency was obtained for around 0.5 mA electron current measured between the filament and the grid.

The ions are guided out of the grid with an extractor and the ion beam is shaped with an einzel lens as shown in Fig. 3.34. For pulsed ion extraction, the grid is pulsed with a rectangular high-voltage pulse with a width of 1 μs and tunable repetition frequency. The energy of the ions can be tuned by changing the amplitude of the grid HV pulse.

For analyzing the output of the ion source, the beamline and the beam analysis section were used as a time-of-flight (TOF) mass spectrometer setup. The relevant part of the beamline is shown in Fig. 3.35. The ions are focused with an additional einzel lens, bent at 90^o with an electrostatic quadrupole deflector and again refocused with an einzel lens before impinging on an off-axis channeltron ion detector. The time-of-flight for the 142 cm between the ion source and the channeltron depends on the mass of the ion, for the same

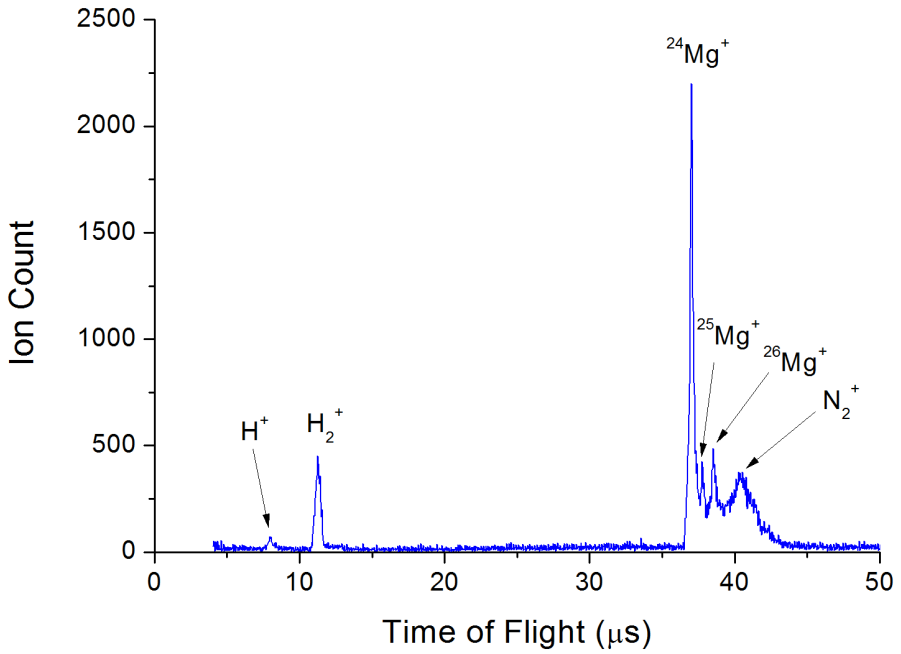

Figure 3.36: An example of TOF mass measurement for 200 eV ion energy and 142 cm distance between the source and the detector.

value of energy. A TOF mass spectrum, integrated over 500 ion pulses, is presented in Fig. 3.36 for the following parameters: 200 eV ion energy, 13 eV electron impact energy, 0.55 mA electron current and -310 V extractor bias. It was estimated that the number of Mg ions in a bunch is between 10 and 50. The energy spread is small enough to resolve the three peaks corresponding to the Mg^+ natural isotopic abundance (^{24}Mg: 78.60%, ^{25}Mg: 10.11%, ^{26}Mg: 11.29% [100]) in the TOF measurement.

The values for the threshold energy and peak energy of the Mg cross section are generally lower than the values for the impurities species found in vacuum (typically combinations of H, O and N). It was experimentally found that by tuning the energy of the electrons, the peaks corresponding to the impurities can be reduced without affecting the Mg peak too much, as in the mass spectrum shown in Fig. 3.36.

The small energy spread, in combination with the good transport efficiency and reproducibility of the output, meets the conditions required for external ion injection into the trap and was consequently used in the experiment.

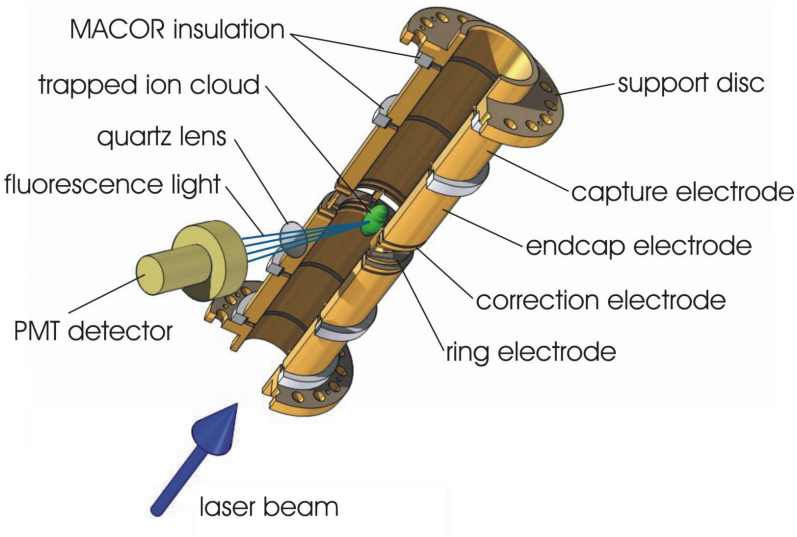

Figure 3.37: The cylindrical Penning trap used in the SPECTRAP experiment.

3.6 Spectrap Overview

The trap designed for the spectroscopy of HCI [12] is shown in Fig. 3.37. It is a cylindrical Penning trap [15, 21] with correction electrodes for the compensation of the electric field inside the trap. Additionally, it has two capture electrodes which facilitates the initial trapping of the externally injected ions. The inner diameter of the trap is 21 mm while the distance between the capture electrodes is 68 mm. The ring electrode is split in four segments to allow the implementation of the FFT-ICR method.

The laser beam is sent axially while the fluorescence is collected radially through two of the four orthogonal observation tubes. The other tubes are closed to reduce heat flow from the outside to the 4 K environment inside. Therefore, each of the ring electrodes has a hole. To collect as much fluorescence as possible at one observation tube, the hole in front of the tube is equipped with a quartz collimation lens, while the opposing ring electrode is equipped with a plano-concave mirror which reflects a large part of the fluorescence towards the optical detector. This can be seen in Fig. 3.38. The electrodes are gold-plated and separated with Macor insulation in a geometry which avoids electrostatic charging.

The required magnetic field for the Penning trap is generated by a Helmholtz-type (split-coil) superconducting magnet as depicted in Fig. 3.39. The coils are immersed in liquid helium and additionally shielded by a liquid nitrogen tank. The magnesium ions are

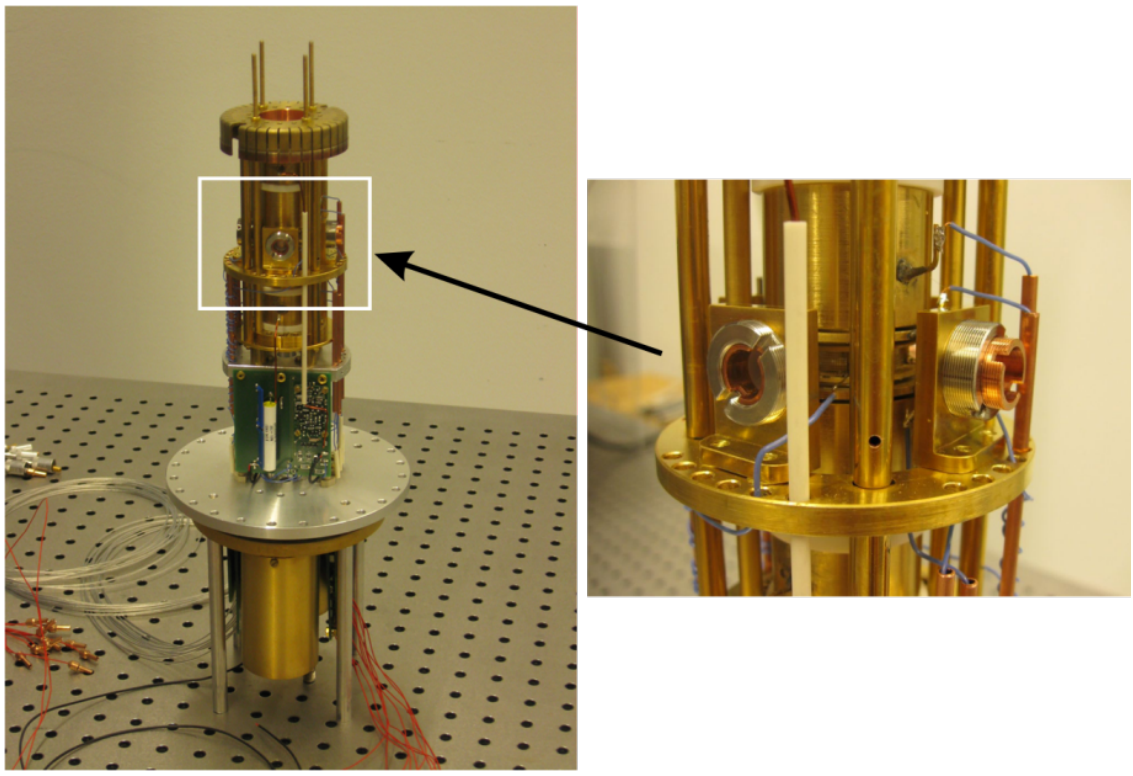

Figure 3.38: Photo of the Penning trap with a zoom on the optical elements.

produced by the ion source described in the previous subsection and guided into the trap through several einzel lenses and further ion optics: A quadrupole deflector for bending, an electric quadrupole for beam shaping and two pulsed drift tubes which can act as energy elevators and decrease the energy of the ions, if required. Two ion detectors - a microchannel plate (MCP) and a channeltron detector - are available for measuring the ion yield from the ionizer and for detecting the ions flying through the trap.

The required high-vacuum is obtained with two turbo pumps, two ion pumps and through the cryogenic pumping by the 4 K/73 K surfaces of the cold magnet bore and of the liquid helium/nitrogen tanks. To reduce the desorption flow from the surface, the setup is baked on 120°C for several days. The pressure near the upper turbo pump was in the low 10^{-8} mbar region while near the lower turbo pump it was in the low 10^{-9} mbar region. The vacuum in the cryogenic trapping region cannot be directly measured but was estimated from the trapping lifetime to be better than 10^{-10} mbar. By removing the upper ion pump, the system can be easily adapted to accept ions from a second source like an EBIS or HITRAP. Two photos are provided in Fig. 3.40, where the location of the

proposed beamline from HITRAP can be seen.

The trap is located in the homogeneous field region in the middle of the magnet. The magnet can provide a magnetic field up to 6 Tesla. A field of 4.1 Tesla was typically used throughout the experiments. The trap is in thermal contact with the magnet bore, as required by the cryogenic electronics for the resistive cooling/axial detection and FFT-ICR. The split-coil configuration allows the radial optical access to the center of the trap required for the fluorescence detection. The fluorescence detector setup was designed and produced at the University of Münster [101] and is based on a half-inch MCP-type optical sensor. A 50 cm μ-metal extension is used to protect the sensor from the high magnetic field and a corresponding lens is used to focus the collimated fluorescence on it. It has a very low dark count rate - less than 20 cps (counts per second) - and it offers an excellent quantum efficiency, $\approx$18% at 280 nm. From solid angle and ray transfer calculations, it was estimated that approximatively 0.15% of the total fluorescence reaches the detector if the ion cloud is less than 1 mm in diameter.

The main limitation of system operation is the high consumption of liquid helium. Normal operation typically requires up to 100 liters for the initial cooling and additionally 20 liters for every day of operation, thus strongly limiting the operation time. Therefore, operation of the trap for test measurements was only possible three times for two-weeks periods.

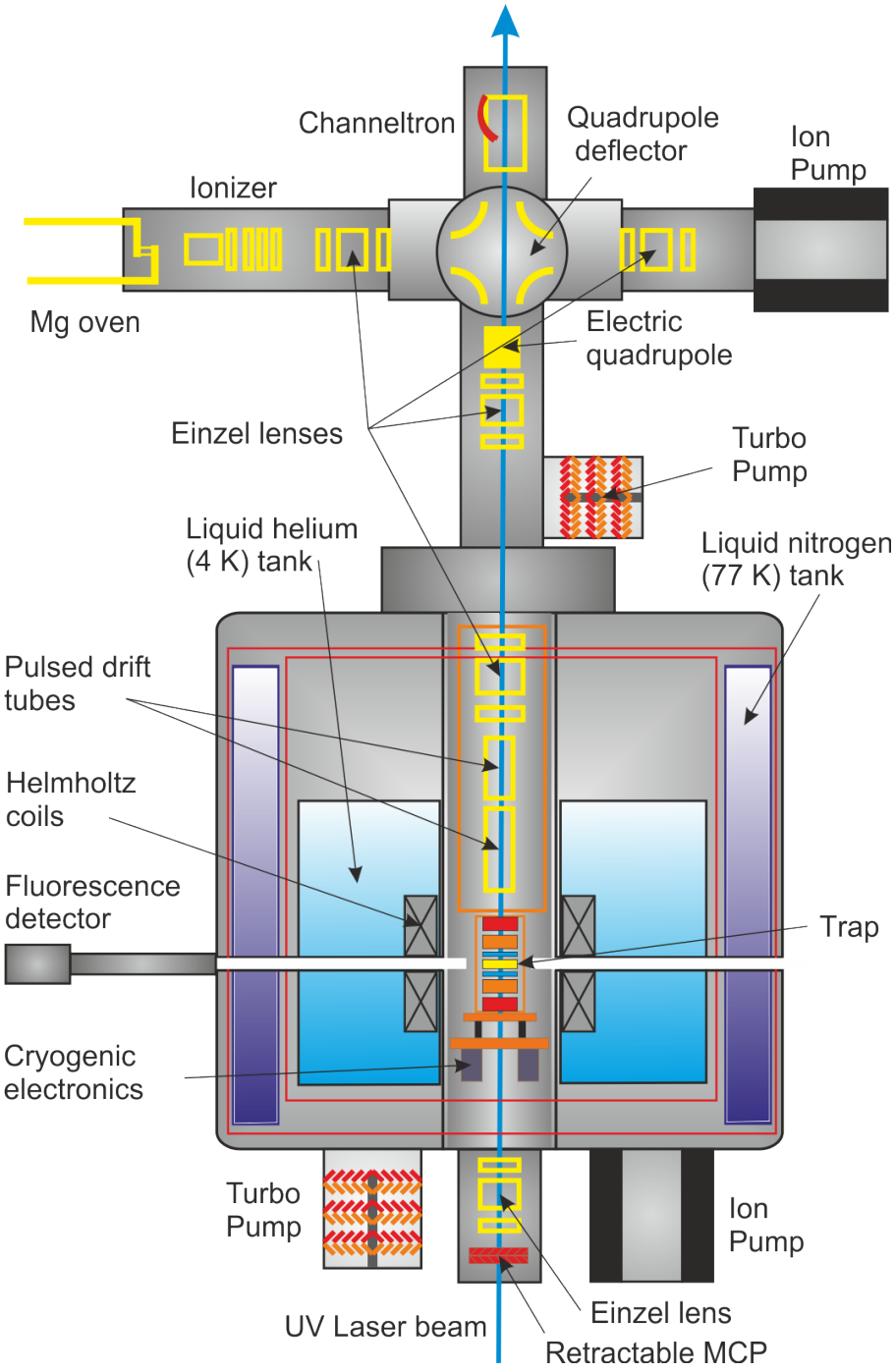

Figure 3.39: The complete trap setup with the superconducting magnet and the ion source.

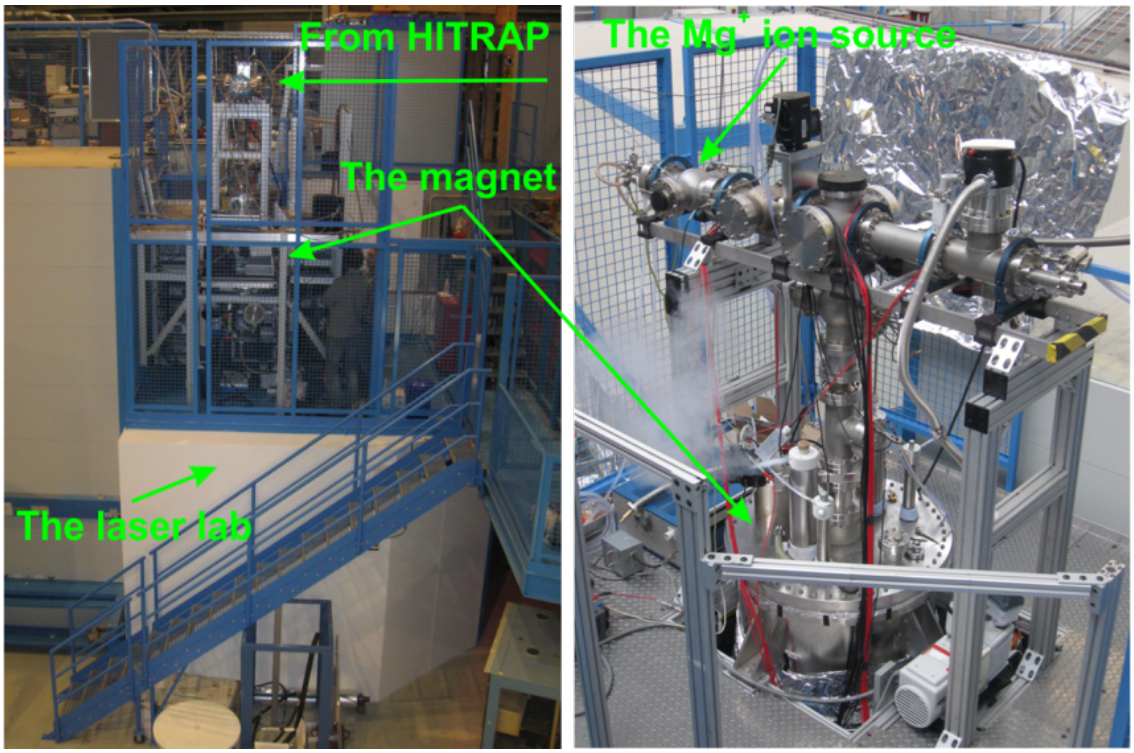

Figure 3.40: Photos of the beamline (right) and the SPECTRAP platform (left), with the location of the proposed beamline from HITRAP marked.

4

Results

4.1 Externally Injected Ions - Stacking and Trapping

In general, the easiest way to trap ions is to produce them continuously inside the trap. In this way, the trap can be kept closed and even with a low ion production rate it is still possible to trap a large amount of ions. This is done for magnesium and other metals by overlapping inside the trap the atomic beams from a Mg-filled oven and either an electron-emitting filament placed near the trap and operated as an electron gun [102] or a laser beam for resonance ionization [103]. Unfortunately, this option is not possible at SPECTRAP because of the cryogenic environment around the trap and the spatial limitations inside the bore.

Considering the small number of Mg ions in a single pulse from the source presented in Subsection 3.5.3, several ion bunches have to be stacked. Taking into account previous experiences with sympathetic cooling in the scientific literature, e.g. [33, 40, 41, 42], the aim was to have 10^4-10^5 Mg ions simultaneously trapped. That corresponds to the stacking of at least 200 bunches, assuming almost no ion loss.

A typical stacking and trapping sequence is presented in Fig. 4.1. The capture electrodes are first maintained at a trapping potential. When the first ion bunch arrives (1), the upper capture electrode is lowered, the ions can enter and are then reflected by the lower capture electrode. Before they can leave, the upper capture electrode potential is raised back to the trapping potential (2). Laser cooling starts immediately. Once the next pulse from the ion trap arrives (3), the upper capture electrode is lowered to an intermediate potential, allowing the next bunch to enter but preventing the trapped ions from leaving the trap. This cycle is repeated until a sufficient number of ions are trapped.

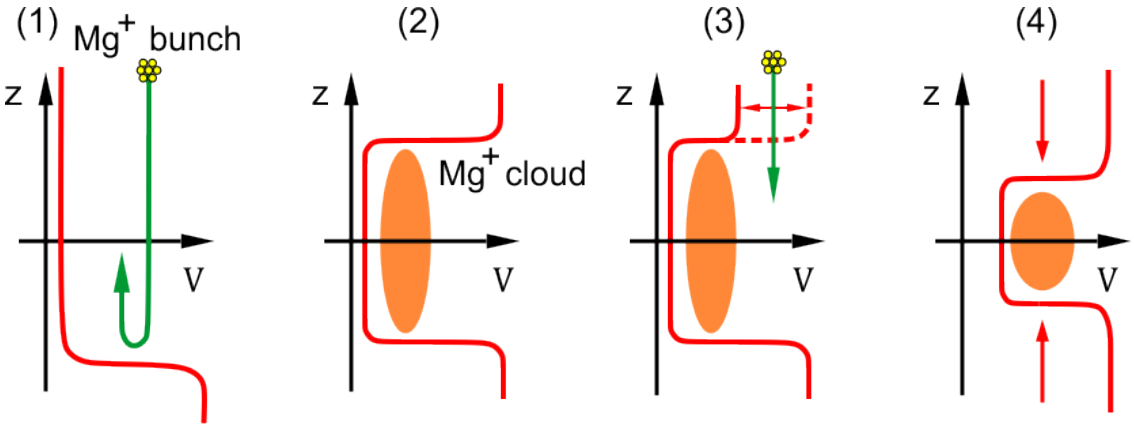

Figure 4.1: Stacking of several bunches of externally injected ions.

Finally, the potential on the endcaps and ring electrodes can be raised (4) so that the ions are compressed in the middle of the trap.

In order to have minimum losses and to trap a large amount of ions, several conditions have to be met:

- the trap should be opened for a period of time less than twice the travel time of the ion bunch between the upper and the lower capture electrodes, taking into account also the temporal spread of the bunch, so that the whole bunch is trapped;
- a fast cooling method should be used that will reduce the ions energy sufficiently, so that they will still be trapped by the intermediate potential in step (3), when the next bunch arrives;
- the total stacking time should be shorter than the lifetime of the ions inside the trap, so that more ions are added to the trap within one cycle than are lost through typical loss processes.

The first condition is generally fulfilled due to the small spread in energy of the Mg ion source (Fig. 3.36) and by using a fast HV switch. For fulfilling the second condition, laser cooling and longer periods between ion bunches are used during stacking while extending the total stacking time. For the third condition, a higher stacking frequency and a shorter total stacking time would be required. Thus, there is a trade-off between the last two conditions and an optimization process is required to enhance the total number of trapped ions.

Experimentally, the following conditions were found to be optimal: The Mg ions were accelerated by the grid to 200 eV. The upper capture electrode was synchronized to be lowered after 65.6 μs for a duration of 2.5-3 μs from 300 V to 140-150 V. The total flight time of the 200 eV ions inside the trap is 3.4 μs and the HV switch has a rise time smaller than 0.1 μs. The repetition rate was found to be optimal in the 1 Hz range, while the maximum corresponding to the equilibrium between the gain and the losses was already obtained for a total stacking time of less than 60 seconds. Thus, the number of captured ions typically ranged between 500 and 2000. However, this will not be sufficient to efficiently cool a bunch of HCI. Therefore, conditions will have to be improved - a better ion source and lower losses are required. This can be easily done, as explained in the following chapter.

4.2 Cooling Time

To determine the cooling time, the trap was filled using the procedure described above. Then the endcaps were raised to 330 V and the ring electrodes to 100 V. As described in Subsection 2.3.2, the ions are cooled near the turning points along the axial motion, since (2.45) is fulfilled for the trapped Mg^+ ions. An example of the fluorescence signal is presented in Fig. 4.2 for a stacking time of 30 seconds and 1 Hz repetition frequency of the ion source. The laser frequency was kept fixed, red-detuned by 300 MHz and the laser beam intensity corresponded to 1/3 of the saturation intensity[1] ($I_{\text{sat}} = 2.5$ mW/mm^2 [39]) over a diameter of roughly 1 mm in the center of the trap.

Initially, the ions have a large spatial oscillation amplitude between the endcaps while the fluorescence detection system is focused on a small volume at the center of the trap. As mentioned in Section 3.6, the optical detector is geometrically calculated to pick 0.15% of the fluorescence if the ion cloud is 1 mm in diameter. Hence, the photons emitted outside this region are not recorded by the detection system. After a few seconds, the ions are cooled to a low temperature corresponding to the laser detuning and the ion cloud is concentrated in the middle of the trap. This, together with an increase in the fluorescence rate per ion, results in the sharp peak in Fig. 4.2 appearing about 8.6 seconds after the endcaps were raised to the trapping potential.

[1] valid for the leftmost transition in the Zeeman-splitted fine structure from Fig. 4.5, for which the Clebsch-Gordan coefficient is $C_{CG} = 1$ [39]

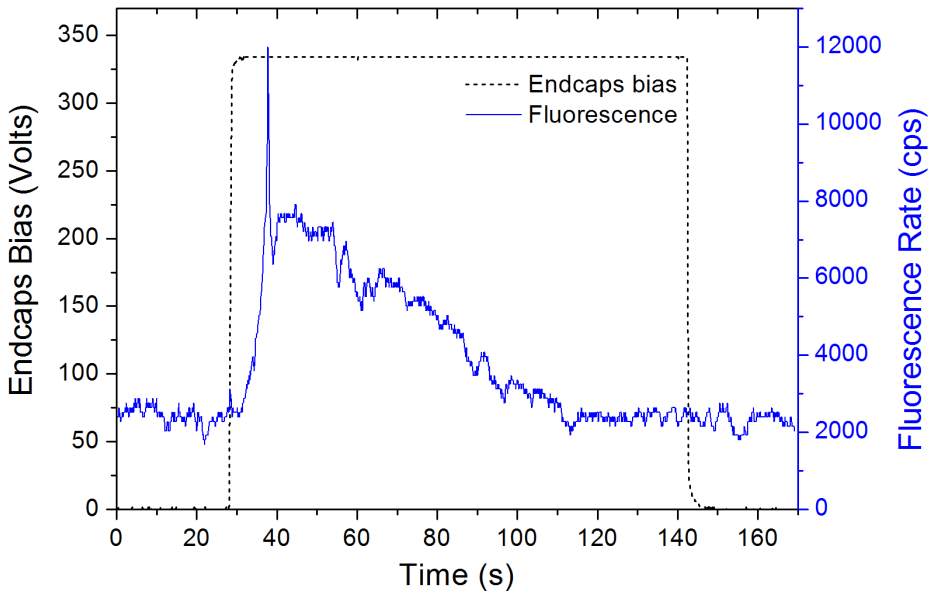

Figure 4.2: The time evolution of the fluorescence rate after closing the trap with a 300 MHz red-shifted laser.

Equation (2.46) from Subsection 2.3.2 can be used to approximate the cooling time for a laser intensity close to or above the saturation. Since in this case, the laser is 1/3 of the saturation intensity, the cooling force has to be calculated accordingly. This can be done, in a first approximation, by comparing Eq. (2.40) corresponding to the force for very high laser intensities with Eq. (2.39) for a very small detuning and a strong transition

$$\frac{F_{\text{scatt}}(I)}{F_{\text{max}}} = \frac{I/I_{\text{sat}}}{1 + I/I_{\text{sat}}} \tag{4.1}$$

and thus the scattering force in Eq. (2.46) at 1/3 of the saturation intensity becomes

$$F_{\text{scatt}}(I_{\text{sat}}/3)) = \frac{1}{4}\hbar k \frac{\omega_z}{\pi}. \tag{4.2}$$

With a further approximation that the ion will always experience the maximum deceleration at this laser intensity

$$a_{\text{max}}(I_{\text{sat}}/3) = \frac{1}{4\pi}\frac{h\omega_z}{\lambda m} \tag{4.3}$$

where λ is the wavelength of the cooling laser and m the mass of $^{24}Mg^{+}$, the stopping time can be calculated according to

$$t_0 = \frac{v_0}{a_{\text{max}}} \tag{4.4}$$

where v_0 is the initial speed of the ions. For 200 eV ions and 1/3 of the saturation intensity, under the previously detailed experimental condition, the stopping time should be approximatively 2.7 seconds. However, it cannot be expected that every ion absorbs at each turning point neither that it experiences the maximum deceleration every time. Moreover, in the beginning, the ion cloud is expected to have a larger spatial extent which would not be covered by the laser and some of the ions will have to be cooled sympathetically by the ions crossing the laser path. All these processes can extend the duration of the cooling process. Therefore, the agreement between the estimated and the experimental value is quite reasonable.

4.3 Laser Cooling of $^{24}Mg^{+}$ - Line Profile and Limit Temperature

In order to improve the reproducibility of the measurement, the trapping sequence was automatized as described in Fig. 4.3. During the stacking time, which is typically between 1 second and a couple of minutes:

- the ion source grid is pulsed with a 1-μs pulse and typically 3 Hz repetition frequency from 0 to 200 V;
- the upper capture electrode is pulsed correspondingly with a delay of 65.6 μs relative to the grid pulse for a duration of 2.5-3 μs from 300 V to 140-150 V, as already stated in the previous section;
- the lower capture electrode is maintained at 300 V;
- the laser frequency is kept fixed at 0.5-1.5 GHz detuning.

After the fall of the stacking gate, a trapping gate is generated. During this time, which is typically between 10 seconds and a couple of minutes:

- both the upper and the lower capture electrodes are maintained at 300 V;
- the endcaps potential is raised to 330 V;
- the ring potential is raised to 100 V;

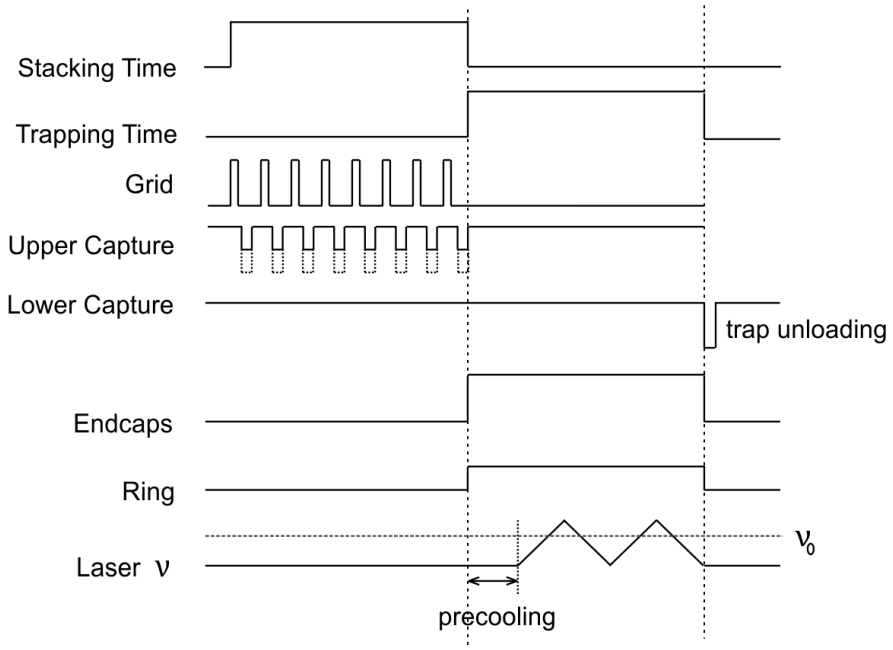

Figure 4.3: The typical loading, trapping and unloading sequence.

- for obtaining the line profile, the laser frequency is tuned repeatedly across the central frequency, with an adjustable delay - typically 10 seconds - for the precooling of the ion cloud, as described in the previous section.

After the fall of the trapping gate, the lower capture electrode is grounded for a short time in order to empty the trap of any remaining particles.

A typical line profile of the $^{24}Mg^{+}$ cloud during laser cooling is presented in Fig. 4.4. The stacking time was 1 minute and the laser was tuned in 10 seconds over a range of 1 GHz from red to blue detuning, after a precooling time of 10 seconds. The precision of the frequency scale and the shape of the line profile is limited by the tuning capabilities of the fiber laser, as described in Section 3.4.

The peak is strongly asymmetric because of the ions being rapidly heated when the laser crosses the central transition frequency. Nevertheless, the full width at half maximum (FWHM) can be approximated as twice the width at half maximum between the cooling slope and the central transition frequency. From Fig. 4.4, the FWHM can thus be approximated to be around 80 MHz. Considering the natural linewidth of $\delta\nu_{\mathrm{nat}} = 42$ MHz [84] and the imprecision of the frequency scale and by using Eq. (1.2) from Section 1.2, a conservative upper limit of the temperature of the $^{24}Mg^{+}$ cloud can be estimated to be of the order of 0.1 K.

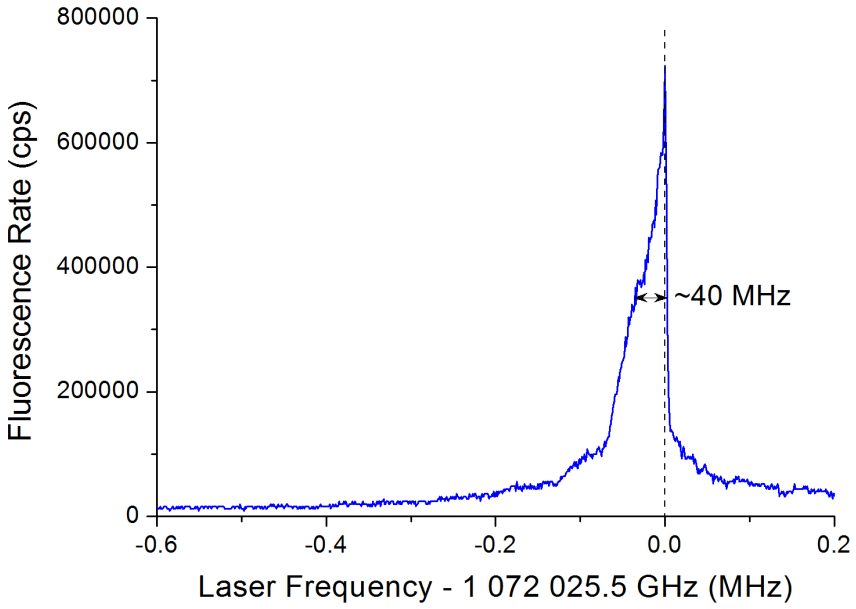

Figure 4.4: A typically measured line profile of the $^{24}Mg^{+}$ cloud during laser cooling.

4.4 Zeeman Shift and Polarization Dependence

Because of the external magnetic field required for the trapping, the additional Zeeman splitting [104] of the fine structure levels involved in the transition is present, as depicted in Fig. 4.5. The Zeeman effect shifts the m_j levels in an external magnetic field with [36]

$$\Delta E_{\mathrm{ZE}} = g_j \mu_{\mathrm{B}} m_j B \tag{4.5}$$

where μ_{B} is the Bohr magneton and g_j is the Landé g-factor which can be approximated by

$$g_j = 1 + \frac{j(j+1) + s(s+1) - l(l+1)}{2j(j+1)}. \tag{4.6}$$

The Landé g-factor for the $^2S_{1/2}$ level is g_j=2 while for the $^2P_{3/2}$ level it is g_j=4/3. The calculated Zeeman shifts in terms of frequency of the m_j levels for $^{24}Mg^{+}$ are summarized in Table 4.1.

To avoid pumping into dark states, the leftmost transition ($-\frac{1}{2} \rightarrow -\frac{3}{2}$) in Fig. 4.5 was chosen for the cooling process. For the chosen transition, there is a Zeeman shift of -13.996 GHz/T compared to the unperturbed $^2S_{1/2} \rightarrow ^2P_{3/2}$ transition at $\nu_0 = 1\ 072\ 082.934$ GHz [84]. Compared to the σ^+-pumping, it has the advantage that the laser is also red-detuned for all neighboring π transitions, e.g. the π transitions $-\frac{1}{2} \rightarrow -\frac{1}{2}$ and $+\frac{1}{2} \rightarrow +\frac{1}{2}$, which still partially accept the σ^- polarization, whereas cooling

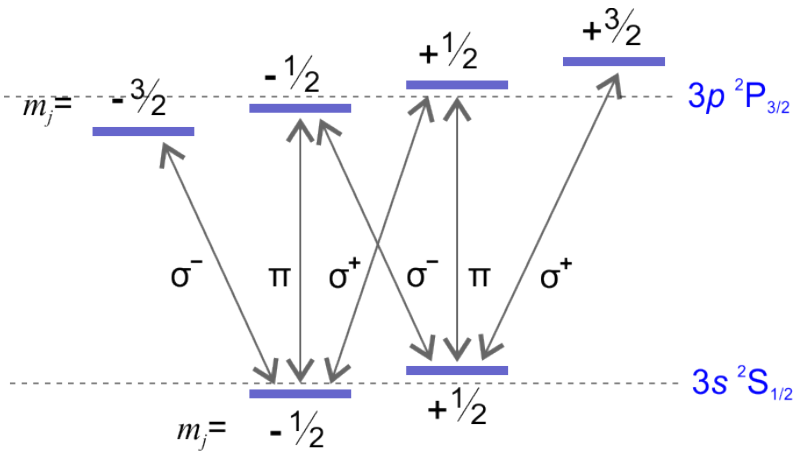

Figure 4.5: The Zeeman splitting of the fine structure for $^{24}Mg^+$ in an external magnetic field with the polarization required for the excitation light.

Table 4.1: The Zeeman shifts of the m_j levels in an external magnetic field for $^2S_{1/2}$ and $^2P_{3/2}$ in $^{24}Mg^+$.

Level	m_j	$\frac{\Delta E_{ZE}}{hB}$ **(GHz/T)**
$^2S_{1/2}$	$-1/2$	-13.996
$^2S_{1/2}$	$+1/2$	$+13.996$
$^2P_{3/2}$	$-3/2$	-27.992
$^2P_{3/2}$	$-1/2$	-9.331
$^2P_{3/2}$	$+1/2$	$+9.331$
$^2P_{3/2}$	$+3/2$	$+27.992$

Table 4.2: The absolute frequency ν_B and the corresponding Zeeman shift $\Delta\nu_B$ at 4.1 T for the possible transitions between the $^2S_{1/2}$ and $^2P_{3/2}$ levels in $^{24}Mg^+$.

m_j **of** $^2S_{1/2}$	m_j **of** $^2P_{3/2}$	**Polarization**	$\Delta\nu_B$ **(GHz)**	$\nu_B(4.1$ **T) (GHz)**
		$B = 0$ T	0	1 072 082.9 [84]
$-1/2$	$-3/2$	σ^-	-57.4	1 072 025.5
$-1/2$	$-1/2$	π	$+19.1$	1 072 102.0
$-1/2$	$+1/2$	σ^+	$+95.6$	1 072 178.5
$+1/2$	$-1/2$	σ^-	-95.6	1 071 987.3
$+1/2$	$+1/2$	π	-19.1	1 072 063.8
$+1/2$	$+3/2$	σ^+	$+57.4$	1 072 140.3

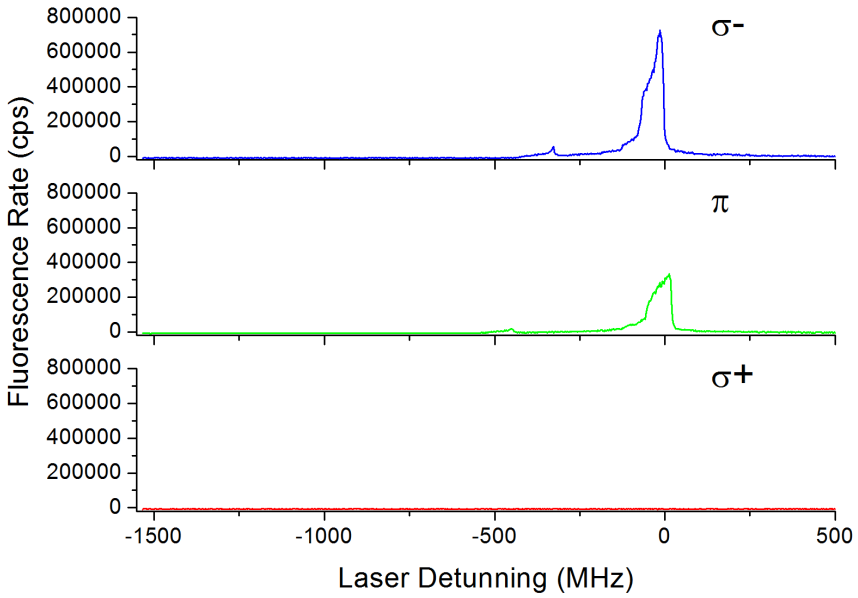

Figure 4.6: The line profile of the $^2S_{1/2}$, $m_j = -1/2 \rightarrow {}^2P_{3/2}$, $m_j = -3/2$ transition for the three different polarizations.

on the $+\frac{1}{2} \rightarrow +\frac{3}{2}$ transition would heat via the wings of these two π transitions. The values of the absolute frequency and the Zeeman shift at 4.1 T for the possible transitions are summarized in Table 4.2.

A fluorescence signal from the $m_j = -\frac{1}{2} \rightarrow m_j = -\frac{3}{2}$ transition at 1072025.5 THz for the three different polarization options is depicted in Fig. 4.6. The stacking time was 40 seconds at 3 Hz repetition frequency of the source and the laser was tuned over a range of 2.12 GHz in 100 s, without precooling time. Since the π (linear) polarization can be considered as a coherent superposition of σ^+ and σ^- light, the fluorescence rate is about half compared to the case with the "pure" σ^- (circular) polarization. As expected, there is practically no observable fluorescence at this frequency for σ^+ polarization.

As explained in Section 4.2, with a fixed red-shifted laser, there is an initial cooling time (≈ 9 s) after which the ions are cooled to the temperature corresponding to the laser detuning and the ion cloud is concentrated in the middle of the trap. Therefore, when scanning the laser frequency, the laser is initially maintained at fixed red-detuning for a precooling time, as depicted in Fig. 4.3. There is no precooling time here, but the cooling speed is much faster than the laser tuning and, at the moment when the ions temperature match the laser frequency for cooling, a small bump in the fluorescence is observed [105]. This can be noticed before the main peak and corresponds to the moment when the cloud

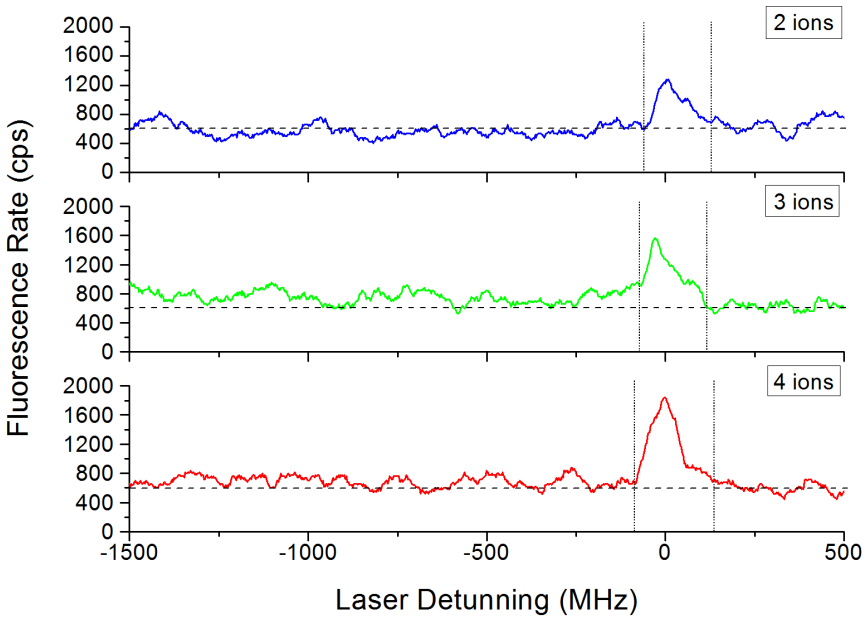

Figure 4.7: The fluorescence signals for 2, 3 and 4 trapped ions. The dashed line represents the subtracted fixed background from each spectra while the dotted vertical lines represent the integration limits.

is bunched in the center of the trap.

4.5 Quantized Laser Fluorescence and Number of Ions

To evaluate the number of trapped ions, the stacking time was more and more reduced in order to observe the minimum amount of fluorescence which would correspond to a single trapped ion. The threshold for a detectable fluorescence was found at a stacking time of 1 second at 3 Hz repetition frequency. Under these conditions sometimes there was even no fluorescence at all.

The laser was maintained at 1/3 of the saturation intensity and was tuned over a range of 1 GHz in 10 seconds. Some examples of fluorescence signals are presented in Fig. 4.7, corresponding to a supposed number of 2, 3 and 4 trapped ions. The background is quite high and the fluorescence from a single ion was consequently experimentally not distinguished from the noise.

Several spectra were recorded and a fixed background from the dark-count rate of the detector and scattered laser light of 600 cps was subtracted from each file (dashed line in Fig. 4.7). Then, the peak was integrated to obtain the total number of detected ions.

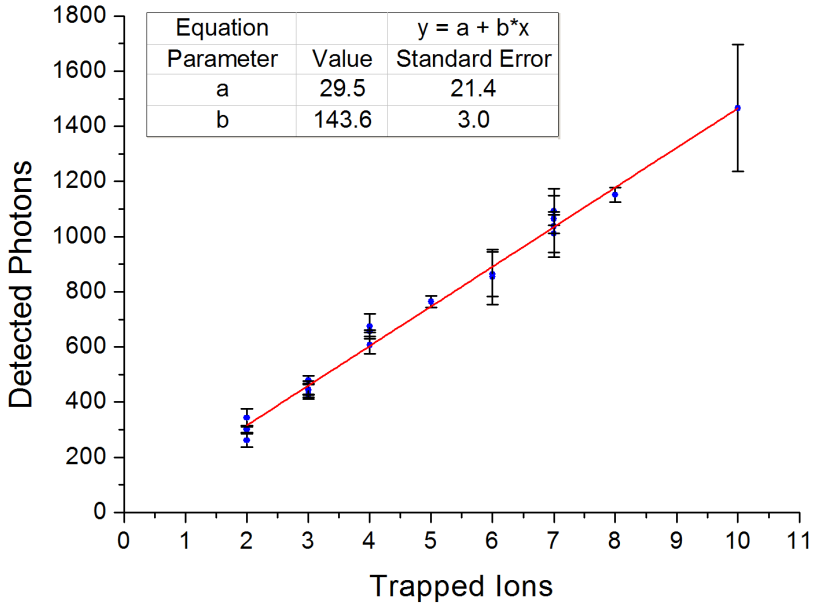

Figure 4.8: The quantized amount of detected photons for the fluorescence of various number of trapped ions.

Large errors lie in the estimation of the integral limits (vertical lines in Fig. 4.7) and, therefore, in the estimation of the integral. Since the width of each profile corresponding to the final temperature should be roughly the same, the deviation from the average width (0.5 s equivalent to ≈ 50 MHz) is an indication of the error size. The result is plotted in Fig. 4.8. A clearly stepwise increase is observed, which can be related to the quantized values for various number of trapped ions.

The relation between the amount of detected photons and the number of ions is highly linear, even though there are large errors in the estimation of the integral. Nevertheless, the calculated amount of detected photons for a single ion under these scanning conditions is extrapolated to be about 145 while the peak-fluorescence rate is evaluated to be roughly 300 cps. With these values, the number of ions from the fluorescence signal presented in Fig. 4.4 can be estimated. This signal was recorded under the same experimental conditions, right after the signals shown in Fig. 4.7, but with a longer stacking time. The integral of the fluorescence signal is about 375000 photons which corresponds to roughly 2600 ions, while the height is about 724000 cps which would correspond to roughly 2400 ions. Both values agree very well, which is an indication for the robustness of this estimation technique.

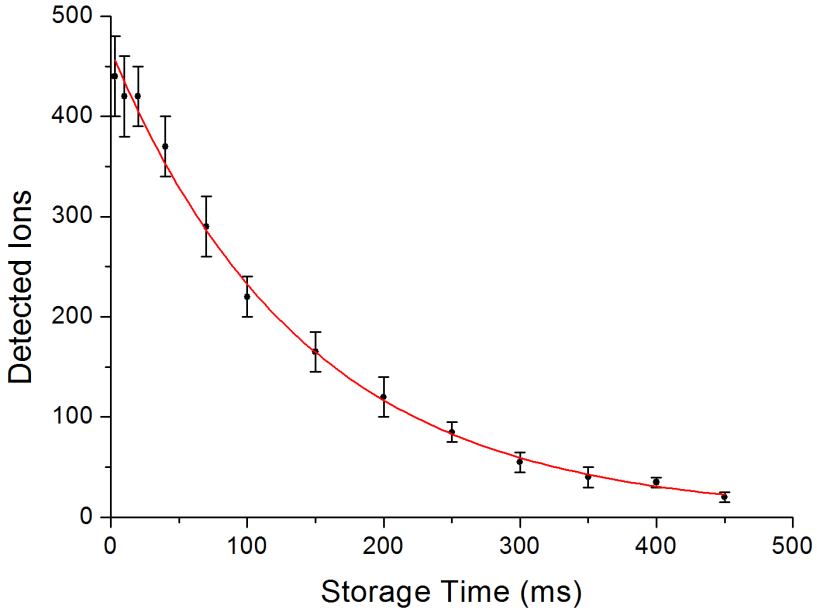

Figure 4.9: The detected number of ejected ions on the MCP from the trap for various storage times.

4.6 Trapping Lifetime

There are many variables which affect the storage time of a charged particle in a Penning trap. Among the main loss processes are the ion-ion or ion-neutral scattering and electron capture [106]. The loss processes are influenced by the vacuum quality, the dimensions of the trap, the ion temperature and energy/momentum spread, etc. Unfortunately, without dedicated measurements, the trapping lifetime - as the time after which the number of trapped ions decreases 2.71 times - can only be roughly evaluated.

A good way to measure the storage time would be to place a detector right after the trap which can detect the leaking neutral particles [106]. Considering that these particles are produced in charge-exchange collisions of the ions with the residual gas inside the trap, the amount of detected particles should be proportional to the number of trapped ions. Thus, by fitting the expected exponential decay of the detected neutral particles, the trapping lifetime can be extracted. Unfortunately, this is appropriate only for very large amounts of ions inside the trap.

Here, the trap was closed for various storage times and afterwards the remaining particles were ejected out of the trap by lowering one of the electrodes and detected with the MCP detector beneath the trap, after collimation with an einzel lens (Fig. 3.39).

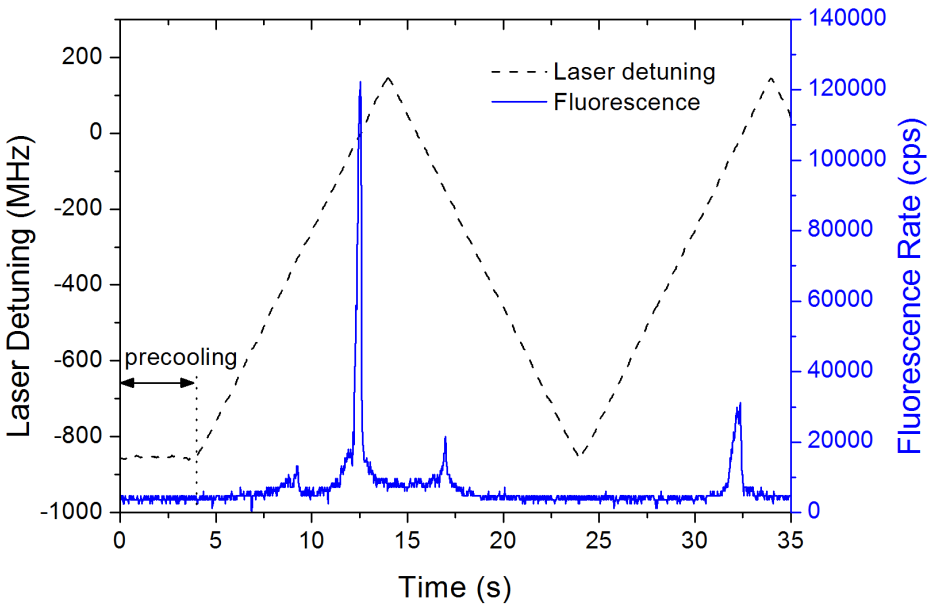

Figure 4.10: An example of fluorescence measurement with variable delay for the laser scanning as used for trapping lifetime evaluation.

An example of such a measurement for 200 eV ion energy is provided in Fig. 4.9. The trapping lifetime was calculated to be 143 ± 7 ms, which is much less than expected for the Penning trap and afterwards measured by means of fluorescence, as discussed below. The measured exponential decrease might be a side effect of the increasing longitudinal momentum spread of the ejected ions, after a few hundred axial oscillations inside the trap. Moreover, the magnetic field has a very large gradient outside the trapping region and it contributes to the defocussing of the ejected ions. These effects, combined with the long distance from the trap to the detector, leads to a reduced focusing on the MCP. It should be noted that in this experiment the ions were not laser-cooled since the MCP blocks the laser path.

The trapping lifetime with the cooling laser present but far-detuned was evaluated by measuring the decrease in the fluorescence rate. This was tried in two ways: In a first experiment, the trap was filled every time with the same conditions, such that a constant number of ions is stored in the trap. Now, the precooling duration is increased each time, which means that the laser passes over the central frequency of the selected transition with an increasing delay. For longer precooling durations, more particles are expected to be lost and the integral of the main fluorescence peak should be proportional to the number of remaining particles at the moment when the laser has no detuning.

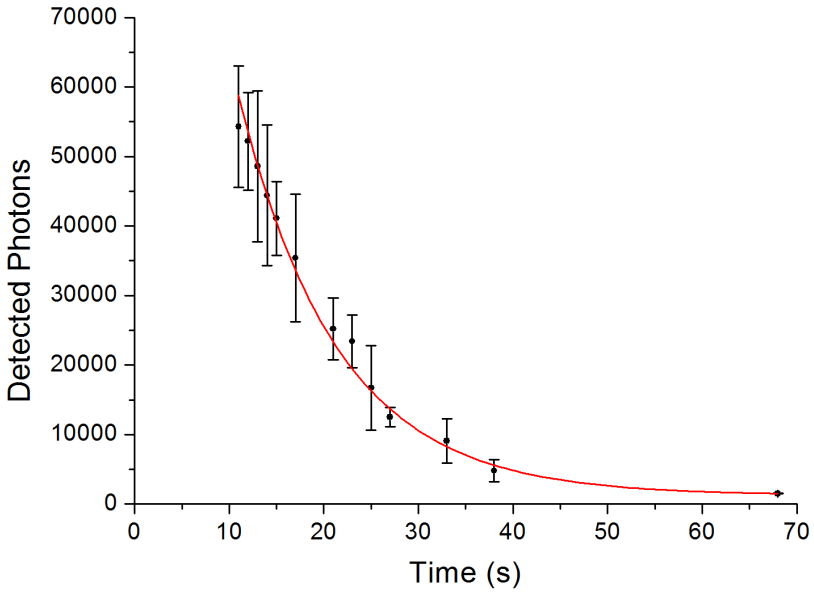

Figure 4.11: The detected number photons for various time-delays between the closing of the trap and the laser scanning over the central frequency of the selected cooling transition.

An example of this type of measurement with 4 seconds precooling time is provided in Fig. 4.10. The resulting data of the main peak integral for a stacking time of 10 seconds are plotted in Fig. 4.11. Although there are large uncertainties in fixing the limits of the integral or in the reproducibility of the trap reloading, the trapping lifetime can be evaluated from the exponential fit to 12.4 ± 0.8 seconds, which is two orders of magnitude larger than measured with the ejection technique. The value is also in good agreement with the decrease in the fluorescence rate for the second peak in Fig. 4.10, when the laser was scanned a second time from lower to higher frequencies: This fluorescence rate decreased approximatively 3.9 times in 19.8 seconds, resulting in a lifetime of ≈ 14.5 s.

The trapping lifetime can also be indirectly evaluated also from fluorescence measurement for a fixed laser frequency as presented in Fig. 4.2, assuming that the decrease in the fluorescence is caused by the loss of ions. Using an exponential fit on the decreasing slope, after the main peak, the trapping lifetime is evaluated to $40 - 50$ seconds, depending on the fitting limits. This is quite different from the previous results and is probably not only caused by the different trapping parameters. The longer trapping time indicates that the decrease in the fluorescence rate is not proportional to the number of trapped ions. This is also supported by the rather linear than exponential decrease in fluorescence. A shrinking number of ions might be partially compensated by a compactification of the

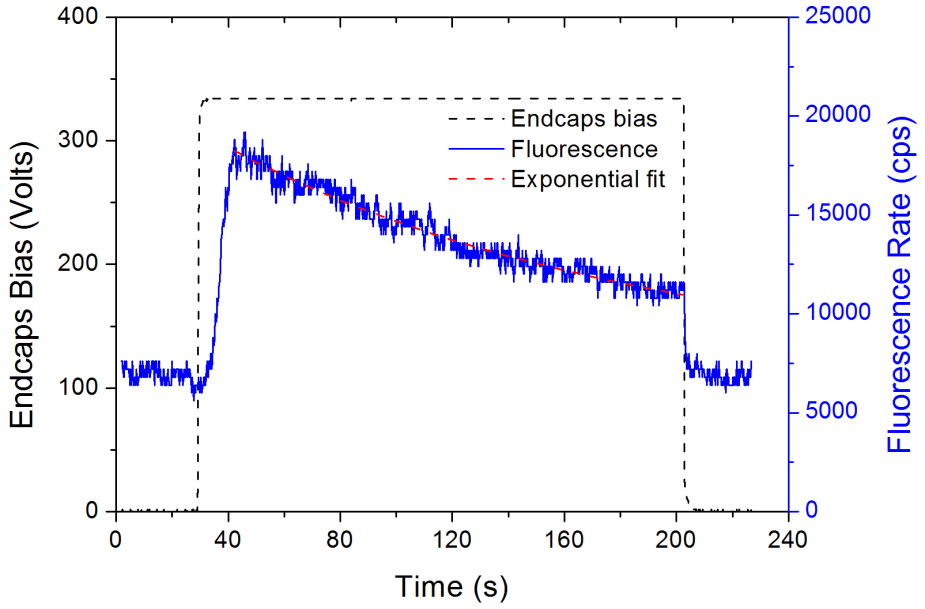

Figure 4.12: The time evolution of the fluorescence rate after closing the trap with a 300 MHz blue-shifted laser and the exponential fit of the decreasing slope.

cooled ion cloud.

An interesting result was observed with a fixed-frequency blue-shifted laser. Although, under normal circumstances, the stacking and the laser cooling should not work in this case, Fig. 4.12 indicates that it surprisingly does. For an explanation, one has to consider the effect of the high energy of the ions. By using Eq. (1.2), the Doppler width corresponding to 200 eV is 239 GHz, which is much larger than the difference between the different Zeeman sublevel transitions listed in Table 4.2. Moreover, there are three more transitions which accept the σ^- polarization totally or partially and, for two of them, the laser is red-shifted less than 100 GHz. As long as the energy of the ions compensate for the difference in the Zeeman-shifted transitions, the ion will not end up in a dark state and the laser cooling occurs even with a blue-shifted laser for the initially selected transition.

An example of fluorescence for a 300 MHz blue-shifted laser (relative to the leftmost transition from the Zeeman splitting scheme) is presented in Fig. 4.12. Using an exponential fit, the trapping lifetime is evaluated to 145 ± 6 seconds. Different trapping parameters and cooling approach can be blamed for the very different result. Though, since in a cryogenic trap there is no heating mechanism, it is possible that the previous decrease of the fluorescence in time for the red-shifted laser is mainly due to the cooling of the ions to the

temperature corresponding to the laser detuning. Hence, the fluorescence will drop after reaching a stable temperature regardless of the ion loss. By using a 300 MHz blue-shifted laser, the ions are initially cooled, but after reaching a certain temperature, the ions will be in a dynamic equilibrium between the heating and the cooling induced by the same laser. The decrease in the fluorescence could then be attributed mainly to the ion loss.

In summary, a conclusive statement about the lifetime of the ions cannot be drawn from the available data and this question should be subject of further investigations.

4.7 FFT-ICR and Laser Fluorescence-ICR

The final test in this experiment was to obtain the FFT-ICR signal as described in Section 2.2. Because of the low number of ions, observing the FFT-ICR signal is not trivial. In order to find the optimal parameters for the detection, the modified cyclotron motion ω_+ was first measured via the reduction in the fluorescence rate. This reduction is expected since the RF excitation of the cyclotron motion drives the ions to larger cyclotron radii and the spatial overlap with the laser beam is therefore reduced.

For this purpose, the RF excitation frequency was varied in variable steps of 50-400 Hz and the trap was reloaded each time. The stacking time was kept fixed at 20 seconds and the precooling time at 9 seconds. The endcaps were raised to 230 V and the ring was maintained at 0 V, to avoid an offset of the excitation signal. The laser was scanned over a range of 1 GHz in 10 seconds and the amplitude of the RF excitation signal was chosen such that, at resonance, the fluorescence signal is considerably reduced but still much higher than the background.

The result is presented in Fig. 4.13. The fluorescence rate is reduced to about 5000 cps when the modified cyclotron motion ω_+ is in resonance with the external RF excitation signal, compared with about 25000 cps outside the resonance or with about 40000 cps without any RF excitation signal. By fitting the data with a Gaussian shape, a resonance frequency of 2.5570 ± 0.0001 MHz is extracted. The number of the trapped ions is estimated to be ≈ 500.

The Gaussian function has a width of about 2900 Hz, which is rather large compared to the expected width of an FFT-ICR signal. For FFT-ICR, the excitation frequency should be very close to the reduced cyclotron frequency in order to have the resonant transfer of energy from the external RF excitation which will cause the ions to start moving coherently. Unlike FFT-ICR, coherent movement of the ions is not required for

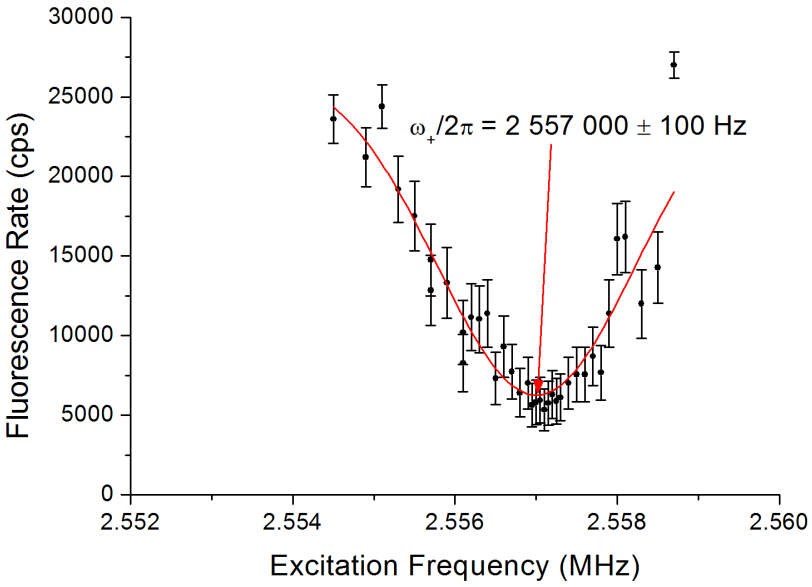

Figure 4.13: The reduction of the fluorescence rate corresponding to the resonance of the modified cyclotron motion with the external RF excitation signal.

measuring the reduced cyclotron frequency through laser fluorescence reduction. As previously mentioned, laser reduction appears because the ions are driven to larger cyclotron radii, which can be due to a non-resonant transfer of energy. Hence, a reduction in the laser fluorescence can be observed on a larger scale of the excitation frequency if the excitation amplitude is large enough.

Several modifications were made for obtaining the FFT-ICR: The laser frequency was maintained fixed, at about 700 MHz red-detuning; the stacking time was extended to 40 seconds with 3 Hz repetition rate; the correction electrodes were biased to -400 V during the trapping time in order to correct the shape of the electric field inside the trap [6, 21]. But the most important modification was the repeated, limited RF excitation time, immediately followed by a measurement after each excitation cycle. The ions were excited with 5000 periods of the external RF signal, corresponding to an excitation time of about 2 ms at 2.5570 MHz, followed by a 1 ms measurement with a spectrum analyzer. This cycle was repeated 5 times per second during the 30 seconds trapping time and averaged over 10 measurements by the spectrum analyzer.

A sampled signal of the FFT-ICR, recorded by the spectrum analyzer, is presented in Fig. 4.14. In order to obtain such a signal, a delicate balance between the laser cooling power and the RF excitation amplitude had to be obtained. When the amplitude of the

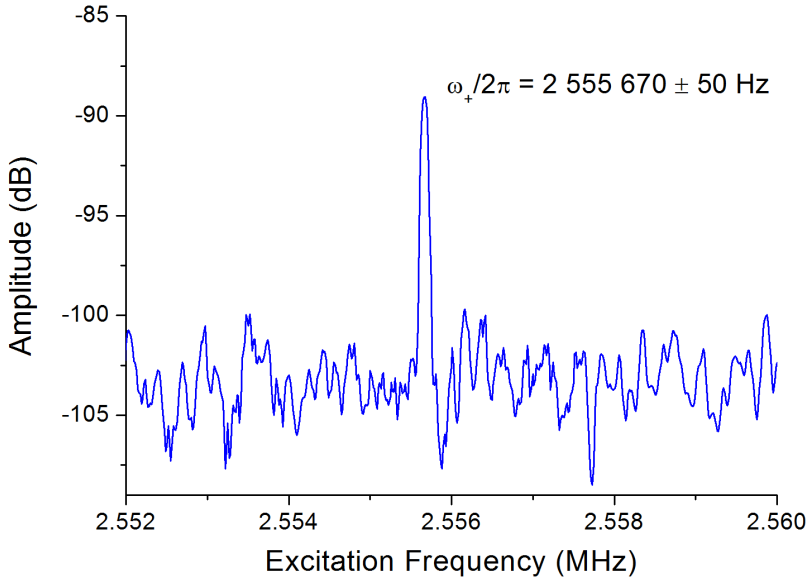

Figure 4.14: A sampled signal of the FFT-ICR, as recorded by the spectrum analyzer.

RF excitation is too high, the ions are driven outside the trap. When the laser cooling power is too high, the ions are strongly cooled and the FFT-ICR signal disappears.

Experimentally, this is obtained by adjusting the power of the cooling laser or the amplitude of the RF excitation and keep them constant afterwards. While keeping the amplitude RF excitation constant is easy, maintaining a constant power level of the laser proved to be difficult. Any small fluctuation in the laser power caused by the main fiber laser or by one of the resonators can tilt the balance one way or the other. An example of a good balance, corresponding to the FFT-ICR in Fig. 4.14, is illustrated in Fig. 4.15. Here the fluorescence rate is relatively constant after the initial precooling, meaning that the heating processes are in perfect balance with the cooling laser. One way to avoid this complication would be a smaller RF excitation amplitude while blocking the laser during the excitation and measurement time with a fast shutter, which unfortunately was not available during the experiment.

The resonance frequency of the FFT-ICR signal is found to be 2.55567 ± 0.00005 MHz. There is a systematic difference to the resonance frequency measured previously by fluorescence. The difference is around 1.3 kHz and it would correspond to a difference in the magnetic field of 2 mT, which might be caused by inhomogeneities in the magnetic field in the trapping region. Moreover, the laser may cross the trap not exactly on axis and therefore at some distance compared to the trap electrical midpoint. Hence, the

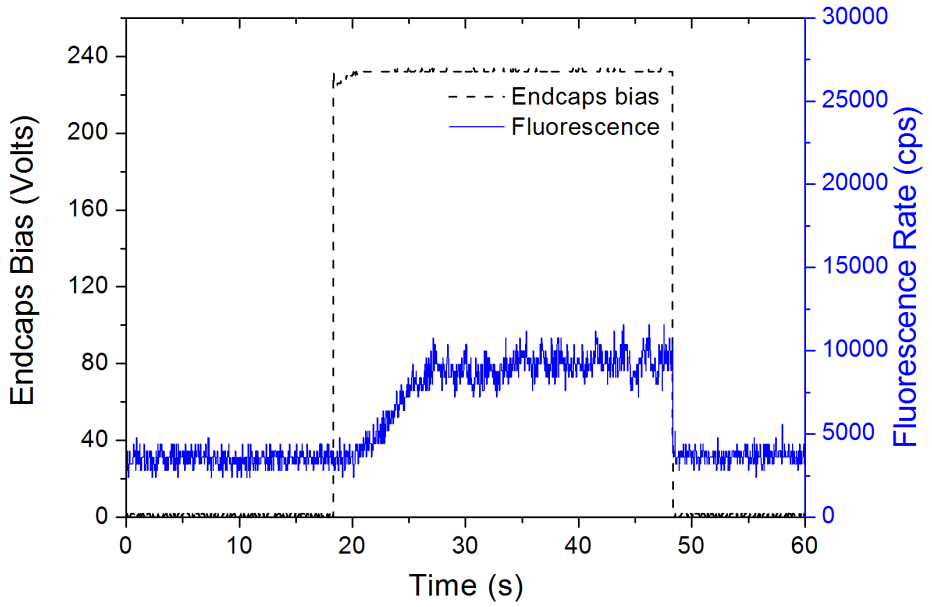

Figure 4.15: The constant fluorescence rate when the cooling laser is in balance with the heating RF excitation.

measurements are actually performed at slightly different points.

This measurement provides us with a possibility to extract the magnetic field at the trap midpoint and compare it with other data: Due to the correction electrodes, the trap can be approximated with an ideal trap and, thus, by using Eq. (2.27) and by calculating the axial frequency ω_z, the real cyclotron frequency can be evaluated. The axial frequency ω_z can be calculated with the modified form of Eq. (2.16) for the open-endcap Penning trap with correction electrodes [15, 107]

$$\omega_z^2 = C_2 \frac{qV_0}{md^2} \tag{4.7}$$

where C_2 is the expansion coefficient of the potential in the trap center and it has a calculated value of 0.61 for this trap while the parameter which characterizes the trap dimension is $d = 6.74$. However, there are some errors in the approximation of the trap with an ideal trap and in the estimation of the expansion coefficients, which limits the accuracy of determination in the absence of measurements for another ion mass [21]. Nevertheless, using these values for a trapping potential $V_0 = 230$ V, the magnetic field can then be calculated from Eq. (2.9) and it amounts to 4.090 ± 0.007 Tesla. This value is in excellent agreement with the values obtained from the magnet datasheet and from the Zeeman-adjusted optical transition frequency, as listed in Table 4.3.

Table 4.3: Comparison of the magnetic fields at the trap center obtained by different methods.

Method	**Relevant Parameter**	**Magnetic Field**
Magnet datasheet (58.7 A @ 6 T)	I=40.1 A	4.10 ± 0.01 T
Zeeman shift (13.996 GHz/T)	$\Delta\nu_{\mathrm{ZE}} = 57.4$ GHz	4.10 ± 0.01 T
Laser fluorescence ICR	$\omega_c/2\pi = 2.611$ MHz	4.092 ± 0.007 T
FFT-ICR	$\omega_c/2\pi = 2.610$ MHz	4.090 ± 0.007 T

5

Conclusions

5.1 Summary

Laser spectroscopy on trapped and cooled highly charged ions - as proposed by the SPECTRAP collaboration - is an ambitious goal and requires many years of sustained work on the experimental setup. In this thesis the first results were achieved in the form of the small, laser-cooled cloud of externally-injected Mg^+ ions, to be used for the sympathetic cooling of HCI.

As described in this work, an all-solid-state laser system at 279.6 nm was designed and successfully tested for this purpose. The laser is based on a Koheras continuous-wave fiber laser as a pump laser at 1118.5 nm and two consecutive frequency doublers. The first doubler uses noncritical phase-matching of an LBO nonlinear crystal, which has a phase-matching temperature at 1118 nm of around 90°C. The second doubler uses critical phase-matching of a BBO nonlinear crystal, using the round, Gaussian output of the first doubler. Since the doubling efficiency for second harmonic generation inside a nonlinear crystal is proportional to the input power, bow-tie optical resonators were constructed for the enhancement of the power inside the crystal. Both resonator were designed using the ray transfer matrix analysis and computer simulations in order to obtain the optimal experimental parameters according to the Boyd-Kleinmann theory. The length of the doublers is actively stabilized using the Hänsch-Couillaud polarization-analysis locking scheme. A maximum overall SHG efficiency at 33% was obtained, providing 320 mW of laser power at 559.3 nm for 950 mW of 1118.5 nm laser power. For the second doubler, a maximum of 16.7 mW of laser power at 279.6 nm for 210 mW of green power in front of the resonator was achieved, equivalent to an overall SHG efficiency of 8%.

5. CONCLUSIONS

In spite of some problems with the main fiber laser, which greatly affected the available pump power, the UV laser power that was achieved for the first trapping tests was still at a sufficient level. Due to very small frequency drifts, the main laser didn't require any frequency stabilization at all and was only frequency tuned in the free-running mode. Nevertheless, frequency stabilization was demonstrated as well using a High-Finesse wavemeter.

A Mg^+ ion source was developed for pulsed ion extraction and transfer into SPECTRAP. Therefore, laser ablation, surface ionization and electron impact ionization were tested. Finally, an atomic beam oven combined with electron impact ionization and pulsed extraction was installed. It delivers up to 50 Mg^+ ions per shot to the trap, with a very small time, momentum and energy spread.

The Penning trap used in SPECTRAP is a cylindrical trap with correction electrodes for optimization of the electrical field inside. Additional capture electrodes aided the in-flight capture of the externally injected ions by providing a longer flying path inside the trap. The laser beam of 1 mm in diameter and ≈ 0.8 mW in power, corresponding to about 1/3 of the saturation power for the selected transition, was sent along the trap axis.

By stacking up to 180 successive bunches of externally injected ions with a repetition frequency of 3 Hz, up to 2600 ions were simultaneously trapped and cooled from 200 eV kinetic energy down to about 0.1 K. These loading parameters are the result of an optimization of the fluorescence signal. The number of trapped ions was estimated by observing quantized jumps in the fluorescence signal corresponding to discrete ions. Because the cooling occurred mainly at the turning points of the ion axial motion, the typical cooling time was in the order of 10 seconds. The trapping lifetime was indirectly estimated via the decrease in the fluorescence signal to be roughly between 12 and 145 seconds, depending on the experimental conditions and the measurement method.

The FFT-ICR detection method was implemented using the split ring electrode of the trap. Using an external RF excitation at frequencies near the calculated reduced cyclotron frequency, ω_+ could be measured by detecting the decrease in the fluorescence signal. After a proper balancing between laser cooling power and the induced heating by the external RF excitation, FFT-ICR signals were obtained on a spectrum analyzer, which directly yields ω_+. The frequency obtained through these two methods were in reasonable agreement, considering the uncertainty of the overlap between the trap center and laser beam position. It also allowed a determination of the magnetic field down to 10 mT level.

Moreover, an excellent non-destructive ion detection method was demonstrated with this technique.

The results obtained in this thesis open the path for further investigations of sympathetic cooling of HCI and laser spectroscopy on forbidden transitions with high accuracy.

5.2 Future Experiments

Further improvements and experiments are planned for the future. First of all, the Mg ion source has to be optimized or replaced and the experimental conditions leading to losses from the trap improved in order to obtain a larger number of trapped ions. The most straightforward way to reduce the ion losses is to have a better vacuum.

The vacuum is expected to be improved for the next test by longer pumping and heating of the setup. The cooling speed of the Mg^+ ions can also be improved by using a more powerful laser beam at 279.6 nm, which would allow the stacking at a higher repetition frequency.

As for the Mg^+ ion source, assuming that the number of atoms coming from the oven is large enough, a higher ionization rate might be achieved with a larger electron current from the filament. The amount of emitted electrons is currently limited by space charge effects occuring at the small surface of the filament. Hence, by using either a second filament or a curled filament, a boost in the electron number and in the source yield can be expected. Combined with the reduced ion losses and with the more efficient stacking, it might be possible to reach the desired number of trapped Mg ions. Otherwise, the Mg ion source can be replaced with a Metal Vapor Vacuum Arc (MEVVA) source [108] or with a High Power Impulse Magnetron Sputtering (HIPIMS) source [109].

For testing the sympathetic cooling, an additional detectable ion species is necessary inside the trap. Since the FFT-ICR is not a very sensitive detection method, an ion with an optical transition from the ground state would be preferable. A possible candidate is Pb^+, with a transition at 710.2 nm [110] achievable by a Titanium:Sapphire laser. This forbidden transition would be an excellent test for the spectroscopy on HCI. Even though the lifetime of the upper level is 41 ms and the efficiency of the detection system is small, it might be still possible to observe fluorescence from cold Pb^+ by integrating the signal over a longer period of time and by having enough Pb^+ ions trapped. The Pb^+ ions can be also easily produced, similar to the Mg ions.

The first tests with multiple charged ions are planned to be performed with the C-like $^{40}Ca^{14+}$, which has a transition at 569.44 nm, or with the B-like $^{40}Ar^{13+}$, which has a transition at 441.24 nm. Both ions will become available with the installation of the connecting beamline to the existing EBIS. Finally, when the HITRAP facility will start delivering HCI, measurements of the hyperfine transition at 243.9 nm in H-like $^{209}Bi^{82+}$ will be performed, as a laser system for this purpose is already available in the SPECTRAP collaboration [111]. Other candidates are the hyperfine transition at 1019.7 nm in H-like $^{207}Pb^{81+}$ and - for disentanglement of the nuclear structure from QED effects - the hyperfine transition at 1555 nm in Li-like $^{209}Bi^{80+}$. By sympathetic cooling of these ions, it is expected to improve the accuracy to about 10^{-7} and therefore improve accuracy by more than three orders of magnitude compared to the currently available results from laser spectroscopy at the ESR or in an EBIT. This will provide a test of QED in the strong magnetic sector to a level on the order of 1% for the first time.

Appendix A

Troubleshooting

A.1 Problems with the Fiber Laser

Unfortunately, the reliability of the Koheras Boostik fiber laser didn't meet our expectations. The useful power without ASE was at maximum 1.1 W when delivered and dropped below 0.7 W after a few hundred hours of operation in parallel with an increase in ASE. This was much less than the specified 1.66 W. The laser was sent for repair to Menlo Systems because the manufacturer refused to accept it during warranty time.

After replacement of the booster amplifier, the power was up to 1.86 W useful power but it was immediately noticed that the laser was not linearly polarized and the power was running on two modes, separated by roughly 1.5 GHz and with polarization perpendicular to each other. The same behavior was then even detected with another oscillator from Koheras. The power of a chosen polarization direction was slowly oscillating between 40 and 60% of the total useful power. Hence, only about half of the power is available for the experiment.

The people from Menlo Systems investigated this problem and it seems that the seeding master oscillator has surprisingly no polarization selecting device. Thus, in order to be properly repaired, the seeding fiber laser has to be replaced or, at Menlo suggestion, a different seeding laser should be used. Since the built doublers are very efficient and for laser cooling the power requirements are very low, the fiber laser was used without being repaired. However, it is planned to replace the seeding laser with an external cavity diode laser in the future.

After a couple of months, the fiber laser broke for the third time because of some damage to a control fiber which prevented the first amplifier to be turned on. This time

it was a rather minor problem and the laser was repaired by Menlo Systems in a very short time.

It was also noticed that the laser is very unstable when it is operated at an output power over 1 W and was repeatedly shutting down because of back reflections of, most probably, one of the laser modes. Just to be in the safe area, the laser is currently used up to 1 W total power which means less than 500 mW in front of the first doubler.

A.2 Problems with the Doublers

The position of the cavity focusing mirrors has to be carefully adjusted since the distance between the focusing mirrors is chosen at the edge of stability for both resonators. An imprecision of only 1 mm in the distance can make the resonator unstable in one of the planes, as initially observed. Even a smaller deviation can cause a significant decrease in the doubling efficiency. Optimization of the distance between the focusing mirrors is complicated by the tilt of the mirrors and hence, the distance has to be measured between the points where the laser really hits the mirror. Therefore, at least one of the focusing mirrors from each resonator is placed on a micrometric linear translation stage. For the first resonator, due to the NCPM, adjusting this distance can be easily done by observing the output beam which should be perfectly round. Unfortunately, for the second resonator, adjusting this distance to the optimal value can be done only by observing the doubling efficiency.

Another problem was with the LBO crystal from the first resonator. At some point during the development of the first resonator, the doubling efficiency dropped by almost two orders of magnitude for the same input power level. Moreover, the shape of the output beam was strongly distorted, as if there were fissures in the AR coatings of the crystal or in the crystal itself. After carefully checking all parameters, the LBO crystal was thought to be the culprit. Since it is always advisable to have a back-up crystal, an additional LBO crystal was ordered. Surprisingly, the problem persisted with the second crystal. Soon it was noticed that after the laser system was recently moved to a newly built, air-conditioned laser lab, the frequency of the input laser was fixed at a different value, corresponding to a temperature of the fiber laser closer to the temperature in the laser lab. Apparently unconnected, it was this new frequency for which the absorption is unusual large in LBO, resulting in large cavity losses. This was also observed and briefly

documented in [66]. Fortunately, this frequency was not of interest and, after readjusting the fiber laser temperature, the problem disappeared.

The high power level of the fiber laser can still cause damage to the optical elements after long-term usage, even though the laser irradiance is well bellow the specified damage threshold. For example, the damage to the input Glan-Taylor prism of the Faraday isolator had a reduction of 1/3 in transmission after ≈ 4 years. Thus, the optical elements should be inspected for damage from time to time.

A.3 Problems with the Penning Trap

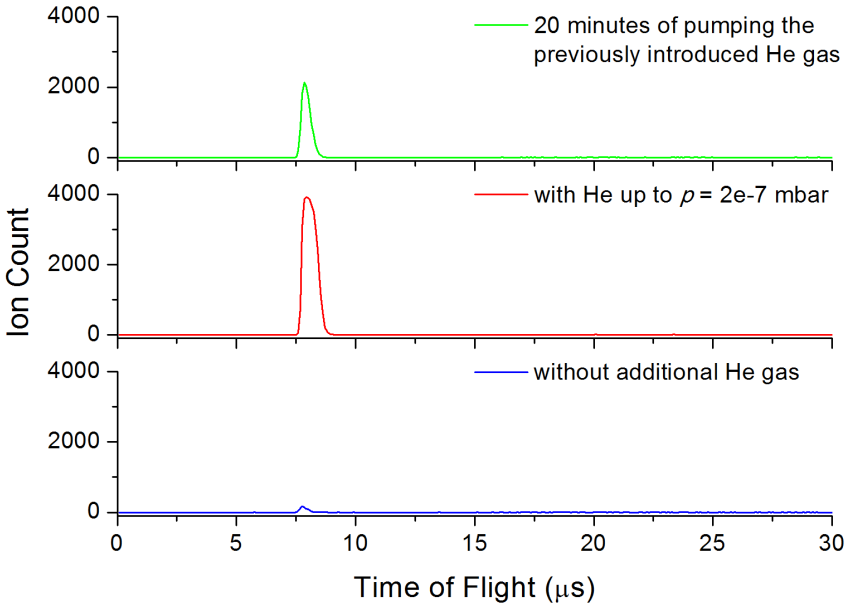

Figure A.1: Time of flight for the ions produced in the trap for three different values of the He partial pressure.

Because the SPECTRAP Penning trap is maintained at 4 K, the background gas can freeze on the electrodes and charge electrostatically if the vacuum is not good enough, as initially observed. This blocked the passage of the Mg^+ ion bunches through the trap and, thus, the trap could not be loaded.

Moreover, because of the energy of the transported ions, the trap was operated at several hundred volts which resulted in disturbing electron production, most probably through field emission. Furthermore, these electrons seemed to produce large amounts of parasitic ions from the background gas. Taking advantage of the MCP located under the

trap and by pulsing the upper capture electrode with a 1-μs pulse, TOF measurements were performed. The ions were identified to be He^+, which makes sense considering that it is the last background gas that would freeze on the walls in the 4 K environment. This was confirmed by purposefully introducing He gas in the beamline up to a total pressure of $2 \cdot 10^{-7}$ mbar, causing an ≈ 20 fold increase in the He^+ TOF peak (ignoring the possible saturation of the MCP), as shown in Fig. A.1. After the leaking was stopped and the beamline was pumped for 20 minutes, the TOF peak decreased to approximatively half of the previous value.

Consequently, the trap electrodes were repolished and slower ions were used. For avoiding the electrostatic charging, the vacuum before the initial cooling was improved and a device which partially prevented the uncollimated particles from entering the trapping area was installed. Finally, after all these modifications, the trap was successfully tested.

References

[1] D. Hanneke, S. Fogwell, and G. Gabrielse. **New Measurement of the Electron Magnetic Moment and the Fine Structure Constant**. *Phys. Rev. Lett.*, **100**:120801, 2008.

[2] S. Sturm, A. Wagner, B. Schabinger, J. Zatorski, Z. Harman, W. Quint, G. Werth, C. H. Keitel, and K. Blaum. **g Factor of Hydrogenlike $^{28}Si^{13+}$**. *Phys. Rev. Lett.*, **107**:023002, 2011.

[3] Thomas Beier. **The g_j factor of a bound electron and the hyperfine structure splitting in hydrogenlike ions**. *Physics Reports*, **339**(2-3):79 – 213, 2000.

[4] H.-J. Kluge, T. Beier, K. Blaum, L. Dahl, S. Eliseev, F. Herfurth, B. Hofmann, O. Kester, S. Koszudowski, C. Kozhuharov, G. Maero, W. Nörtershäuser, J. Pfister, W. Quint, U. Ratzinger, A. Schempp, R. Schuch, Th. Stöhlker, R.C. Thompson, M. Vogel, G. Vorobjev, D.F.A. Winters, and G. Werth. **Chapter 7 HITRAP: A Facility at GSI for Highly Charged Ions**. In S. Salomonson and E. Lindroth, editors, *Current Trends in Atomic Physics*, **53** of *Advances in Quantum Chemistry*, pages 83 – 98. Academic Press, 2008.

[5] M. Vogel, J. Alonso, S. Djekic, H.-J. Kluge, W. Quint, S. Stahl, J. Verdu, and G. Werth. **Towards electronic g-factor measurements in medium-heavy hydrogen-like and lithium-like ions**. *Nuclear Instruments and Methods in Physics Research Section B: Beam Interactions with Materials and Atoms*, **235**(1-4):7 – 16, 2005.

[6] Klaus Blaum. **High-accuracy mass spectrometry with stored ions**. *Physics Reports*, **425**(1):1 – 78, 2006.

[7] Manuel Vogel and Wolfgang Quint. **Trap-assisted precision spectroscopy of forbidden transitions in highly-charged ions**. *Physics Reports*, **490**(1-2):1 – 47, 2010.

[8] A. V. Volotka, D. A. Glazov, I. I. Tupitsyn, N. S. Oreshkina, G. Plunien, and V. M. Shabaev. **Ground-state hyperfine structure of H-, Li-, and B-like ions in the intermediate-Z region**. *Phys. Rev. A*, **78**:062507, 2008.

[9] Jenny E. Rosenthal and G. Breit. **The Isotope Shift in Hyperfine Structure**. *Phys. Rev.*, **41**:459–470, 1932.

[10] M. F. Crawford and A. L. Schawlow. **Electron-Nuclear Potential Fields from Hyperfine Structure**. *Phys. Rev.*, **76**:1310–1317, 1949.

[11] I. Klaft, S. Borneis, T. Engel, B. Fricke, R. Grieser, G. Huber, T. Kühl, D. Marx, R. Neumann, S. Schröder, P. Seelig, and L. Völker. **Precision Laser Spectroscopy of the Ground State Hyperfine Splitting of Hydrogenlike $^{209}Bi^{82+}$**. *Phys. Rev. Lett.*, **73**:2425–2427, 1994.

[12] M. Vogel, D. F. A. Winters, D. M. Segal, and R. C. Thompson. **Proposed precision laser spectrometer for trapped, highly charged ions**. *Review of Scientific Instruments*, **76**(10):103102, 2005.

[13] V. M. Shabaev, A. N. Artemyev, V. A. Yerokhin, O. M. Zherebtsov, and G. Soff. **Towards a Test of QED in Investigations of the Hyperfine Splitting in Heavy Ions**. *Phys. Rev. Lett.*, **86**:3959–3962, 2001.

[14] Wilfried Nörtershäuser. **Laser spectroscopy for QED tests in highly charged ions**. *Hyperfine Interactions*, **199**:131–140, 2011.

[15] Zoran Andjelkovic, Shailen Bharadia, Bettina Sommer, Manuel Vogel, and Wilfried Nörtershäuser. **Towards high precision in-trap laser spectroscopy of highly charged ions**. *Hyperfine Interactions*, **196**:81–91, 2010.

[16] Wolfgang Demtröder. *Laser spectroscopy*. Springer, 2003.

[17] K. Blaum and F. Herfurt. **Trapped charged particles and fundamental interactions**. *Lecture Notes in Physics*, **749**, 2008.

[18] Evgeni D. Donets. **Historical review of electron beam ion sources**. *Review of Scientific Instruments*, **69**(2):614–619, 1998.

[19] D. Schneider, D. DeWitt, M. W. Clark, R. Schuch, C. L. Cocke, R. Schmieder, K. J. Reed, M. H. Chen, R. E. Marrs, M. Levine, and R. Fortner. **Ion-collision experiments with slow, very highly charged ions extracted from an electron-beam ion trap**. *Phys. Rev. A*, **42**:3889–3895, 1990.

[20] R. E. Marrs. **Production of U^{92+} with an electron beam ion trap (invited)**. *Rev. Sci. Instrum.*, **67**(3):941–944, 1996.

[21] Zoran Andjelković. *Dissertation in preparation*. PhD thesis, University of Mainz, Mainz, 2012.

[22] Viorica N. Gheorghe Fouad G. Major and Günther Werth. *Charged Particle Traps: Physics and Techniques of Charged Particle Field Confinement*. Springer, 2004.

[23] S. Earnshaw. **On the nature of the molecular forces which regulate the constitution of the luminiferous ether**. *Trans. Camb. Phil. Soc*, **7**:97–112, 1842.

[24] H.G. Dehmelt. **Radiofrequency Spectroscopy of Stored Ions I: Storage**. **3** of *Advances in Atomic and Molecular Physics*, pages 53 – 72. Academic Press, 1968.

[25] Wolfgang Paul. **Electromagnetic traps for charged and neutral particles**. *Rev. Mod. Phys.*, **62**:531–540, 1990.

[26] D.A. Church and H.G. Dehmelt. **Radiative Cooling of an Electrodynamically Contained Proton Gas**. *J. Appl. Phys.*, **40**:3421–3425, 1969.

[27] D. J. Wineland and H. G. Dehmelt. **Principles of the stored ion calorimeter**. *Journal of Applied Physics*, **46**(2):919–930, 1975.

REFERENCES

[28] G Bollen, S Becker, H.-J Kluge, M König, R.B Moore, T Otto, H Raimbault-Hartmann, G Savard, L Schweikhard, and H Stolzenberg. **ISOLTRAP: a tandem Penning trap system for accurate on-line mass determination of short-lived isotopes**. *Nuclear Instruments and Methods in Physics Research Section A: Accelerators, Spectrometers, Detectors and Associated Equipment*, **368**(3):675 – 697, 1996.

[29] Melvin B. Comisarow and Alan G. Marshall. **Fourier transform ion cyclotron resonance spectroscopy**. *Chemical Physics Letters*, **25**(2):282 – 283, 1974.

[30] J. Ketelaer, J. Krämer, D. Beck, K. Blaum, M. Block, K. Eberhardt, G. Eitel, R. Ferrer, C. Geppert, S. George, F. Herfurth, J. Ketter, Sz. Nagy, D. Neidherr, R. Neugart, W. Nörtershäuser, J. Repp, C. Smorra, N. Trautmann, and C. Weber. **TRIGA-SPEC: A setup for mass spectrometry and laser spectroscopy at the research reactor TRIGA Mainz**. *Nuclear Instruments and Methods in Physics Research Section A: Accelerators, Spectrometers, Detectors and Associated Equipment*, **594**(2):162 – 177, 2008.

[31] Lowell S. Brown and Gerald Gabrielse. **Precision spectroscopy of a charged particle in an imperfect Penning trap**. *Phys. Rev. A*, **25**:2423–2425, 1982.

[32] H. Häffner, T. Beier, S. Djekić, N. Hermanspahn, H.-J. Kluge, W. Quint, S. Stahl, J. Verdú, T. Valenzuela, and G. Werth. **Double Penning trap technique for precise g factor determinations in highly charged ions**. *The European Physical Journal D - Atomic, Molecular, Optical and Plasma Physics*, **22**:163–182, 2003.

[33] Wayne M Itano, J C Bergquist, J J Bollinger, and D J Wineland. **Cooling methods in ion traps**. *Physica Scripta*, **1995**(T59):106, 1995.

[34] T.W. Hänsch and A.L. Schawlow. **Cooling of gases by laser radiation**. *Optics Communications*, **13**(1):68 – 69, 1975.

[35] W D Phillips, P D Lett, S L Rolston, C E Tanner, R N Watts, C I Westbrook, C Salomon, J Dalibard, A Clairon, and S Guellati. **Optical Molasses: The Coldest Atoms Ever**. *Physica Scripta*, **1991**(T34):20, 1991.

[36] Christopher J. Foot. *Atomic Physics*. OUP Oxford, 2004.

[37] Claude Cohen-Tannoudji, Jacques Dupont-Roc, and Gilbert Grynberg. *Optical Bloch Equations*, pages 353–405. Wiley-VCH Verlag GmbH, 2008.

[38] Harold J. Metcalf and Peter van der Straten. *Laser Cooling and Trapping*. Springer, 1999.

[39] Kristian Molhave. *Construction of and Experiments with a Linear Paul Trap*. Master, University of Aarhus, Denmark, 2000.

[40] Pradip K. Ghosh. *Ion Traps*. Oxford University Press, USA, 1996.

[41] M. Bussmann, U. Schramm, D. Habs, V.S. Kolhinen, and J. Szerypo. **Stopping highly charged ions in a laser-cooled one component plasma of ions**. *International Journal of Mass Spectrometry*, **251**(2-3):179 – 189, 2006.

[42] Michael Bussmann. *Laser-Cooled Ion Beams and Strongly Coupled Plasmas for Precision Experiments*. Dissertation, Ludwig-Maximilians University Munich, Munich, 2007.

[43] M. Bussmann, U. Schramm, and D. Habs. **Simulating the stopping dynamics of highly charged ions in an ultra-cold, strongly coupled plasma**. *Hyperfine Interactions*, **173**:27–34, 2006.

[44] U. Schramm and D. Habs. **Crystalline ion beams**. *Progress in Particle and Nuclear Physics*, **53**(2):583 – 677, 2004.

[45] Setsuo Ichimaru. **Strongly coupled plasmas: high-density classical plasmas and degenerate electron liquids**. *Rev. Mod. Phys.*, **54**:1017–1059, 1982.

[46] Daniel H. E. Dubin. **Theory of structural phase transitions in a trapped Coulomb crystal**. *Phys. Rev. Lett.*, **71**:2753–2756, 1993.

[47] Günter Zwicknagel, Christian Toepffer, and Paul-Gerhard Reinhard. **Stopping of heavy ions in plasmas at strong coupling**. *Physics Reports*, **309**(3):117 – 208, 1999.

[48] Radu Cazan, Christopher Geppert, Wilfried Nörtershäuser, and Rodolfo Sánchez. **Towards sympathetic cooling of trapped ions with laser-cooled Mg^+ ions for mass spectrometry and laser spectroscopy**. *Hyperfine Interactions*, **196**:177–189, 2010.

[49] Yu Ralchenko, A. E. Kramida, J. Reader, and Nist A. S. D. Team. **NIST Atomic Spectra Database (version 3.1.5)**, 2008.

[50] John Canning. **Fibre lasers and related technologies**. *Optics and Lasers in Engineering*, **44**(7):647 – 676, 2006.

[51] Emmanuel Mimoun, Luigi De Sarlo, Jean-Jacques Zondy, Jean Dalibard, and Fabrice Gerbier. **Sum-frequency generation of 589 nm light with near-unit efficiency**. *Opt. Express*, **16**(23):18684–18691, 2008.

[52] NKT Photonics A/S. **Koheras Narrow linewidth Low Noise Fiber Lasers**, November 2011.

[53] P. A. Franken, A. E. Hill, C. W. Peters, and G. Weinreich. **Generation of Optical Harmonics**. *Phys. Rev. Lett.*, **7**:118–119, 1961.

[54] Robert W. Boyd. *Nonlinear Optics*. Academic Press, 2003.

[55] Bahaa E. A. Saleh and Malvin Carl Teich. *Fundamentals of Photonics*. Wiley-Interscience, 2007.

[56] M. Bass, P. A. Franken, J. F. Ward, and G. Weinreich. **Optical Rectification**. *Phys. Rev. Lett.*, **9**:446–448, 1962.

[57] Martynas Beresna, Peter G. Kazansky, Yuri Svirko, Martynas Barkauskas, and Romas Danielius. **High average power second harmonic generation in air**. *Applied Physics Letters*, **95**(12):121502, 2009.

[58] Rüdiger Paschotta. *Encyclopedia of Laser Physics and Technology*. Wiley-VCH, Berlin, 2008.

[59] Shujie Lin, Baichang Wu, Fali Xie, and Chuangtian Chen. **Phase matching retracing behavior for second harmonic generation in LiB_3O_5 crystal**. *Journal of Applied Physics*, **73**(3):1029–1034, 1993.

[60] Castech. **Fujian Castech Crystals, Inc.**, January 2012.

[61] G. D. Boyd and D. A. Kleinman. **Parametric Interaction of Focused Gaussian Light Beams**. **39**(8):3597–3639, 1968.

[62] Y.F. Chen and Y.C. Chen. **Analytical functions for the optimization of second-harmonic generation and parametric generation by focused Gaussian beams**. *Applied Physics B: Lasers and Optics*, **76**:645–647, 2003.

[63] R. W. P. Drever, J. L. Hall, F. V. Kowalski, J. Hough, G. M. Ford, A. J. Munley, and H. Ward. **Laser phase and frequency stabilization using an optical resonator**. *Applied Physics B: Lasers and Optics*, **31**:97–105, 1983.

[64] Eric D. Black. **An introduction to Pound-Drever-Hall laser frequency stabilization**. **69**(1):79–87, 2001.

[65] T.W. Hansch and B. Couillaud. **Laser frequency stabilization by polarization spectroscopy of a reflecting reference cavity**. *Optics Communications*, **35**(3):441 – 444, 1980.

[66] A. Friedenauer, F. Markert, H. Schmitz, L. Petersen, S. Kahra, M. Herrmann, Th. Udem, T.W. Hänsch, and T. Schätz. **High power all solid state laser system near 280 nm**. *Applied Physics B: Lasers and Optics*, **84**:371–373, 2006.

[67] R. Clark Jones. **New Calculus for the Treatment of Optical Systems. VIII. Electromagnetic Theory**. *J. Opt. Soc. Am.*, **46**(2):126–131, 1956.

[68] H. Kogelnik and C. V. Shank. **Coupled-Wave Theory of Distributed Feedback Lasers**. *Journal of Applied Physics*, **43**(5):2327–2335, 1972.

[69] K. O. Hill, Y. Fujii, D. C. Johnson, and B. S. Kawasaki. **Photosensitivity in optical fiber waveguides: Application to reflection filter fabrication**. *Applied Physics Letters*, **32**(10):647–649, 1978.

[70] KH Yla-Jarkko and AB Grudinin. **Performance limitations of high-power DFB fiber lasers**. *IEEE Photonics Technology Letters*, **15**(2):191–193, 2003.

[71] R. Paschotta, J. Nilsson, A. C. Tropper, and D. C. Hanna. **Ytterbium-doped fiber amplifiers**. *IEEE Journal of Quantum Electronics*, **33**:1049–1056, 1997.

[72] Ruth Steinborn. *Ein leistungsstarker Ytterbium-Faserverstärker bei 1091 nm für eine kontinuierliche Lyman-α-Quelle*. Diplom, University of Mainz, Mainz, 2009.

[73] H.M. Pask, R.J. Carman, D.C. Hanna, A.C. Tropper, C.J. Mackechnie, P.R. Barber, and J.M. Dawes. **Ytterbium-doped silica fiber lasers: versatile sources for the 1-1.2 m region**. *Selected Topics in Quantum Electronics, IEEE Journal of*, **1**:2–13, 1995.

[74] Michel J.F. Digonnet. *Rare-Earth-Doped Fiber Lasers and Amplifiers*. CRC Press, 2001.

[75] Peter Herskind, Jens Lindballe, Christoph Clausen, Jens Lykke Sørensen, and Michael Drewsen. **Second-harmonic generation of light at 544 and 272 nm from an ytterbium-doped distributed-feedback fiber laser**. *Opt. Lett.*, **32**(3):268–270, 2007.

[76] M. Brieger, H. Büsener, A. Hese, F. v.Moers, and A. Renn. **Enhancement of single frequency SGH in a passive ring resonator**. *Optics Communications*, **38**(5-6):423 – 426, 1981.

[77] J. S. Nielsen. **Generation of 90-mW continuous-wave tunable laser light at 280 nm by frequency doubling in a KDP crystal**. *Opt. Lett.*, **20**(8):840–842, 1995.

[78] Tim Freegarde and Claus Zimmermann. **On the design of enhancement cavities for second harmonic generation**. *Optics Communications*, **199**(5-6):435 – 446, 2001.

[79] Joseph T. Verdeyen. *Laser Electronics*. Prentice Hall, 1995.

[80] Michael D. Harvey and Andrew G. White. **Frequency locking by analysis of orthogonal modes**. *Optics Communications*, **221**(13):163 – 171, 2003.

[81] K. Kondo, M. Oka, H. Wada, T. Fukui, N. Umezu, K. Tatsuki, and S. Kubota. **Demonstration of long-term reliability of a 266-nm, continuous-wave, frequency-quadrupled solid-state laser using β-BaB_2O_4**. *Opt. Lett.*, **23**(3):195–197, 1998.

[82] J. D. Bhawalkar, Y. Mao, H. Po, A. K. Goyal, P. Gavrilovic, Y. Conturie, and S. Singh. **High-power 390-nm laser source based on efficient frequency doubling of a tapered diode laser in an external resonant cavity**. *Opt. Lett.*, **24**(12):823–825, 1999.

[83] D.N. Madsen, P. Yu, S. Balslev, and J.W. Thomsen. **Generation of 99-mW continuous-wave 285-nm radiation for magneto-optical trapping of Mg atoms**. *Applied Physics B: Lasers and Optics*, **75**:835–839, 2002.

[84] M. Herrmann, V. Batteiger, S. Knünz, G. Saathoff, Th. Udem, and T. W. Hänsch. **Frequency Metrology on Single Trapped Ions in the Weak Binding Limit: The $3s_{1/2} - 3p_{3/2}$ Transition in $^{24}Mg^+$**. *Phys. Rev. Lett.*, **102**:013006, 2009.

[85] Andreas Krieger. *Dissertation in preparation*. PhD thesis, University of Mainz, Mainz, 2012.

[86] S Amoruso, R Bruzzese, N Spinelli, and R Velotta. **Characterization of laser-ablation plasmas**. *Journal of Physics B: Atomic, Molecular and Optical Physics*, **32**(14):R131, 1999.

[87] Yoshinori Hashimoto, Leo Matsuoka, Hiroyuki Osaki, Yu Fukushima, and Shuichi Hasegawa. **Trapping Laser Ablated Ca^+ Ions in Linear Paul Trap**. *Japanese Journal of Applied Physics*, **45**(9A):7108–7113, 2006.

[88] Y. Hashimoto, K. Minamino, D. Nagamoto, and S. Hasegawa. **Measurement of isotope ratio of Ca^+ ions in a linear Paul Trap**. *AIP Conference Proceedings*, **1104**(1):36–41, 2009.

[89] O.W. Richardson. *The Emission of Electricity from Hot Bodies*. Longman's, Green and Company, London, 1916.

[90] Nobelprize.org. **Owen Willans Richardson - Nobel Lecture**, 1929.

[91] R. G.a Wilson. **Surface Ionization Ion Sources**. *Nuclear Science, IEEE Transactions on*, **14**:72 – 74, 1967.

[92] Mark G. Inghram and William A. Chupka. **Surface Ionization Source Using Multiple Filaments**. *Review of Scientific Instruments*, **24**(7):518–520, 1953.

REFERENCES

[93] M. J. Dresser. **The Saha-Langmuir Equation and its Application**. *Journal of Applied Physics*, **39**(1):338–339, 1968.

[94] Toshihiro Fujii and Hiromi Arimoto. **New sensitive and selective detector for gas chromatography: surface ionization detector with a hot platinum emitter**. *Analytical Chemistry*, **57**(13):2625–2628, 1985.

[95] J. P. Blewett and Ernest J. Jones. **Filament Sources of Positive Ions**. *Phys. Rev.*, **50**:464–468, 1936.

[96] Kenneth Barbalace. **Periodic Table of Elements - EnvironmentalChemistry.com, 1995 - 2012**, December 2011.

[97] HeatWave Labs. **Alkali earths and Alkali metal ion sources**, December 2011.

[98] Gregory H. Wannier. **The Threshold Law for Single Ionization of Atoms or Ions by Electrons**. *Phys. Rev.*, **90**:817–825, 1953.

[99] L. Jiao, Y. Zhou, and P. Hou. **Cross section for single ionization of magnesium by electron impact**. *Physics Letters A*, **372**(32):5318 – 5320, 2008.

[100] J. R. White and A. E. Cameron. **The Natural Abundance of Isotopes of Stable Elements**. *Phys. Rev.*, **74**:991–1000, 1948.

[101] Raphael Jöhren. *Dissertation in preparation*. PhD thesis, University of Münster, Münster, 2012.

[102] D.J. Bate, K. Dholakia, R.C. Thompson, and D.C. Wilson. **Ion Oscillation Frequencies in a Combined Trap**. *Journal of Modern Optics*, **39**(2):305–316, 1992.

[103] V. Batteiger, S. Knünz, M. Herrmann, G. Saathoff, H. A. Schüssler, B. Bernhardt, T. Wilken, R. Holzwarth, T. W. Hänsch, and Th. Udem. **Precision spectroscopy of the $3s$-$3p$ fine-structure doublet in Mg^+**. *Phys. Rev. A*, **80**:022503, 2009.

[104] P. Zeeman. **The Effect of Magnetisation on the Nature of Light Emitted by a Substance**. *Nature*, **55**:347, 1897.

[105] Richard Thompson. *private communication*. Imperial College London, 2011.

[106] H. B. Pedersen, D. Strasser, O. Heber, M. L. Rappaport, and D. Zajfman. **Stability and loss in an ion-trap resonator**. *Phys. Rev. A*, **65**:042703, 2002.

[107] G. Gabrielse, L. Haarsma, and S.L. Rolston. **Open-endcap Penning traps for high precision experiments**. *International Journal of Mass Spectrometry and Ion Processes*, **88**(23):319 – 332, 1989.

[108] Ian G. Brown. **Vacuum arc ion sources**. *Review of Scientific Instruments*, **65**(10):3061–3081, 1994.

[109] Joakim Andersson and André Anders. **Self-Sputtering Far above the Runaway Threshold: An Extraordinary Metal-Ion Generator**. *Phys. Rev. Lett.*, **102**:045003, 2009.

[110] X. Feng, G. Z. Li, and G. Werth. **High-precision hyperfine spectroscopy in $M1$ - $M1$ double-resonance transitions on trapped $^{207}Pb^+$**. *Phys. Rev. A*, **46**:2959–2961, 1992.

[111] S. Albrecht, S. Altenburg, C. Siegel, N. Herschbach, and G. Birkl. **A laser system for the spectroscopy of highly charged bismuth ions**. *Applied Physics B: Lasers and Optics*, **Online First**:1–6, 2011.